UNIVERSITY OF CALIFORNIA
RIVERSIDE

Multi-Scale Mathematical Modeling Study of Proper Shape Formation During Epithelial Tissue Development

A Dissertation submitted in partial satisfaction
of the requirements for the degree of

Doctor of Philosophy

in

Mathematics

by

Jennifer Rangel Ambriz

September 2024

Dissertation Committee:

Dr. Mark Alber, Chairperson
Dr. Weitao Chen
Dr. Jia Gou

The Dissertation of Jennifer Rangel Ambriz is approved:

Committee Chairperson

University of California, Riverside

Acknowledgements

First, I want to express my deepest gratitude and appreciation for my advisor, Dr. Mark Alber. I want to thank Dr. Alber for directing my research, spending countless hours helping me develop my scientific thinking and writing skills, supporting me through GSRs, and believing in my potential to succeed in the program. This journey would have been impossible without Dr. Alber's support, guidance, mentorship, patience, and life advice. No words can express my endless appreciation for all of the time and resources Dr. Alber has invested in helping me grow as a researcher and academic.

Next, I would like to thank my committee members, Dr. Weitao Chen and Dr. Jia Gou for their support, time, and insightful comments on my work. I want to give a special thank you to Dr. Chen for playing a crucial role in my success and supporting me throughout these challenging years. I am beyond grateful for her guidance and mentorship on my research projects. Thank you Dr. Chen for the constant encouragement and support, for believing in me and investing a lot of time in helping me succeed.

I would also like to thank and acknowledge my experimental collaborators, Dr. Jeremiah J. Zartman, Dr. Nilay Kumar, Mayesha S. Mim, and Dr. Marycruz Flores-Flores from the University of Notre Dame. Thank you for your hard work, dedication, and passion for biology. This project would not have been possible without you. Also, thank you for your hospitality during my summer visit at Note Drame and for giving me the opportunity to see *Drosophilas* in real life.

Thank you to the many wonderful mentors I've been so lucky to have: Sam, Jolene, Mikhal, Francesco, Christian, and Kevin. Thank you all for everything you've ever taught me, for always answering a million questions, and for the many opportunities you have provided me with. Your continuous support, words of encouragement, and guidance will never be forgotten. I would have never made it this far without you and for that, I will be eternally grateful!

Thank you to my dear friends, research companions, and cohort for making my days so much brighter. Alysha, I could not have asked for a better friend to embark on this

journey with. Thank you for being my anchor. I simply cannot imagine reaching this milestone without you. Christian, thank you for always having the best words of advice and encouragement. You have been one of my greatest mentors and also one of my dearest friends. Nav, Austin, and James, your friendship and endless support mean the world to me. There are not enough words to describe how thankful I am for each and every one of you.

I would like to give a very special thank you to Margarita Roman for being there for me every step of the way. Thank you for everything you have ever done for me. You are truly the rock and lifeline of our department and all graduate students. Your charisma, dedication, and genuine investment in our success and well-being will forever be appreciated.

To my family, thank you for your love, support, compassion, and patience throughout this journey. Your endless words of encouragement have kept me focused, motivated, and resilient. I would have never made it without you.

Finally, I want to thank the National Science Foundation for supporting this research through grant DMS-2029814.

The text of this dissertation, in part or in full, is a reprint of the material as it appears in: [1] Nilay Kumar, Jennifer Rangel Ambriz, Kevin Tsai, Mayesha Sahir Mim, Marycruz Flores-Flores, Weitao Chen, Jeremiah J. Zartman, and Mark Alber. Balancing competing effects of tissue growth and cytoskeletal regulation during *Drosophila* wing disc development. *Nat Commun* **15**, 2477 (2024). The authors of correspondence of [1], Mark Alber and Jeremiah J. Zartman, directed and supervised the research of [1] which forms the basis for a chapter of this dissertation, in addition to contributing to the research and preparation of the manuscript. Kevin Tsai developed and calibrated the initial computational model and code. Weitao Chen helped conceptualize the investigation, provided technical advice for setting up simulations, and contributed to the data and simulation analysis. Nilay Kumar, Mayesha Sahir Mim, Marycruz Flores-Flores, and Jeremiah J. Zartman designed and performed the experiments on the *Drosophila* wing disc as well as provided biological expertise. In addition, Nilay Kumar analyzed the experimental data. All of the authors contributed to the preparation of the listed manuscript.

To my mom, dad, and sister Jocelyn for their unconditional love and support. For always believing in me and cheering me on during this difficult and lengthy journey. You have been my rock and my rays of sunshine.

To my grandparents for their love, kindness, and guidance every day of my life.

ABSTRACT OF THE DISSERTATION

Multi-Scale Mathematical Modeling Study of Proper Shape Formation During Epithelial Tissue Development

by

Jennifer Rangel Ambriz

Doctor of Philosophy, Graduate Program in Mathematics
University of California, Riverside, September 2024
Dr. Mark Alber, Chairperson

This dissertation consists of two parts describing different mathematical and computational models developed for testing novel biological hypothesized mechanisms of *Drosophila* wing disc morphogenesis.

How a developing organ robustly coordinates the cellular mechanics and growth to reach a final size and shape remains poorly understood. Through iterations between experiments and model simulations that include a mechanistic description of interkinetic nuclear migration, in the first part, we show that the local curvature, height, and nuclear positioning of cells in the *Drosophila* wing imaginal disc are defined by the concurrent patterning of actomyosin contractility, cell-ECM adhesion, ECM stiffness, and interfacial membrane tension. We show that increasing cell proliferation via different growth-promoting pathways results in two distinct phenotypes. Triggering proliferation through insulin signaling increases basal curvature, but an increase in growth through Dpp signaling and Myc causes tissue flattening. These distinct phenotypic outcomes arise from differences in how each growth pathway regulates the cellular cytoskeleton, including contractility and cell-ECM adhesion. The coupled regulation of proliferation and cytoskeletal regulators is a general strategy to meet the multiple context-dependent criteria defining tissue morphogenesis.

In the second part, we develop a 2D mathematical model of actomyosin network dynamics, intended to extend the simplified representation of actomyosin in the Subcellular Element (SCE) model presented in the first part. During *Drosophila* wing disc organogenesis, the actomyosin network gives rise to contractility, a key force-generating mechanism that regulates cell shape changes and interkinetic nuclear migration (IKNM). Although experimental studies have shown that actomyosin contractility is a key driver of IKNM, not enough work has been done to investigate the exact mechanism(s) of how actomyosin produces the contractile forces that constrict the basal membrane and in turn, facilitate the nuclear migration. Because of this, we developed an actomyosin network model that captures a detailed description of the actin-myosin interactions and the directionality of the contractile forces. Once coupled with the SCE model, it will allow us to explore the mechanism(s) behind the basal narrowing of cells that drive the apical migration of nuclei and mitotic rounding during cell division.

Contents

List of Figures

List of Tables

Chapter 1

Introduction

1.1 Overview

The development of tissues and organs is a complex process that involves the integration of mechanical forces with complex chemical signaling networks at different spatial scales, from sub-cellular to cellular to tissue level scales. In addition, robust morphogenesis requires the coordination of various factors, including mechanical regulators, cell proliferation, cell death, and cell-environment regulations such as cell-cell and cell-substrate adhesions. A successful combination of all of these processes gives rise to the final tissue shape. However, dysregulation of any of these processes will hinder proper tissue or organ development and result in congenital disabilities and degenerative diseases. Since achieving the correct size and shape is critical for organ function, one of the central problems in developmental biology is understanding how an organ's shape is formed and maintained [2]. In particular, understanding the role of mechanical regulators (such as actomyosin) and cell proliferation in reaching the final tissue morphology is critical to understanding proper development. In this dissertation, we combine novel mathematical and computational models with experimental data to study organ development in the context of the *Drosophila* wing imaginal disc.

1.1.1 Organization of the Dissertation

This dissertation is organized as follows. First, a background section that reviews various mathematical and computational models is presented in this chapter. Then, in the introduction section of Chapters 2 and 3, a review of the biological background of each study is included.

In Chapter 2, we present a novel two-dimensional multi-scale mathematical and computational model for studying mechanisms of embryo tissue development of the *Drosophila* wing imaginal disc, which has been calibrated using experimental data. More specifically, we developed a multi-scale Subcellular Element (SCE) model that captures the morphology of the wing disc cross-section along the Anterior-Posterior axis by modeling the nuclei, different cell types, and the extracellular matrix as a set of several nodes interacting with one another through different energy potential functions. The positions of nodes are described via overdamped Langevin equations of motion. In other words, the motion of nodes is represented by solving stochastic ordinary differential equations using a forward Euler numerical scheme. The novelties of this model include the detailed representation of cell growth and proliferation, modeling the non-uniform spatial patterning of mechanical regulators, and capturing the actomyosin contractility in the apical and basal regions of columnar cells (one cell type in the wing disc). By combining our model with experimental work, we investigate how subcellular and cellular-level processes, such as mechanical regulators and cell proliferation, play a role in the formation of the overall shape of the wing disc.

In Chapter 3, we set the ground for extending the simplified representation of actomyosin contractility in the SCE model presented in Chapter 2. In particular, we develop a mathematical model of actomyosin network dynamics that captures an individual representation of actin filaments and non-muscle myosin II (pMyoII) mini-filaments, the biological components of the network. In addition, the model captures the actin-pMyoII interactions, which give rise to contractile forces. The goal is to couple this detailed network model with the SCE model to investigate how actomyosin gives rise to the contractile forces that constrict the

basal membrane at the onset of cell division, which drive the nuclear migration of mitotic nuclei to the apical region of the cells to divide successfully.

Both Chapters 2 and 3 conclude with a discussion section that summarizes the main results of each chapter and highlights some areas of future work. Finally, Chapter 4 contains the overall conclusions of our studies, where we discuss an exciting future direction and application of our presented work to study later stages of *Drosophila* wing development.

1.2 Mathematical and Computational Modeling Background

This section is a reproduction of Supplementary Information section S3.1 Overview of computational modeling approaches published in [1]. This section was written by me with the help of my advisor Dr. Alber, and collaborators, Dr. Chen and Dr. Tsai. Note that for the sake of organization and readability of this dissertation, subsection titles were added to the reproduced text from [1].

1.2.1 Mathematical Continuum Modeling Approaches

Multiple mathematical and computational modeling approaches varying from continuum to discrete cell-based models have been used to study epithelial tissue mechanics and morphogenesis [6]. For example, in Keller et al., a continuum model employing the finite element method was developed to reproduce deformation experiments on the *Drosophila* wing imaginal disc to investigate how geometry affects its elastic properties [85]. In Levis et al., a compression microfluidic device was developed to compress the wing imaginal disc, and a continuum computational model was used to estimate the elastic modulus of the disc based on the deformations occurring in the wing disc [86]. In particular, Levis et al. used a finite element model using the structural mechanics module of COMSOL [87] to simulate the wing disc cross section and show that the elasticity of discs increases with age. Recently, Harmansa et al. developed a continuum three-dimensional finite element model to study the bending of the *Drosophila* wing imaginal disc [25] to demonstrate that the domed

shape of the wing disc can be driven by the differential growth rate between the columnar cells and their associated basal ECM and not by the difference in growth rates between the columnar and peripodial tissue layers. In general, continuum modeling approaches are more appropriate to capture macroscale tissue-level phenomena and cumulative tissue mechanisms as they usually do not model cell-level properties and biological processes such as individual cell adhesion, division, and intracellular processes.

1.2.2 Cell-Based Mathematical and Computational Modeling Approaches

Unlike continuum models, discrete cell-based models simulate cell-level processes, such as cell-cell adhesion and individual cell division. Cell-based models can be categorized into either lattice or off-lattice modeling approaches (see Osborne et al. [61] and Honda and Nagai [88] for extended reviews). A lattice-based model such as the Cellular Potts model (CPM) represents a cell as a cluster of lattice sites that interact with one another via Monte Carlo rules based on changes in energy potentials. Among other biological problems, CPMs have been used to study morphogenesis, limb formation, cell aggregation, and cell sorting [65–68, 89, 90]. These types of models can efficiently capture a great number of cells and they are easy to implement computationally. In terms of off-lattice models, a well-established modeling approach is the vertex-based model, which represents cells as polygons composed of vertices connected by edges where each vertex moves under the action of the force term acting on it [60]. In Nagai and Honda [91], the vertex model was applied to study wound closure in epithelia and demonstrated that cell basal-lamina adhesion is responsible for proper closure. In other applications, the vertex-based modeling framework was applied to study cell shape formation, tissue morphogenesis, and regulation of tissue size [60, 70–75, 92]. For an extensive review of the vertex models and various applications, please see the book by Honda and Nagai [59].

Several previous computational models have been developed to study the impact of changing mechanical properties of epithelial tissue on its structure and shape [70, 91, 92]. A common setup in previous models is to describe the epithelial layer as a tightly connected

two- or three-dimensional structure composed of polyhedrons. As surveyed by Smallwood, earlier models can be traced back to the paper by Honda that describes the epithelial structure from a top-down view using Dirichlet domains [91, 93]. Subsequent models, either two-dimensional or three-dimensional, were developed utilizing geometrical techniques represented by topology dynamics, center dynamics, boundary dynamics, or vertex-based dynamics where an individual cell is depicted as a polyhedron [23, 24, 32, 59, 74, 94–97].

1.2.3 Physics-Based Mathematical and Computational Modeling Approaches

Physics-based models describing an epithelial cell layer where mechanical stress and elastic deformation are modeled via potential terms, stress-tensor, or continuum approach, are a key area of continued interest [59, 98–101]. These computational models have been used to provide insight into important biological questions including the formation of epithelial folding and invagination to identify potential mechanisms driving such processes. For instance, in the work of Marin-Riera et al., an off-lattice center dynamics model was developed to illustrate the ability to capture the interaction between an epithelial layer with its surrounding extracellular matrix (ECM), and how differential adhesion, cell migration, and cell contraction lead to tissue deformation [102]. A key aspect of these models is allowing different degrees of contraction at the apical and basal surface, regardless of the model dimension, to achieve deformation. However, such models often make simplified assumptions including but not limited to reducing the contacting surfaces between two neighboring cells into a single surface, and therefore reducing the flexibility of the lateral cell surfaces [12, 103]. In addition, it is also frequently assumed that the contraction is surface-bound, either apically or basally. For a detailed review of physical models developed to study folding and invagination, please see Rauzi et al [94].

1.2.4 Three-Dimensional Mathematical and Computational Modeling Approaches

Recently, Tozluoglu et al. developed a 3-dimensional finite element model where each individual cell in the *Drosophila* wing pouch is represented with triangular prisms, and growth is modeled by the increase in the volume of prisms, to study the mechanism for fold formation [23]. This model captures the ability of cells to resist deformation including shear strain. They conclude that external resistance to growth from the ECM is essential for buckling the tissue and the increased apical stiffness can induce the correct number of folds. Ioannou et al. developed a three-dimensional hybrid vertex model that allows a more complex polyhedron representation of the epithelial cells, improving the ability of capturing the packing of cells more realistically [104].

1.2.5 Coupled Mechanical and Chemical Signaling Models

There have also been models developed to identify the links between mechanical behaviors with the underlying chemical signaling pathways. The work by Hughes et al. has delved into how mechanical compaction of the extracellular matrix during mesenchymal condensation leads to tissue folding [105]. In the work of Zmurchok et al., a two-way feedback between signaling and mechanical tension was investigated to observe waves of contraction and relaxation sweeping through a two-dimensional model epithelium [106]. However, it still remains unclear how morphogenesis arises from the interplay between mechanical contraction and signaling networks. To fill this gap of knowledge, we specifically explore the relative contributions of cell proliferation and actomyosin contractility in regulating tissue curvature, cell height, and nuclear positioning.

1.2.6 SCE Modeling Approach and its Advantages

In this study, we use the general Subcellular Element (SCE) modeling approach, which was initially developed by Newman et al [76]. Here, we developed a novel multi-scale mathematical and computational model that allows us to study how changes in local

subcellular mechanical properties and cell proliferation regulate the dynamical changes in epithelial tissue geometry. The SCE method provides unparalleled resolution in describing detailed intra- and inter-cellular interactions including cell-cell adhesion and membrane-nucleus interactions (see Chapter 2 Fig 2.1) Previously, SCE type models have been utilized to study both the top-down and cross-sectional view of the epithelial layer in the *Drosophila* wing disc [24, 32]. While more computationally intensive, the SCE approach represents an interplay between cellular deformation due to contraction and the dynamics of subcellular components including the nucleus, which is often absent in more coarse-grained models. To overcome the computational cost, most models using the SCE approach have been parallelized on GPU computer clusters. One final and key advantage of the SCE model is that the cell mechanical properties can be directly calibrated based on experimental data [32, 80].

Chapter 2

A Multi-Scale Model of the Development of the *Drosophila* Wing Disc Cross-Section

2.1 Preface

The content of this chapter is a reproduction of our recently published paper, where I am one of three first authors: Nilay Kumar, Jennifer Rangel Ambriz, Kevin Tsai, Mayesha Sahir Mim, Marycruz Flores-Flores, Weitao Chen, Jeremiah J. Zartman, and Mark Alber. Balancing competing effects of tissue growth and cytoskeletal regulation during *Drosophila* wing disc development. *Nat Commun* **15**, 2477 (2024) [1]. Nilay Kumar and I led the manuscript writing and revisions. Nilay Kumar designed and performed experiments as well as analyzed the experimental data under the guidance of Jeremiah J. Zartman and with the help of Mayesha Sahir Mim and Marycruz Flores-Flores. Kevin Tsai developed and calibrated the original mathematical and computational models and performed initial simulations. I substantially extended the models, performed the simulations presented in the manuscript, and contributed to the data and simulation analysis. The design and creation of all figures and associated captions were a team effort, but mainly led by Nilay Kumar and I.

2.2 Introduction

The final shape of an organ is a result of the dynamic interplay between cell-level developmental processes [3–6]. A major challenge in reverse engineering biological systems arises from the inherent complexity of interactions governing protein regulatory networks and multicellular interactions that occur over multiple spatial and temporal scales [7–10]. In particular, regulating features such as local tissue curvature, cell height, and nuclear positioning is critical for controlling the morphogenesis of multicellular organisms [11–13]. Iteration of morphological changes such as epithelial folding and flattening results in the formation of an organ's final 3-D structure and function [14–16]. Untangling the regulation of multiple subcellular features that compete with each other and control morphogenesis requires systems-level, multi-scale approaches [15] that incorporate highly complex biologically calibrated computational model simulations coupled with quantitative experimental analysis [17, 18].

In this chapter, we decouple the roles of cell proliferation and spatiotemporal cytoskeletal regulation in facilitating shape changes during organ development by using the *Drosophila* wing imaginal disc as a model system. The wing disc is a pseudostratified epithelial vesicle comprising multiple cell types, including squamous, columnar, and cuboidal cells [19]. In early developmental stages, the wing disc undergoes rapid proliferation, starting from around 30 cells and maturing into an organ with approximately 35000 cells [19]. Wing disc cells are enclosed by an extracellular matrix (ECM) along with several cytoskeletal regulators that vary in structural functions. For instance, interactions between Actin and phosphorylated non-muscle myosin II (pMyoII) generate contractile forces necessary for interkinetic nuclear migration during cell division [13]. Further, β-Integrin (βPS) adheres the ECM to the cell basal surface [20]. Collagen IV (Col-IV), a key component of the ECM, maintains tensile strength and adhesion of cells with the ECM [21]. The dynamic regulation of the cytoskeleton is spatially patterned across the tissue. In particular, the wing disc starts as a flat tissue that thickens and acquires a dome shape as it grows in size. Further, shape

changes in individual cells can regulate morphogen signaling through feedback to pattern cytoskeletal regulators [22].

Forces generated in individual cells resulting from single-cell processes, including proliferation and cytoskeletal regulation, combine across a multicellular system to give rise to its shape. For instance, fold formation partially occurs due to differential cell proliferation rates [23]. Also, Nematbakhsh and Levis et al. found that patterning of actomyosin contractility along the apical-basal axis of pouch cells is necessary for generating the dome shape, and the ECM is critical for maintaining the shape [24]. Recently, Harmansa et al. demonstrated that variation between growth rates of the cellular and ECM layers in the *Drosophila* wing imaginal disc contributes to the bending of the tissue [25]. However, biophysical mechanisms that couple cell shape, cell mechanical properties, and proliferation are yet to be established fully [26, 27]. In the case of *Drosophila*, a fundamental question lies in determining the systems-level mechanism driving the formation and maintenance of wing disc shape during the larval stage and the connection between such shape acquisition with patterning of cell identities and cellular properties, including growth [14, 28, 29]. For example, Decapentaplegic (Dpp), a key morphogen that patterns the anterior-posterior (AP axis), activates and patterns the Rho family of small GTPases to generate a gradient in cell height through regulation of actomyosin contractility [11, 30]. Proper shape acquisition is critical for the fitness of the organism. For instance, the final wing shape is a crucial determinant in flight performance [31].

To test how spatial patterning of cell mechanical properties and cell proliferation impact the tissue shape, we developed and calibrated a multi-scale spatial mathematical and computational modeling approach incorporating the spatial patterning of fundamental subcellular properties, including subcellular mechanics and cell division dynamics. As a basis for our model, we adopted the general Subcellular Element (SCE) modeling approach [24, 32, 33], which was previously used to determine the role of basal contractility and spatially varying ECM stiffness in generating the bent shape of the wing disc [24]. In the model, we introduce a cell division module that captures the interkinetic nuclear migration and mitotic

rounding process within a pseudostratified epithelium [12, 13]. Combining experiments and computational model simulations, we demonstrate that key regulators of tissue curvature include the ratio of apical to basal contractility, ECM stiffness, and cell-ECM adhesion. Additionally, proliferation promotes increased tissue height and basal curvature. Surprisingly, analysis of multiple growth regulators reveals distinct subclasses that result in two very different phenotypic outcomes to growth stimulation: increased basal curvature or flattening of the tissue as growth increases. Consequently, the dual action of growth on proliferation and cytoskeleton generates the ability to regulate tissue size and shape as independent features.

2.3 Methods

2.3.1 Mathematical and Computational Modeling Background

Various mathematical and computational modeling approaches, ranging from continuum to discrete cell-based models [59], have been introduced to study tissue development and growth [6, 16–18, 59]. In the context of studying the *Drosophila* wing imaginal disc, continuum models employing the finite element method have been recently used to study the bending of the wing disc [25]. On the other hand, discrete cell-based models, classified as lattice-based or off-lattice models, have been successfully utilized to investigate different aspects of tissue growth and development [18, 60–64]. For example, the Cellular Potts modeling (CPM) method, a lattice-based approach, describes cells as clusters of lattice sites that change shape via energy-based Monte Carlo algorithms. This modeling approach has been used to study fundamental biological processes, including but not limited to morphogenesis, cell aggregation, cell sorting, and thrombus formation [65–69]. Off-lattice vertex-based models have been implemented to investigate tissue morphogenesis and the regulation of tissue size, among other biological applications [60, 70–75]. Although vertex and CPM models have been successfully used to study various biological systems, it is often hard to calibrate representations of cellular and subcellular mechanical properties in these models using

micro-scale experimental data [60, 65, 66]. In this chapter, we use the general off-lattice Subcellular Element (SCE) modeling approach, initially developed by Newman et al. [76] and based on the coarse-grained molecular dynamics method. It allows one to combine submodels at the micro-scale into a model by choosing appropriate levels of resolution, as well as represent mechanical properties and shapes of cellular membranes, nuclei, and the ECM in detail and calibrate the multi-scale model using experimental data at the subcellular, cellular and tissue scales. (For a more detailed review of different models, please see Chapter 1).

2.3.2 Description of the SCE Model

The general SCE modeling approach [24, 32, 33] was used as the basis for the model presented in this chapter. Here, our SCE-type multi-scale model in detail represents cell deformation and proliferation and integrates mechanical properties, including cell membrane elasticity, internal cell pressure, polarized actomyosin contractility with nuclear movement, and cell-cell and cell-ECM adhesivity. Another key advantage of this SCE modeling approach is that most of the cell mechanical properties considered can be directly or indirectly calibrated based on experimental data [32, 77]. This computational modeling framework is used to simulate a two-dimensional (2D) cross-sectional profile of the *Drosophila* wing imaginal disc along the anterior-posterior axis adjacent to the DV compartment boundary. Using a detailed 2D model allows for simulating large numbers of cells with high resolution and with particular attention to mechanical cell properties and small changes in tissue structure and shape. Given that the cross-section is composed of boundary cells, squamous cells, and columnar cells, the model includes a separate description for each cell type (Fig 2.1). Important distinctions from our previous model [24] are detailed representations of cell division and actomyosin contractility in different parts of a cell. The model includes membrane nodes, nucleus nodes, and ECM nodes. Energy potentials are used to describe interactions between different nodes, as in Nematbakhsh and Levis et al. [24]. The total potential energy in the general SCE model is calculated across node representations of different components of

individual cells, and the position of each node of interest is determined via the following Langevin equations of motion:

$$C_{nuc}\frac{d}{dt}\boldsymbol{x}_{nuc} = -(\nabla E_{nuc} + \nabla E_v) + \xi_s \tag{2.1}$$

$$C_{memb}\frac{d}{dt}\boldsymbol{x}_{memb} = -(\nabla E_{memb} + \nabla E_{memb,bend} + \nabla E_{api,cont} + \nabla E_{bas,cont} + \nabla E_v + \nabla E_{vol} + \nabla E_{adhL} + \nabla E_{adhB} + \nabla E_{adhA}) + \xi_s \tag{2.2}$$

$$C_{ecm}\frac{d}{dt}\boldsymbol{x}_{ecm} = -(\nabla E_{ecm} + \nabla E_{ecm,bend} + \nabla E_v + \nabla E_{adhB}) + \xi_s \tag{2.3}$$

where C_{nuc}, C_{memb} and C_{ecm} are damping coefficients and ξ_s is the stochastic force satisfying the Fluctuation-Dissipation Theorem [78]. In this chapter, we neglect the stochastic force term on the right-hand side of Eqs. 2.1 - 2.3 by setting $\xi_s = 0$ for two important reasons. First, the cells in the wing disc cross-section are part of a tightly packed tissue where the level of fluctuation of membranes is negligible. The second reason is that we use the coarse-graining approximation. Instead of modeling at the molecular level, a single node in our model represents a portion of cell nuclei, membrane, or ECM. Therefore, ξ_s is assumed to be zero as the mean behavior. Although for this specific application, we neglect the stochastic term, we plan to include the non-zero stochastic term and study its effect in our future extended model.

In the SCE model, a linear spring potential,

$$E_{memb} = \frac{1}{2}k_{memb}(L_{memb} - L0_{memb})^2 \tag{2.4}$$

where L_{memb} and $L0_{memb}$ are the lengths between connected nodes and the resting length respectively, is used to describe mechanical properties of the cell membrane (Fig 2.1 A-F). The E-cadherin mediated cell-to-cell adhesion between cells of the same type is captured by a linear spring potential (see Fig 2.1 E) defined by:

$$E_{adhL} = \frac{1}{2}k_{adhL}(L_{adhL} - L0_{adhL})^2 \tag{2.5}$$

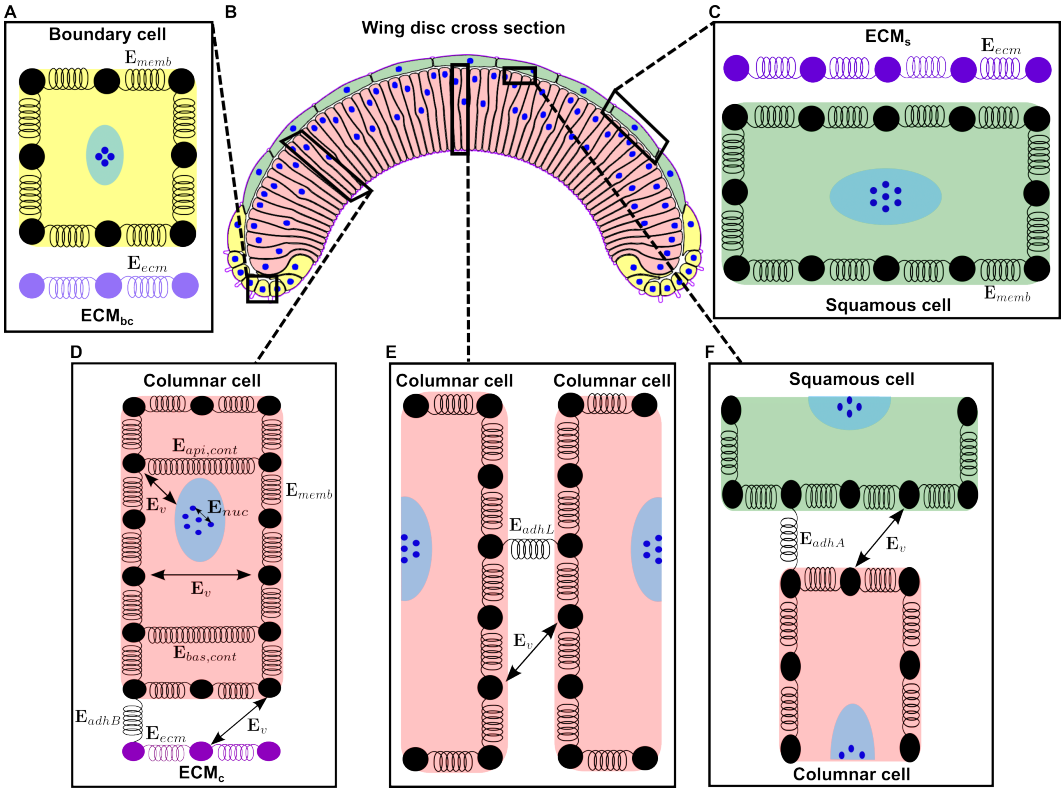

Figure 2.1: **Two-dimensional (2D) multi-scale subcellular element (SCE) model of the *Drosophila* wing disc cross-section along the anterior-posterior (AP) axis.** This model closely resembles the wing disc cross-section by including a representation of the three different cell types (boundary, squamous and columnar cells) that make up the cross-section and of the ECM, which connects to the basal surface of the cells. Simulated cells, nuclei, and ECM are represented by a set of nodes interacting via different potential energy functions. (A) Model representation of a boundary cell and its associated ECM denoted by ECM_{BC}. (B) Model simulation of the cross-sectional profile of the wing disc along the AP axis includes boundary cells (colored in yellow), columnar cells (colored in light red), squamous cells (colored in green), and the ECM (colored in purple). (C) Model representation of a squamous cell and its respective ECM denoted by ECM_S. (D) Model representation of a columnar cell with different potential energy functions that capture intracellular interactions, apical and basal actomyosin contractility and cell interactions with the ECM (denoted by ECM_C). Although we only use a single spring to represent the apical ($E_{api,cont}$) and basal ($E_{bas,cont}$) contractility in (D), in the model there are actually several apical and basal contractile springs. See section "Determination of the Number of Springs in Non-Mitotic Cells" for details. (E) Adjacent columnar cell nodes interact via linear spring E_{memb} and Morse potentials E_v to maintain the cells closely connected without the membranes overlapping. (F) The apical membrane of columnar cells is connected to squamous cells.

Similarly, the adhesion between squamous and columnar cell membrane nodes is defined by the energy potential

$$E_{adhA} \;=\; \frac{1}{2}k_{adhA}(L_{adhA} \;-\; L0_{adhA})^2 \tag{2.6}$$

while the membrane-to-ECM adhesion mediated by Integrin is defined by

$$E_{adhB} \;=\; \frac{1}{2}k_{adhB}(L_{adhB} \;-\; L0_{adhB})^2 \tag{2.7}$$

(see Fig 2.1 D, F). To account for membrane bending resistance, a bending spring potential

$$E_{memb,bend} \;=\; \frac{1}{2}k_{memb,bend}(\theta_{memb} \;-\; \theta_0)^2 \tag{2.8}$$

is defined where θ_{memb} is the angle between two connected linear springs, and θ_0 is the resting angle between two connected linear springs [24, 32]. The ECM (E_{ecm}) is also modeled similarly via placing a spring between adjacent ECM nodes (Fig 2.1 D-F, see later subsection entitled "Modeling the Extracellular Matrix") to account for both stretching and bending resistances. Note that for the ECM, the bending spring potential is defined as:

$$E_{ecm,bend} \;=\; k_{ecm,bend}(1 \;-\; \cos{(\theta_{ecm} \;-\; \theta_0)}) \tag{2.9}$$

where θ_{ecm} and θ_0 represent the current and resting angles between two connected ECM linear springs [24]. Volume-exclusion (E_v) between different types of nodes is described by the Morse potential:

$$E_v \;=\; U_v \exp\left(\frac{-|\boldsymbol{x}_i \;-\; \boldsymbol{x}_j|}{\xi_v}\right) - W_u \exp\left(\frac{-|\boldsymbol{x}_i \;-\; \boldsymbol{x}_j|}{\gamma_u}\right) \tag{2.10}$$

where $\boldsymbol{x}_i$ and $\boldsymbol{x}_j$ are vectors representing the positions of nodes i and j and U_v, ξ_v, W_u and γ_u are the Morse coefficients [24, 32].

Since we introduce apical actomyosin contractility in this chapter, an additional linear spring energy potential term is introduced in Eq. 2.2 and denoted by $E_{api,cont}$. In this way,

we capture actomyosin contractility in the apical ($E_{api,cont}$) and basal ($E_{bas,cont}$) parts of a columnar cell (Fig 2.1 D). Note that

$$E_{api,cont} = \frac{1}{2}k_{api,cont}(L - L0_{api,cont})^2 \tag{2.11}$$

$$E_{bas,cont} = \frac{1}{2}k_{bas,cont}(L - L0_{bas,cont})^2 \tag{2.12}$$

where L represents the lengths between connected nodes while $L0_{api,cont}$ and $L0_{bas,cont}$ are the resting lengths of the apical and basal contractile springs, respectively. It is important to highlight several contractile springs in the apical and basal regions of columnar cells and that the number of springs is cell-dependent. For a detailed explanation of how the number of springs is determined, please see later subsection "Determination of the Number of Springs in Non-Mitotic Cells". For completeness, we reproduced the table of energy potentials Table 2.1 from our previous publication [24], with the addition of the description of the new potential $E_{api,cont}$, in order to provide a detailed description of the potential functions in the right-hand side of Eqs. 2.1–2.3.

Given that it is valid to assume that cellular motion is under an overdamped regime for most biological systems [24, 32, 79, 80], we assume that the nodes in our wing model are also in an overdamped regime. In this way, the inertia force acting on each node is neglected. Moreover, Eqs. 2.1–2.3 include a damping coefficient (C_{nuc}, C_{memb}, C_{ecm}) to account for the viscous drag acting on each node due to the surrounding environment. (A detailed description of the types of potential energies and model construction can be found in Table 2.1, Nematbakhsh and Levis et al. [24] and Appendix A subsection A.4.2 "Model Calibration Pipeline"). The parameter ranges of this computational model have been calibrated using a combination of experimental data from this study and from literature (Appendix A Tables A.1 - A.4). Various parameter values were taken from our previous publications (Nematbakhsh and Levis et al. [24], Nematbakhsh et al. [32]), where they were calibrated based on specific experimental results. Parameters such as spring constants, which are not biological, have been calibrated by comparison with specific experiments and

Potential function	Type	Biological representation
E_{nuc}	Morse potential	Size of a cell's nucleus
E_v	Morse potential	Volume exclusion
E_{memb}	Spring	Elasticity of the cell membrane
$E_{memb,bend}$	Bending Spring	Bending Elasticity of the cell membrane
$E_{api,cont}$	Spring	Apical actomyosin contractility inside the cells and above the nucleus
$E_{bas,cont}$	Spring	Basal actomyosin contractility inside the cells and below the nucleus
E_{vol}	Lagrange Multiplier	Volume conservation of the cytoplasm for each cell
E_{adhL}	Spring	Cell-cell adhesion mediated by E-cadherin
E_{adhB}	Spring	Cell-ECM adhesion mediated by Integrin
E_{adhA}	Spring	Adhesion between columnar and squamous cells
E_{ecm}	Spring	Extracellular matrix stiffness
$E_{ecm,bend}$	Bending Spring	Extracellular matrix bending stiffness

Table 2.1: Energy potentials used in the SCE model

experimental data. In addition, we used actin and pMyoII intensities quantified in this study to calibrate the number of springs and spring coefficients, respectively, associated with the apical and basal contractility. To ensure that the parameter values were in agreement with experimentally quantified data, we relied on three metrics for calibration: (1) local basal curvature, (2) tissue thickness, and (3) nuclear positioning (Fig 2.2 B). (A detailed description of our calibration pipeline can be found in Appendix A subsection A.4.2 "Model Calibration Pipeline").

2.3.3 Nonuniform Apical and Basal Actomyosin Contractility

A feature of the current model represents the nonuniform spatial patterning of actomyosin contractility in the apical and basal parts of a cell. Namely, interactions between actin and myosin lead to the formation of a contractile force that creates constriction in the apical and

basal portions of the columnar cells. In our computational model, this constriction effect is represented by the contractile springs linking the lateral sides of a columnar cell. Note that the interaction between actin and myosin is mostly membrane-bound, and therefore, the contractile force is exerted on the membrane surface, altering the circumference of the cross-sections of each columnar cell.

While such contractile forces may manifest themselves in multiple directions, we only considered the apical and basal contractile forces that are perpendicular to the apical-basal direction, which constrict the lateral sides of the cells, as the dominant factor giving rise to the elongated rectangular geometry of the columnar cells. Therefore, in a 2D setting, this circumferential contractile force is projected on the 2D plane where our cross-sectional model tissue resides in the form of linear springs. Thus, there is no direct interaction between the nuclei and the contractile springs, although some model simulations may falsely suggest otherwise. The contractile force exerted by the actomyosin network on the cell membrane is therefore described by the linear spring potential, $E_{*,cont} = \frac{1}{2}k_{*,cont}(|x| - x_0)^2$, where x is the distance between a pair of membrane nodes connected by the contractile spring. A detailed description of the application for the nonuniform actomyosin patterning can be found in the following section and the last section.

2.3.4 Spatial Representation of the Model of the Imaginal Wing Disc

The cross-sectional view of a wing disc can be separated into approximately left, middle, and right regions. The middle section is often found to be relatively flat in comparison to the left and right sections. At the same time, significant bending is observed at the junctions between the three sections (Fig 2.3). Based on this observation, we first simplified our assumption of the nonuniform basal and apical contractility patterns as a step function. For details of the computational model related to membrane stiffness and membrane-to-membrane adhesion, please see [24]. To systematically study the effect of perturbing both apical and basal actomyosin contractility, we divided the columnar cells of the model tissue into three uniformly spaced sections, for example, the apical contractility profile is set to be $(a,\ 1.0,\ a)$

and the basal contractility profile is set as $(1.0,\ a,\ 1.0)$ where $0 \leq a \leq 1.0$ (Fig 2.4 E-i, Appendix A Figs A.7, A.8). These manually chosen nonuniform patterns of actomyosin contractility are utilized to perform model validation. Such validation is necessary to confirm that the resulting physical behavior of the model is plausible and helps narrow down the range of possible perturbations to evaluate. These simulation results are in good agreement with experimentally observed tissue shapes (Fig 2.4).

2.3.5 Modeling the Extracellular Matrix

This subsection is a reproduction of the Supplementary Information section S-3.4 of [1], which describes in detail how the ECM is modeled.

The ECM is divided into three sections to represent the ECM associated with each cell type: the columnar cells (ECM_c), the boundary/cuboidal cells (ECM_{bc}) and the squamous cells (ECM_s) (Fig 2.1 A, C, D). The forces applied to the ECM are as follows:

$$F_{ecm,c} = k_{ecm,c}(L - L0_{ecm,c}) + c_1 \tag{2.13}$$

$$F_{ecm,bc} = k_{ecm,bc}(L - L0_{ecm,bc}) + c_2 \tag{2.14}$$

$$F_{ecm,s} = k_{ecm,s}(L - L0_{ecm,s}) \tag{2.15}$$

The constants c_1 and c_2 in the equations 2.13 and 2.14 are added to represent the pre-strain of the basal ECM. This representation of prestrain is equivalent to the one used in Adam et al. [83]. The values of c_1 and c_2 were chosen based on obtaining simulated cell and tissue shapes that qualitatively reproduce the bent shape of the wing pouch as shown in experimental images (Appendix A Tables A.1 - A.4). Previous biological studies also suggest that collagen fibers, key components of ECM in most of the organs, are under tension both prior to and during experiencing loads [84].

2.3.6 Cell Growth and Mitotic Rounding

Several key features were developed to study the effect of cell growth and division on the shape generation of the wing disc. Such features include cell growth via the increase of cell volume, mitotic rounding events, cell division, and an increase of the ECM nodes within the model. The volume conservation (or constraint) in the existing model utilizes a Lagrange multiplier energy function,

$$E_{vol} \;=\; k_{vol}(\Omega \;-\; \Omega_0)^2 \tag{2.16}$$

where k_{vol}, Ω and Ω_0 are the strength of the enforcement of volume constraint, current cell volume, and target (equilibrium) cell volume, respectively. To represent the increase in cell volume during cell growth, the equilibrium cell volume is increased linearly by a fixed value per simulation time step, namely $\Omega_0^{new} \;=\; \Omega_0^{init} \;+\; \epsilon T$. Here $\epsilon << 1$ is a small positive real number representing the increment in volume per simulation time step, T is the current total simulation time, and Ω_0^{init} is the equilibrium cell volume at the starting time point of cell growth. Furthermore, the maximal value Ω_0^{max} for Ω_0^{new} is set based on the expected cell volume before cell division occurs. Note that $\Omega_0^{max} \;<\; 2\Omega_0^{init}$ since the cross-section of the cell does not double even if the 3D volume is doubled. New ECM nodes are added locally when a certain portion of the ECM exceeds a fixed tension threshold, which arises due to individual cellular growth and division. This growth mismatch ensures that the cellular growth in the columnar epithelial layer is always greater than the ECM growth because the addition of ECM nodes depends upon the ECM's stretching due to the addition of new daughter cells from cell division. This model assumption is equivalent to growth in the columnar cell layer, which is upstream (and faster) than the ECM, following the mechanism described in Harmansa et al. [25].

2.3.7 Modeling the Basal Constriction Effect and the Dynamics of Actomyosin Patterning During Mitotic Rounding

Mitotic rounding in the *Drosophila* wing disc is special because the columnar cells experience an increased basal constriction that eventually pushes the majority of the cell interior content apically. This leads to an enlarged sphere at the apical side whose diameter is roughly a four-fold increase compared to the non-growing cell [32]. During this process, it was experimentally observed that the enrichment of actin and myosin concentration occurred near the basal section of the cell. This increased constriction effect is modeled as a time-dependent gradual increase in the number of actomyosin contractile springs in the existing model (Fig 2.4 E-i) using the equation $H_0^{new} = H_0^{init} + hT$. Here H_0^{init} is the value at the basal point calculated as the average of the membrane node coordinates in the basal portion of the cell, $h << 1$ is a positive real number representing the increment per simulation time step in actomyosin network buildup, and T is the current total simulation time. h is approximated by using the experimentally observed mitotic rounding time duration and the portion of a mitotic rounding cell with high intensity of actomyosin presence at the onset of cell division (Fig 2.2 D, E). In this way, a contractile spring is active when the distances from the membrane nodes connected by such contractile spring to the basal point (H_{cont}) satisfy $H_{cont} < H_0^{new}$. Therefore, as H_0^{new} increases, the number of contractile springs also increases. The strength of the contractile springs is also increased to increase the constriction effect further. This combined effect would correspond to the increased actin and myosin concentration observed during the mitotic rounding process. Finally, at the end of the mitotic rounding process, we restore the value of the contractile spring constant to the initially prescribed value and assume that the actin concentration undergoes a restoration from a depolymerized state back to a pre-mitotic state.

2.3.8 Modeling Cell Division Process

Cell division is modeled by constructing a division plane based on the centerline of each cell. Since the cell geometry can become rather distorted when simulating the mitotic rounding

process, the division plane has to be carefully crafted. This was achieved by calculating the midpoints of the cell. These midpoints are based on the corresponding pair of nodes positioned at the two lateral sides of a given model cell. Given such a centerline, new cell membranes in the model can be constructed by shifting the centerline slightly toward the two lateral sides, leading to two separate cells. This algorithm also corresponds to the scenario in that the planar orientation of the mitotic spindle is established as observed in the wild-type tissue, leading to the division along the lateral direction.

Each cell that can undergo cell growth and division was assigned an initial growth progress (GP) value $GP_0 < 1$. Such value was increased by a fixed value $\delta << 1$ per simulation time step. A cell in the model is considered to enter the mitotic rounding process when $(GP_0 + \delta T) > GP_{mit}$, where T is the current total simulation time, and GP_{mit} satisfying $GP_0 < GP_{mit} < 1$ is a threshold value. When $(GP_0 + \delta T) \geq 1$, the cell is considered to reach the end of the M phase of the cell cycle leading to subsequence cell division. To ensure that premature cell division with respect to cell volume increase does not occur, the small increments used in the cell volume and actomyosin contractile spring are calibrated so that the cell growth and division process can be completed in a timely manner. After a division event completes, the resulting cells are assigned a new GP value to indicate how fast such cells will undergo the mitotic rounding and cell division process again.

To ensure numerical stability in our simulations, the advancement in the cell cycle of a given cell is suspended if its immediate neighboring cell is already undergoing mitotic rounding and cell division. In terms of biological relevance, this is equivalent to the assumption that cells under high external stress are prevented from entering the mitotic phase. Lastly, in the simulation results presented in this chapter, each cell can perform a maximal number of 10 cell divisions.

2.3.9 Modeling the Introduction of a New Cell in the Cross-Section as Part of the Cell Division Process

At the end of cell division, a random number is generated to determine whether a new cell is introduced into the same plane (or cross-section). Since cell division can produce a new cell that would lie within the same cross-section or outside of the cross-section, it is necessary to consider both in-plane and out-of-plane cell division. The probability of this event can be experimentally approximated by calculating the frequency of new cells occurring in the same cross-section post-division. If a new cell is not introduced in the same cross-section post-cell division, the equilibrium volume is restored to the original value Ω_0^{init} by a method discussed in an earlier section, except we use expression $\Omega_0^{new} = \Omega_0^{postdiv} - \epsilon T$ where $\Omega_0^{new} \geq \Omega_0^{init}$.

Due to the unique mitotic rounding process, special care was taken to ensure numerical stability (Fig 2.2 D, E). Since columnar cells in the model are tightly packed and experience an increase in cell volume during mitotic rounding, volume exclusion is manipulated to prevent membranes from different cells from overlapping. This is done via a temporary but significant increase in the magnitude of the volume exclusion energy potential coefficient which becomes active as a cell enters the mitotic process and briefly post cell division.

As described earlier, the number of contractile springs corresponds to the presence of actin filaments found throughout the wing disc. In this model, we use the actin intensity (or concentration) observed in experiments to determine the number of contractile springs per cell in the model. An additional simplification was applied by calculating the average value of the recorded intensity according to its corresponding spatial position on the wing disc (Fig 2.2). However, this simplification can be discarded if the actomyosin intensity is governed by a time-dependent chemical signaling mechanism, and individual intensity can be prescribed to each cell.

2.3.10 SCE Model of Nuclear and Cell Shape Dynamics During Organ Growth

How morphogenesis arises from the interplay between mechanical contraction and signaling networks remains unclear. To fill this knowledge gap, we specifically explore the relative contributions of proliferation and actomyosin contractility in controlling curvature, height, and nuclear positioning. During actomyosin contraction, pMyoII is responsible for bringing actin filaments closer to each other, generating the contractile force. Such a force also depends on the availability of actin filaments [81]. The model incorporates actin density by utilizing a certain number of (linear) contractile springs in different parts of each cell. The impact of myosin on actin is represented by the spring constant of a contractile spring. In this chapter, we consider both apical and basal contractility.

2.3.11 Determination of the Number of Springs in Non-Mitotic Cells

This subsection is a reproduction of the Supplementary Information section S-3.3 of [1] since this section describes in detail how the number of contractile springs was determined.

The number of apical and basal actomyosin contractile springs within a non-mitotic cell depends on the height of the cell (H_{cell}) and the local actin intensities. To determine the number of springs, we first need to determine the apical and basal portions of a cell that can be occupied by springs. Measuring from the apical side of a cell, the apical contractile spring height is denoted by H_0^{api}, which defines the upper region of the cell where apical springs can exist (Fig 2.2 C, right panel, apical light blue region). Similarly, measuring from the basal point of a cell, we have the basal contractile spring height H_0^{basal} (Fig 2.2 C, right panel, basal dark blue region). The exact values of H_0^{api} and H_0^{basal} at the current iteration are determined by the local actin densities. More specifically, we assume that $H_0^{api},\ H_0^{basal} \leq 0.3H_{cell}$ and define $H_0^{api} = \alpha_i H_{cell}$ and $H_0^{basal} = \beta_i H_{cell}$. The weight constants α_i is defined by $\alpha_i = 0.3(A_i/A_{max})$ where A_i and A_{max} represent the local apical actin intensities and the maximum apical actin intensity, respectively. The calculation for β_i is similar to α_i, except we utilize the local and maximum basal actin intensities. Finally, a

contractile spring becomes active if the distance between the apical point of the cell and the nodes connected by the contractile spring is less than H_0^{api} or greater than $H_{cell} - H_0^{basal}$. If this distance is less than H_0^{api}, an apical contractile spring will manifest in the upper portion of the cell while if the distance is greater than $H_{cell} - H_0^{basal}$, then a basal contractile spring becomes active.

2.3.12 Experimental and Image Analysis Methods

All of the experimental and image analysis in this chapter was conducted by members of Dr. Zartman's lab and mainly led by Nilay Kumar. These methods are described in the following sections 2.3.13 - 2.3.17 accordingly.

2.3.13 Fly Stocks and Culture

Drosophila were raised in a 25 ° C incubator with a twelve-hour light cycle unless specified otherwise. Virgins from Gal4 lines were collected twice a day from the bottles. Virgins were crossed with males carrying the indicated UAS line constructs in a ratio of females to males 15:5. The crosses were staged for 4 h to collect the correct aged larvae. The wild-type Oregon-R fly line is a long-standing stock in the Zartman lab acquired from the N. Yakoby lab. The following transgenic stocks were obtained from Bloomington Drosophila Stock Center (BDSC): UAS-RyR$^{\mathrm{RNAi}}$ (BDSC#31540), UAS-InsR$^{\mathrm{DN}}$(BDSC#8253), UAS-InsR$^{\mathrm{CA}}$(BDSC#8263), UAS-Tkv$^{\mathrm{RNAi}}$ (BDSC#31041), UAS-Tkv$^{\mathrm{CA}}$(BDSC#36537), Nubbin-Gal4 (BDSC#25754), Engrailed-Gal4 (BDSC#25752), UAS-Myc (BDSC#9674), UAS-mTOR$^{\mathrm{RNAi}}$ (BDSC#33951), UAS-Myc$^{\mathrm{RNAi}}$ (BDSC#25783), and UAS-mTOR$^{\mathrm{DN}}$ (BDSC#7013).

2.3.14 Immunohistochemistry

Wing imaginal discs were dissected as described in previous publications [24]. Details of methods and reagents are found in section A.6 Experimental Methods of Appendix A.

2.3.15 Confocal Microscopy

The wing imaginal discs were imaged using a Nikon Eclipse Ti confocal microscope with a Yokogawa spinning disc and MicroPoint laser ablation system, and a Nikon A1R-MP laser scanning confocal microscope. For the two confocal microscopes, image data were collected on an IXonEM+colled CCD camera (Andor Technology, South Windsor, CT) using MetaMorph v7.7.9 software (Molecular Devices, Sunnyvale, CA) and NIS-Elements software, respectively. Discs were imaged throughout the entire depth of z-planes with a step size of 0.8-1 μm, depending on sample thickness, with a 40x and 60x oil objective with 200 ms exposure time, and 50 nW, 405 nm, 488 nm, 561 nm, and 640 nm laser exposure at 44% laser intensity. The imaging was performed from apical to basal surface so that peripodial cells were imaged first, followed by the columnar cells of the wing disc. Optical slices were taken at distances equaling half the compartment length. Tiling was performed on images to get the entire sample in the field of view, and QuickStich [52] was utilized to stitch individual tiles.

2.3.16 Image Analysis

For the Oregon-R staging data, CSBDeep [53] was used on the Actin fluorescent channel for denoising (Figs 2.2-2.6). For visualization purposes, the background subtraction of the pMyoII channel data was done using a rolling ball algorithm in ImageJ [54]. Intensity values for quantifications in this chapter were measured using the raw data without any image corrections. Brightness and contrast adjustments were made to minimize saturation during the visualization of Rho1 data for InsR and Tkv genetic perturbations (Figs 2.8 and 2.9). Analysis of curvature at the basal surface of a *Drosophila* wing imaginal disc cross-section was carried out using an in-house Python-based pipeline described in Appendix A subsection A.5.1 "Quantification of Local Basal Curvature" (Appendix A Fig A.23). StarDist [55], an open-source ImageJ plugin, was used to segment the nuclei. Details about quantifications of cell height and nuclear positioning can be found in Appendix A section A.5 Image Analysis and Data Quantification Pipelines (Appendix A Figs A.24, A.25).

2.3.17 Statistics and Reproducibility

We performed a two-sided two sample t-test to compare the significance of differences between the means of any two groups of data. For each comparison, we have reported the following statistics: the t-statistic, p-value, mean difference, and the lower and upper bound of the 95% confidence interval for the mean difference [56]. For comparison of curvature profiles, a t-test was additionally followed by a Cohen's d [57] measure to account for the large number of points in averaged curvature profile. We report t-statistic, p-value and Cohen's d measure for estimating the practical significance of comparison. All the statistical tests were carried out using Python's Scipy [58] module. Please see Appendix A subsection A.8.1 "Statistical Tests Employed in Chapter 2" for detailed statistics tables corresponding to specific figures within this chapter.

2.4 Results

2.4.1 The Role of Proliferation and Cytoskeletal Regulation in a Pseudostratified Epithelium

Here, we developed a computational model, combined with experiments, to test hypothesized mechanisms of shape changes in the wing imaginal disc during growth. In particular, we developed an SCE model that captures the shape of individual cells and overall wing disc morphology along the AP direction near the DV boundary (Fig 2.2 A-i). We also quantified important metrics defining the cross-sectional shape of the wing along the anterior-posterior axis (Fig 2.2 Bi-iii). In our previous work [24], it was assumed that actomyosin contractility is patterned uniformly across the apical and basal surfaces of the pouch. However, our experimental analysis (Figs. 2.2C and 2.3) of major cytoskeletal regulators reveals the nonuniform spatial patterning of mechanical regulators such as Actin, pMyoII, and Integrin (specifically βPS) across the AP axis. In particular, Actin, pMyoII, and βPS are more concentrated at the lateral basal ends than in the medial domain of the pouch at later stages of development (84 h AEL and later) (Fig 2.2 C). To test the significance of this

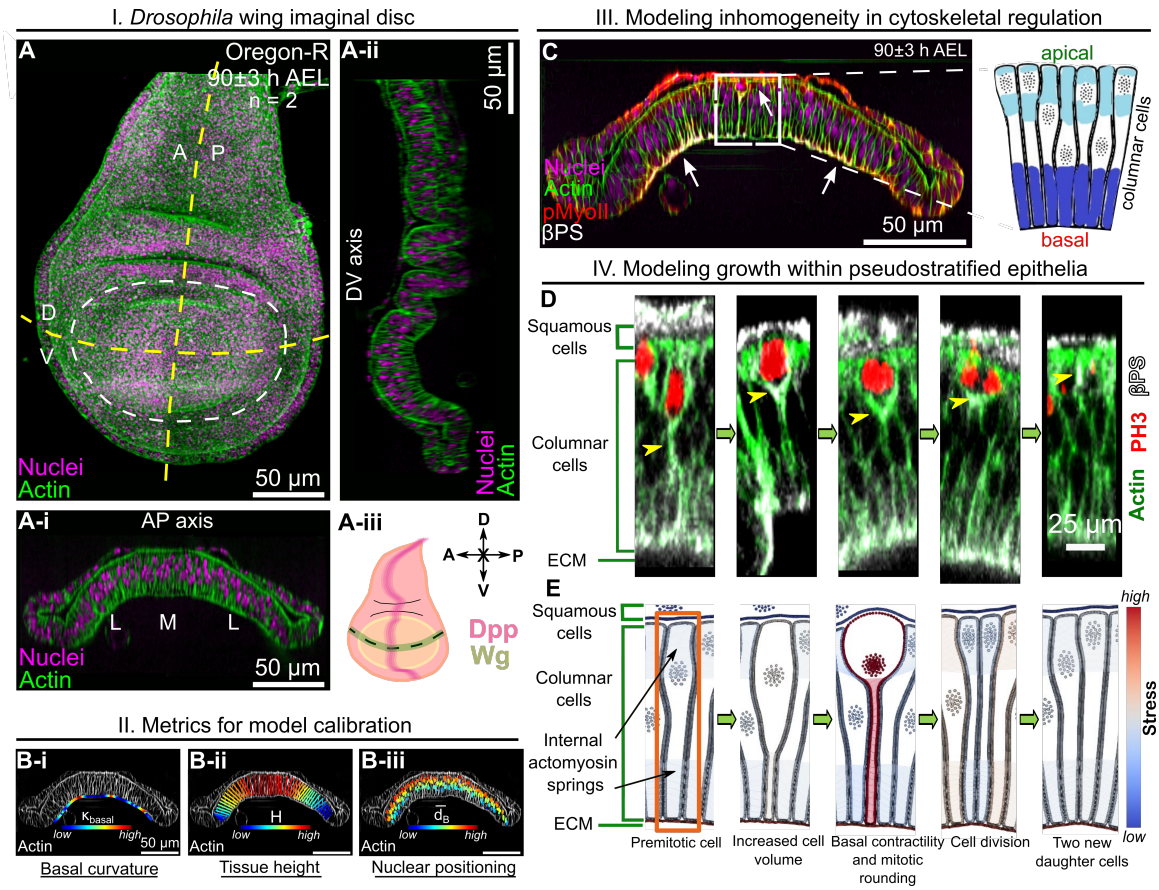

Figure 2.2: **Multi-scale Subcellular Element (SCE) model simulation of proliferation in a pseudostratified epithelium predicts proliferation dynamics and cytoskeletal regulation.** (A) Maximum intensity z plane projection showing the apical view of a wing imaginal disc at 90 h after egg laying (AEL). (A-i, A-ii) Cross-sectional views of the wing imaginal disc running parallel along the Anterior-Posterior (AP) and Dorsal-Ventral (DV) boundaries, respectively. The tissue is further divided into three equal parts, and the medial (M) and lateral (L) domains are defined in (A-i). (A-iii) A schematic illustrating patterning of the key morphogens, Decapentaplegic (Dpp) and Wingless (Wg). The inset on top-right specifies compartment orientation for data visualization and analysis. (B) Geometrical features defining the global tissue architecture include i. Local basal curvature (κ_{basal}), ii. tissue thickness (H), and iii. relative nuclear distance from the basal surface ($\bar{d}_B = \frac{d_B}{d_A+d_B}$). The color code represents low to high numerical quantity. (C) Computational model incorporating spatial inhomogeneity of cell mechanical parameters. Parameters are determined based on experimental quantification. (D) Stages of interkinetic nuclear migration during cell division in wing disc cells. Yellow arrows show observed concentrations of Actin and βPS below the dividing cell. (E) Computational snapshots of a simulated columnar cell undergoing division. Black arrows point to the various apical and basal actomyosin contractile springs within the columnar cells.

asymmetry in cytoskeletal regulation in defining tissue morphology, we developed simulations that include spatial variation of cell-level mechanical properties. This spatial patterning of parameters across the AP axis for each cell is the first innovation of our previous work [24].

Previous studies only allowed investigations of shape regulation at a single developmental stage and without spatial patterning of individual cell properties. As a second key innovation, we created the first SCE model that provides detailed simulations of cell proliferation and growth within a pseudostratified epithelium throughout the stages of organ development. The model of cell division includes multiple stages of interkinetic nuclear migration (Fig 2.2 D, E). During mitosis, the cell experiences narrowing of the basal section due to actomyosin contractility and depolymerization of the apical contractile springs. Consequently, the mitotic nucleus migrates towards the apical surface of the pouch. After division, the apical and basal contractile springs of the two new daughter cells are restored to pre-division values (Fig 2.2 E). Interestingly, both βPS and Collagen IV (Col-IV), key components of ECM-cell adhesion, form prominent tails below dividing cells (Fig 2.2 D, Appendix A Fig A.1). This may suggest that the basolateral surface of mitotic cells is pulled close to the bottom of the rounded cells during cell division to maintain a continuous structure for the epithelium to prevent delamination or excessive cell rearrangement.

Next, we developed a pipeline to calibrate the SCE model with the quantified experimental data for model calibration using local shape features such as basal curvature (κ_{basal}), tissue thickness (H), and nuclear positioning ($\bar{d}_B$) (Fig 2.2 B-i, B-ii, B-iii). The computational model, along with the quantification of experimental data, enables us to reverse engineer mechanisms governing organ shape and size regulation.

2.4.2 Both Cell Height Thickening and Tissue Flattening Occur Towards the End of Larval Wing Disc Maturation

Experimental analysis of staged wing discs reveals cell height thickening and flattening of the medial basal surface of the pouch. In particular, shape changes are correlated with changes in cytoskeletal regulation. To understand the interrelationships between tissue

growth and morphology, we quantified wing disc shapes over multiple time points leading up to pupal stages (72-96 h AEL, Fig 2.3 A, B). Basal curvature (κ_{basal}) along the DV boundary shows transitions from a relatively flat tissue (<72 h AEL) (Appendix A Fig A.2) to acquire a curved shape with almost uniform curvature (72-84 h AEL) (Fig 2.3 B, Ci-ii, top panel). The disc then continues to grow in size with increased bending in the lateral regions and flattening in the medial domain (84-96 h AEL) (Fig 2.3 B, Ciii-v, top panel). This central flattened section increases in width as development progresses (Fig 2.3 C, top panel). Moreover, cell height varies (Fig 2.3 C, bottom panel) across both the medial and lateral domains of the pouch.

Our results also indicate a change in the spatial patterning of cytoskeletal regulators throughout development (Fig 2.3 D-F'). In particular, the relative levels of pMyoII shift apically in the pouch's medial region as the discs grow (Fig 2.3 D i-v, E). Similar to pMyoII, βPS also undergoes temporal changes across the pouch basal surface (Fig 2.3 D' i-v). During the initial stages of development, βPS is localized along the basal surface with increased localization in the medial regions. As the pouch grows in size, it becomes more dominantly localized across the lateral regions of the pouch (Fig 2.3 E'). The strong correlation of Actin, pMyoII, and βPS along the basal surface of pouch cells suggest potential functional associations between the different cytoskeletal components (Fig 2.3 F, F', Appendix A Figs A.4, A.5). Additionally, the ratio of apical to basal levels of pMyoII strongly correlates with tissue height at later stages of morphogenesis (Fig 2.3 G, G'). Further, βPS localization correlates with the basal tissue curvature. Overall, the regions within the basal surface of epithelia that have higher localization of βPS have higher basal curvature (Fig 2.3 H, H'). While local cell height exhibits a strong correlation with the ratio of apical to basal pMyoII for discs at later stages of development (Fig 2.3 G'), it cannot be conclusively asserted that this relationship is the exclusive mechanism of cell height regulation across the pouch AP axis. This point stems from the observation that columnar cell height decreases when transitioning away from the medial pouch domain in younger discs (Fig 2.3 C-I, bottom panel), despite a relatively constant apical to basal pMyoII ratio across the pouch AP axis

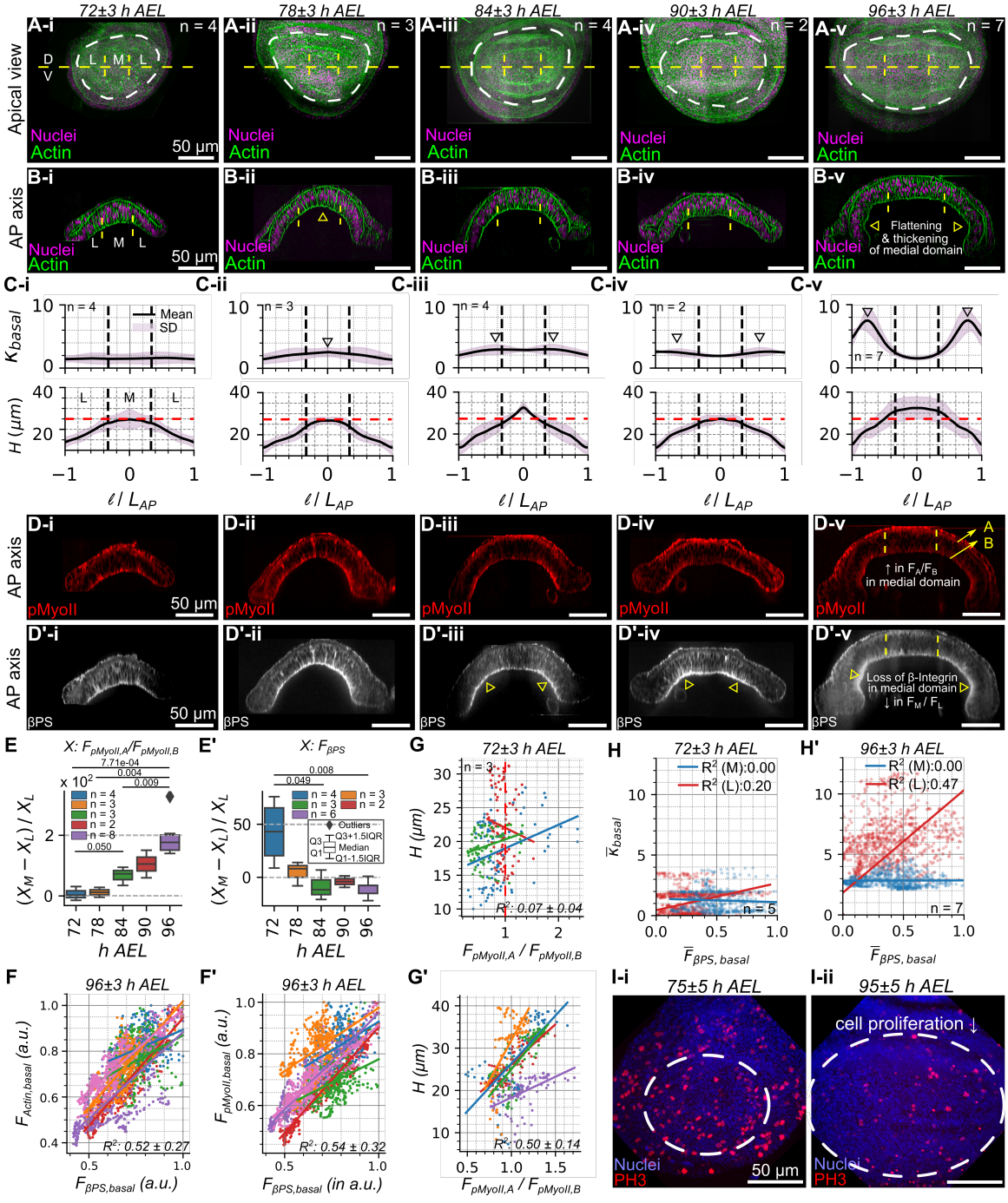
72±3 h AEL
78±3 h AEL
84±3 h AEL
90±3 h AEL
96±3 h AEL
Apical view
AP axis
Nuclei
Actin
50 µm
Flattening & thickening of medial domain
Mean
SD
pMyoII
↑ in F_A/F_B in medial domain
βPS
Loss of β-Integrin in medial domain ↓ in F_M/F_L
X: F_pMyoII,A/F_pMyoII,B
X: F_βPS
h AEL
Outliers
Median
R²: 0.07 ± 0.04
R²: 0.52 ± 0.27
R²: 0.54 ± 0.32
R²: 0.50 ± 0.14
R² (M):0.00
R² (L):0.20
R² (L):0.47
75±5 h AEL
95±5 h AEL
cell proliferation ↓
PH3

Figure 2.3: **The central domain of the wing disc pouch flattens and thickens as it grows.** (A i-v) Apical views of a wild-type wing imaginal disc at five different larval stages with medial (M) and lateral (L) domains defined. Fluorescence signals in green and magenta denote the patterning of Actin and Nuclei. (B i-v) Cross-sectional view of wing imaginal discs. (C) Plot showing quantification of (top panel) local basal curvature (κ_{basal}) and (bottom panel) cell height (H) along the DV axis of the pouch. Here l and L_{AP} denote the distance of the point from center of the pouch along the basal surface of AP axis and the length of the tissue along the AP axis, respectively. (D, D' i-v) Spatial patterning of pMyoII and βPS across the AP axis. (E) Quantification of the ratio of apical to basal intensities of pMyoII at multiple locations within the pouch's medial domain is plotted as a box plot for discs belonging to 72-96 h AEL. (E') Ratio of integrated intensity of βPS across the medial and lateral domains of the pouch. (F, F') Fluorescence intensity of Actin, pMyoII, and βPS. Several points sampled in the basal surface for discs belonging to 96h AEL larval stage. Average R^2 values for multiple samples are indicated. Different colors represent data from individual samples. (G, G') Plot showing a correlation between the ratio of apical to basal levels of pMyoII and tissue height belonging to 72 and 96 h AEL. R^2 values calculated over multiple samples have been reported (right bottom inset). The different colors in each plot represent different samples. (H, H') Fluorescence intensity of β-Integrin is plotted against the local basal curvature across several points sampled in the basal surface for discs belonging to 72 and 96 h AEL larval stage. Different colors represent the location of points within the pouch (medial/lateral). Region-specific R^2 values calculated using multiple samples are indicated (sample sizes, right bottom inset). (I i-ii) Apical view of pouch showing that the fraction of dividing cells marked by phosphohistone 3 (PH3) decreases as terminal organ size approaches.

(Figs. 2.3 E, 2.4 Fi-ii). Further, the increase in cell height between the lateral and medial domains becomes more pronounced as the disc grows in size (Appendix A Fig A.3 B, C). Collectively, these observations suggest that multiple independent mechanisms likely play integrative roles in orchestrating cell height and ensuring robust tissue morphogenesis.

Along with these cytoskeletal dynamics, cell proliferation decreases toward the end of larval development, in agreement with previous studies [29, 34, 35] (Fig 2.3 I, Appendix A Fig A.6). These observations of dynamic changes in cell-level processes such as contractility, cell-ECM adhesion, and proliferation suggest possible coordinated regulation between cell growth, proliferation, and the cell mechanics that define subcellular features of cells and the shape of the tissues.

2.4.3 Key Regulators of Basal Curvature Include the atio of Apical to Basal Contractility, ECM Stiffness and Cell-ECM Adhesion

We next tested several proposed mechanisms driving the flattening of the medial domain. From the normalized basal curvature (κ_{basal}) calculations, we confirmed that κ_{basal} is almost uniform at 72 h AEL larval stage but it becomes patterned with higher local κ_{basal} at the lateral ends at 96 h AEL (Fig 2.4 A-B"). To test hypothesized mechanisms that can generate medial flattening i.e. less curved than lateral ends (Fig 2.4 B"), we varied model parameters that correspond to perturbations in the cell cytoskeleton, the apical ($k_{api,cont}$) and basal ($k_{bas,cont}$) actomyosin contractility, the basal ECM stiffness ($k_{ecm,c}$), the membrane tension ($k_{memb,basal}$, $k_{memb,lateral}$, $L0_{memb,lateral}$, $L0_{memb,basal}$) and the Integrin-based adhesion between the cells and the basal ECM (k_{adhB}) (Appendix A Figs A.7, A.8). All simulations started with the same flat tissue shape as the initial condition. For comparison, our control simulation assumed homogeneous contractility across the AP axis on both apical and basal sides of individual cells with higher strength at the basal side while all other parameters remained constant. Under these conditions, the tissue evolved into a bent shape with a globally uniform curvature (Fig 2.4 C). For the in silico tests, parameters were

patterned differently as step functions to increase or decrease the parameter values in the medial and lateral domains of the pouch (Fig 2.4 D-i, details in Appendix A Figs A.7, A.8).

Next, we calculated the ratio of the average basal curvature of the lateral ends to the medial domain for both the experimental data and model simulations. This quantitative comparison (Fig 2.4 D-ii, Appendix A Fig A.9) revealed that the key regulators that can explain the flattening of the pouch's medial domain are the ratio of apical-to-basal contractility ($\frac{k_{api,cont}}{k_{bas,cont}}$), basal ECM stiffness ($k_{ecm,c}$) and the adhesion between pouch cells and the basal ECM (k_{adhB}) (Fig 2.4 i-iii, Supplementary Movies 1-3 of [1]). The prescribed parameter profiles for these cases (Fig 2.4 E i-iii, top panel) resulted in medial tissue flattening compared to the lateral ends.

To corroborate our model results, we employed a quantification pipeline for fixed and stained samples for pMyoII, Col-IV, and βPS (Fig 2.4 F–H). We observed that late-stage wing imaginal discs (96 h AEL) have a nonuniform spatial patterning of pMyoII along the AP axis across both the apical and basal surfaces. In particular, pMyoII is more localized at the apical-medial and basal-lateral domains (Fig 2.4 F). This variation generates a decreasing trend in the ratio of the apical to basal pMyoII as one moves away from the center of the pouch along the AP axis. A similar patterning of the parameters $k_{api,cont}$ and $k_{bas,cont}$ can generate the flattening in the medial domain as observed in the experimental data (Fig 2.4 E-i). In fact, a similar patterning of pMyoII across the basal surface is reported for later staged discs (Fig 2.4 F'-ii).

Next, our model demonstrates that a graded stiffness of ECM across the AP axis for ECM surrounding pouch cells generates a κ_{basal} profile similar to that of wing discs belonging to late developmental stages (96 h AEL). More specifically, a stiffer ECM at the pouch central region induced by increasing $k_{ecm,c}$ in this region promotes flattening (Fig 2.4 E ii). The underlying reason why this phenomenon is observed in Fig 2.4 E-ii can be attributed to the dynamics between the model columnar cells under contractile force and the ECM. While the contractile forces originating from actomyosin contractile springs situated in each columnar cell promote tissue curvature, the equilibrium angle, π, prescribed to the bending

potential energy function would lead to the ECM preferring a flat shape. By increasing the ECM stiffness (i.e. an increase in the resistance to stretching by increasing the linear spring coefficient) the ECM's contribution to the overall model tissue shape becomes more pronounced. Therefore, the angles between nodes in the model ECM will tend toward the equilibrium value reducing the basal curvature. Our result suggests that under certain conditions, the ECM's increased stiffness can promote a flatter basal curvature. Based on our observations, wing disc morphogenesis can be a joint effort of the locally stiffening ECM and the dynamics of actomyosin contractility. Apart from the graded ECM stiffness along the DV axis, the ECM appeared less taut at the basal region of squamous cells as compared to pouch columnar cells.

Our experimental results show increased Col-IV localization in the lateral bends of the wing disc (Fig 2.4 G, G'). This localization may result from two possible phenomena. First, it may result from spatially nonuniform local growth, which is greater in the z-direction (greater ECM thickness), increasing the local growth mismatch between the cell layer and the ECM in the planar AP direction. Alternatively, or additionally, this increased localization is due to greater basal contractility, shrinking the basal region resulting in a higher density of Col-IV compared to the flatter medial basal domain of the wing disc. Our data also shows higher Col-IV localization in the region surrounding the squamous epithelia, confirming the difference in stiffness of ECM surrounding the squamous and columnar cells. The latter finding is consistent with the results presented in previous work [24, 25]. This result is also consistent with fold generation inhibited in the vicinity of a stiff ECM. Future experiments are required to estimate the mechanical properties of ECM to validate predictions made by the computational model.

Lastly, our model simulations show that increasing the adhesion strength between the ECM and basal surface of columnar cells at the lateral domains compared to the medial domain flattens the tissue (Fig 2.4 E-iv). Similar to the input parameter profile, we observe high Integrin localization in the lateral domains of the pouch compared to the medial region for discs belonging to late developmental stages (Fig 2.4 H, H'-ii).

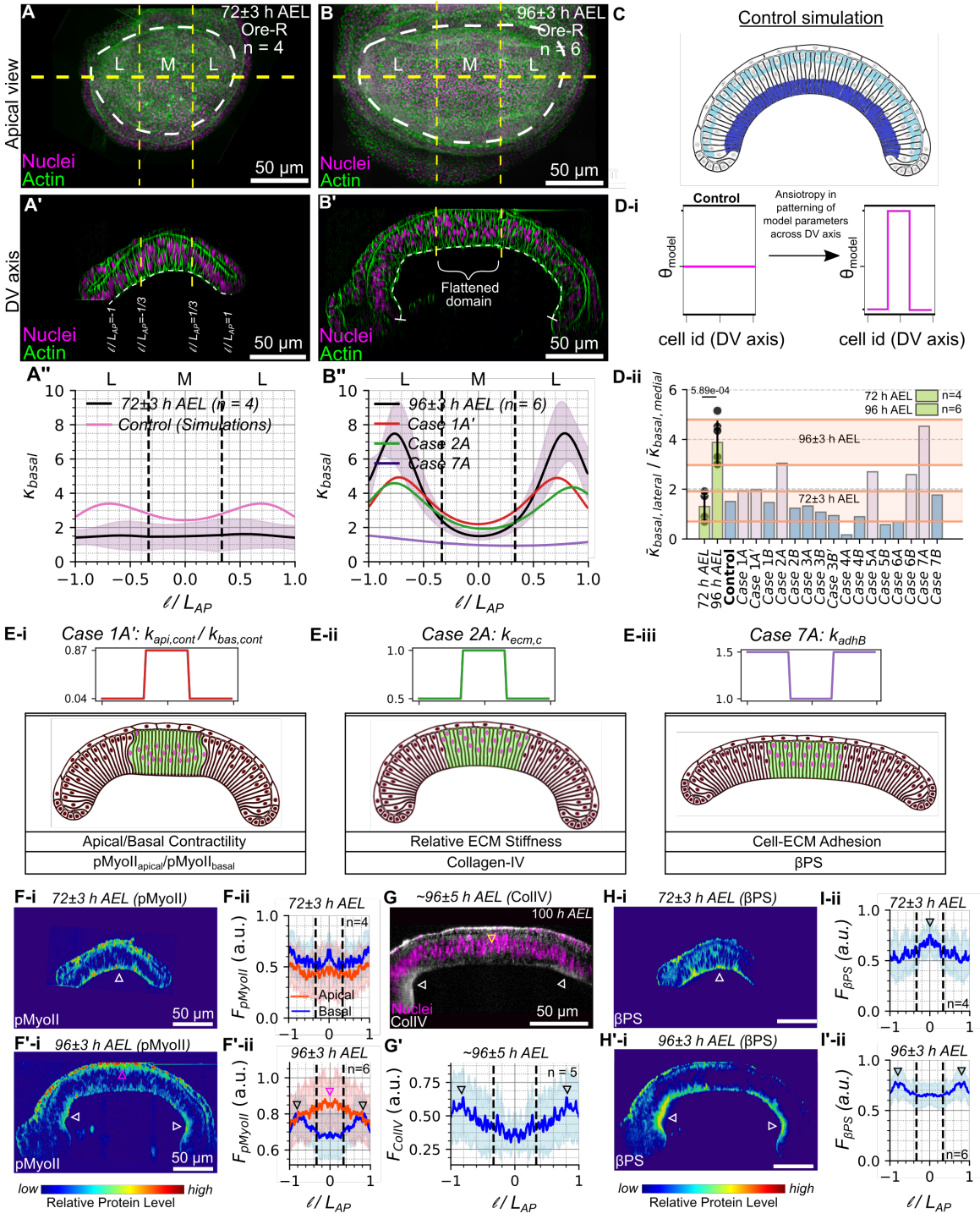
A
72±3 h AEL
Ore-R
n = 4
Apical view
L
M
L
Nuclei
Actin
50 µm
B
96±3 h AEL
Ore-R
n = 6
A'
DV axis
B'
Flattened domain
C
Control simulation
D-i
Control
Ansiotropy in patterning of model parameters across DV axis
θmodel
cell id (DV axis)
A''
B''
72±3 h AEL (n = 4)
Control (Simulations)
96±3 h AEL (n = 6)
Case 1A'
Case 2A
Case 7A
κbasal
ℓ / LAP
D-ii
5.89e-04
72 h AEL
96 h AEL
n=4
n=6
96±3 h AEL
72±3 h AEL
κ̄basal, lateral / κ̄basal, medial
Control
Case 1A
Case 1A'
Case 1B
Case 2A
Case 2B
Case 3A
Case 3B
Case 3B'
Case 4A
Case 4B
Case 5A
Case 5B
Case 6A
Case 6B
Case 7A
Case 7B
E-i
Case 1A': kapi,cont / kbas,cont
0.87
0.04
Apical/Basal Contractility
pMyoII apical/pMyoII basal
E-ii
Case 2A: kecm,c
1.0
0.5
Relative ECM Stiffness
Collagen-IV
E-iii
Case 7A: kadhB
1.5
1.0
Cell-ECM Adhesion
βPS
F-i
72±3 h AEL (pMyoII)
pMyoII
F-ii
72±3 h AEL
n=4
Apical
Basal
FpMyoII (a.u.)
F'-i
96±3 h AEL (pMyoII)
F'-ii
96±3 h AEL
n=6
G
~96±5 h AEL (ColIV)
100 h AEL
Nuclei
ColIV
G'
~96±5 h AEL
n = 5
FColIV (a.u.)
H-i
72±3 h AEL (βPS)
βPS
I-ii
FβPS (a.u.)
H'-i
96±3 h AEL (βPS)
low
high
Relative Protein Level

Figure 2.4: **The evaluation of computational model scenarios validates cytoskeletal impact on tissue curvature via biomechanics.** (A, B) Reference apical and (A'-B') cross-sectional views of a wild-type (WT) disc stained with DAPI and Phalloidin at (A) 72 h and (B) 96 h AEL. (A"-B") Ratio of average curvature over the lateral and medial domain for staged discs (72 and 96 h AEL) compared with simulation results. Plots show the normalized curvature of the tissue basal surface (κ_{basal}) calculated for samples corresponding to 72 h and 96 h, respectively. The red, green, and purple solid lines in (B") correspond to the normalized basal curvature from simulation cases Ei-iii. (C) Control simulation output. (D-i) Perturbing model parameters (θ_{model}) that correspond to the cell cytoskeleton and cell-ECM adhesive energies. θ_{model} was patterned as a step function. (D-ii) Quantification of the ratio of average curvature in the lateral-to-medial pouch domains for staged discs (72 and 96 h AEL) and simulation results. Green bars denote the experimental data. Blue and pink bars represent the simulation data. The pink bars denote cases that capture medial flattening. Shaded regions represent the mean plus or minus one standard deviation. (E i-iii) Simulation results from varying model parameters representing mechanical properties of cell cytoskeleton. Parameter profiles are plotted. The green-colored region represents the medial domain of the simulated tissue. Case 1 A' in B", D-ii and E-i is Case 1D from Appendix A Fig A.8. See Appendix A Fig A.9. (F-F' i) Heat maps of pMyoII distribution across the DV section for 72 and 96 h AEL discs. Color code represents lower (blue) to higher (red) intensity of pMyoII. (F-F' ii) Variation of pMyoII localization across the pouch apical and basal surfaces. Plots show intensity profiles across the AP axis. (G) Col-IV antibody staining in AP cross-section of 90-100 h AEL disc. (G') Spatial localization of Col-IV in the pouch basal surface. (H-H' i) Heat maps of βPS distribution across the DV section of 72 and 96 h AEL discs. (I-I' ii) Variation of βPS localization across the pouch basal surface. Plots show intensity profiles across the AP axis.

In summary, our experimental data, together with the simulation results, suggest that nonhomogeneous actomyosin contractility, basal ECM stiffness, and cell-ECM adhesion all can generate a tissue shape with non-uniform curvature where the medial section is flat. These correlations in non-homogeneous spatial patterns suggest the possibility of mechanistic redundancy and crosstalk between multiple cellular processes. A high degree of correlation between βPS and pMyoII at the pouch basal surface across multiple developmental stages (Fig 2.3 F) suggests that spatiotemporal regulation in one of the cytoskeletal regulators affects the patterning of another.

2.4.4 A Balance in the Patterning of Forces Generated by Actomyosin Contractility, Basal Cell Tension, and Cytoplasmic Pressure Maintains a Spatial Profile in Cell Height

As described previously, the average tissue height increases as the discs age from 72 h to 96 h of larval development (Fig 2.3) across both medial and lateral domains of the pouch (Fig 2.5 A, A'). Our experimental data, which is validated by previous studies [11], also shows a gradient in the patterning of cell height across the AP axis (Fig 2.3, Appendix A Fig A.3). Cells in the central region of the pouch are more elongated as compared to cells in the lateral ends (Fig 2.5 A, A', Appendix A Fig A.3 D).

To test the importance of cytoskeletal regulation in defining the tissue height, we analyzed cell height for the simulation outputs generated during the different model scenarios (Appendix A Figs A.7, A.8). Our model identifies apical and basal contractility ($k_{api,cont}$ and $k_{bas,cont}$, respectively) and basal cell tension ($k_{memb,basal}$, $L0_{memb,basal}$) as crucial regulators of cell height in the middle domain of the tissue (Fig 2.5 A, A'). These parameters were patterned across the AP axis as previously described. An increase in the $\frac{k_{api,cont}}{k_{bas,cont}}$ ratio within the pouch medial domain causes the cells to elongate (Fig 2.5 A, Appendix A Fig A.10). Moreover, our model also suggests that an increase in the contractility values in both the apical and basal surfaces of the pouch while (1) keeping the ratio constant and (2) increasing the ratio led to an increase in average tissue thickness (Appendix A Fig A.10). This increase

in cell height is limited to the medial pouch domain where the increase in the apical and basal contractility is introduced. (Additional details regarding the variation in the ratio can be found in the Appendix A section A.3.7 "Tissue Local Height is Regulated by the Difference in Apical-Basal Contractility"). Finally, our model suggests that modulating the basal tension of the cells changes tissue thickness. In particular, lowering basal tension in the center of the pouch by increasing $L0_{memb,basal}$ shrinks the height in the medial domain (Fig 2.5 A, Case 6B).

Next, we analyzed experimental perturbations to test the role of the aforementioned contractility and basal tension parameters on basal curvature and height maintenance. First, we perturbed tension in the basal surface of columnar cells by RNAi-mediated downregulation of *myospheroid* (*mys*), a β-subunit of the Integrin dimer (Fig 2.5 B). Perturbation in the cell-ECM adhesion through downregulation of *mys* reduced basal βPS levels and cell height. Notably, the cell height reduction was pronounced across the lateral section of the pouch (Fig 2.5 D, D') as denoted by the p-values of the student t-test for the comparison of height (H) between RyR^{RNAi} control and mys^{RNAi} (p-value of 0.06 and <0.05 in the lateral and medial sections, respectively). Interestingly, the loss of Integrins also caused a loss in basal expression of pMyoII, suggesting a positive regulation of pMyoII through Integrin localization (Appendix A Fig A.11 E, E'). Next, we varied the apical to basal contractility ratio, associated with the $\frac{k_{api,cont}}{k_{bas,cont}}$ ratio from simulations, in the dorsal compartment of the pouch by expressing $\text{Rho1}^{\text{RNAi}}$ using an MS-1096 Gal4 driver (Fig 2.5 C, C'). Inhibiting Rho1 increases cell height and inhibits basal curvature (Fig 2.5 D, D', Appendix A Fig A.11).

Although the computational model scenarios identified the parameters that can explain the control of cell height within the medial domain of the tissue, it remained unclear if they were sufficient to generate the gradient in cell height across the AP axis as observed in the experimental data (Fig 2.5 A, A'). Except for the variation of $\frac{k_{api,cont}}{k_{bas,cont}}$, the other case study simulations did not generate the same difference in average cell heights compared to the experimental data. Since the loss of actomyosin contractility in Rho1 genetic perturbations

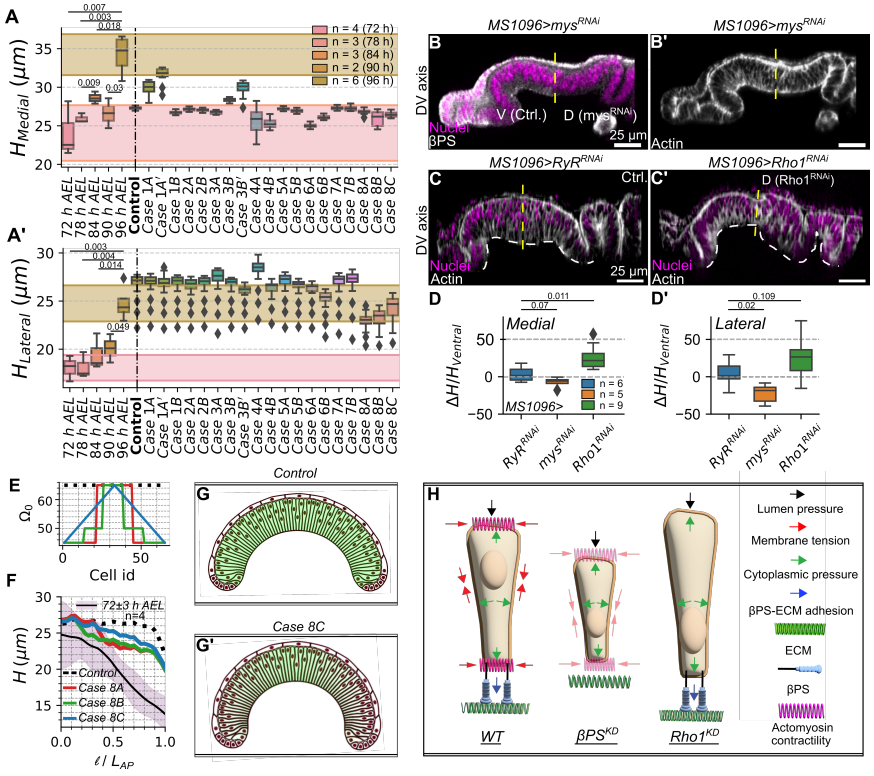

Figure 2.5: **A balance in actomyosin-mediated contractility, surface tension, Integrin-ECM adhesion, and cell pressure patterns tissue thickness.** (A, A') Quantification of medial and lateral heights for discs belonging to 72-96 h AEL larval stages and model simulations (Reference parameter profiles are found in Appendix A Fig A.7). The error bars represent points within the 1.5 interquartile range of the lower and upper quartile, and diamonds represent the values outside this range, respectively. Shaded regions represent the standard deviation of the 72 h and 96 h experimental data. (B-B') β-Integrin was knocked down in the dorsal compartment of the wing (*MS1096-Gal4* x *UAS-mys^{RNAi}*). Visualization of the cross-section along the DV axis. (C-C') pMyoII was knocked down in the dorsal compartment of the wing disc (*MS1096-Gal4* x *UAS-Rho1^{RNAi}*). Control for the experiment has been generated by crossing the same Gal4 driver with a *UAS-RyR^{RNAi}* line, previously validated as a negative control for wing morphology. (D, D') Quantification of medial and lateral heights for the β-Integrin and pMyoII genetic perturbations. (E) The target cell volume (Ω_0) in the Lagrange Multiplier was varied across the DV axis for pouch cells. Variations of parameter profiles are included. (F) Plot showing the height of discs at 96 h AEL. The black solid line indicates the average experimental height. The shaded region represents the standard deviation across multiple samples. Lines in green and blue represent the control and the case where the Ω_0 was patterned. (G, G') Model simulation output for (F). (H) A schematic summary of height regulation in pouch cells. Here, WT and KD stand for wild-type and knockdown, respectively.

increased cell height, we hypothesize that cytoplasmic pressure within the cell must be one of the factors causing the tissue to increase in volume with reduced cortical actomyosin tension. Moreover, the increase in cell height was non-uniform and increased more in the medial than the lateral region (Fig 2.5 D, D'). This suggests that a non-uniform distribution of cell pressure across the AP axis may potentially explain the varying degrees of cellular height changes across the AP axis when Rho1 is inhibited. Testing this hypothesized spatial gradient in cell pressure across the tissue requires future experiments. In our simulations, we varied cell pressure by changing the control volumes (Ω_0) of cells such that Ω_0 decreases away from the center of the pouch (Fig 2.5 E-G', Appendix A Fig A.12). A patterning of Ω_0 increased the gradient in cell height, as is observed within the experimental data (Fig 2.5 F, G', Supplementary Movie 4 of [1]). Hence, the cell height in the lateral domains is more sensitive to variations in cell volume, while the cell height in the medial domain of the tissue is more sensitive to non-homogenous patterning of actomyosin contractility. In conclusion, our computational model simulations show that changing the relative ratio between apical and basal actomyosin contractility by modifying $k_{api,cont}$ and $k_{bas,cont}$, varying the tension in the basal membrane by changing $k_{memb,basal}$ or patterning cell pressure [36] through the target volume term (Ω_0) can impact local tissue height (Fig 2.5 H).

2.4.5 The Relative Levels of Apical Contractility and Basal Surface Tension Determine Nuclear Positioning in Pseudostratified Epithelial Cells

Next, we analyzed the positioning of nuclei within pouch cells of wing imaginal discs from 72 h and 96 h AEL (Fig 2.6 A-A'). In the initial stages, the distribution of nuclear positioning is uniform across the AP cross-section (Fig 2.6 A, B). However, with age, nonmitotic nuclei in the medial domain are more basally located than those in their lateral counterparts (Fig 2.6 A', B). To study the relative importance of individual cytoskeletal regulation components, we measured nuclei positioning across the pouch medial and lateral domains for all of the different simulation case scenarios performed in the previous sections (Figs 2.3, 2.4). We

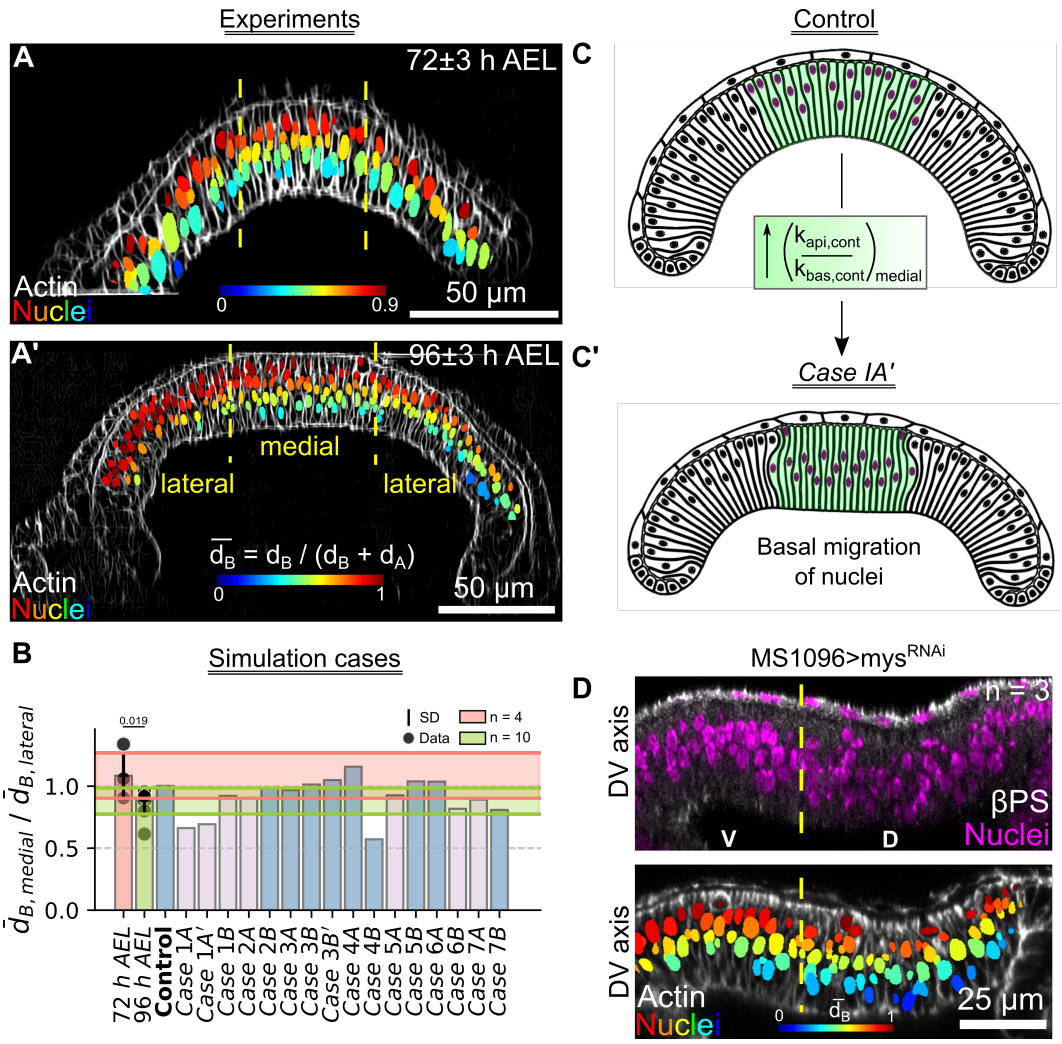

Figure 2.6: **Higher levels of apicocentral contractility results in a basal bias of the position of nuclei.** (A-A') Optical sections along the AP axis for discs belonging to 72 and 96 h AEL were used to mimic the patterning of contractility in the model simulations. Nuclei have been color-coded with respect to their distance from the basal surface ($\bar{d}_B$). (B) Bar graph visualizing ratio of $\bar{d}_B$ between the medial and lateral pouch domains for the experimental data (orange and green bars) and the model simulations (pink and blue bars). (C) Nuclear positioning in a uniformly patterned actomyosin profile is distributed uniformly within each columnar cell. (C') A non-uniform actomyosin patterning generates a flatter midsection, resulting in a shift of nuclear positions toward the basal side in the midsection. (D) (Top panel) Optical section along the DV axis for pouch expressing mys^{RNAi} predominantly in the dorsal compartment using an *MS1096-Gal4* driver. Fluorescent labels have been indicated as an inset within the plot. (Bottom panel) Nuclei within the genetically perturbed cross-section have been color-coded based on $\bar{d}_B$, where 0 and 1 denote a more basal or apical location, respectively.

define $\bar{d}_B$ as the relative distance of the nuclei from the basal surface (Fig 2.6 A'). The ratio of $\bar{d}_B$ across the medial to lateral domains was computed and compared with the experimental data (Fig 2.6 B).

In the case of a uniform patterning of the actomyosin profile, the relative nuclear positioning along the apicobasal axis shows marginal differences across the whole wing disc (Fig 2.6 B, C). A higher ratio of apical to basal contractility ($\frac{k_{api,cont}}{k_{bas,cont}}$) in the medial domain (Case 1A'), where the apical contractility is comparable to the basal contractility, pushed the nuclei to the basal surface of the pouch (Fig 2.6 B, C, C'). The simulated shift in contractility is similar to the experimentally reported change of pMyoII (Fig 2.3). Based on our experimental observations and predictions generated by our model, we initially targeted the inhibition of actomyosin contractility in the dorsal compartment of the wing disc by inhibiting Rho1. This inhibition resulted in the migration of columnar cell nuclei towards the basal surface, as detailed in Appendix A Fig A.13. Thus, Rho1 mediates actomyosin contractility in maintaining the proper nuclear arrangement within wing discs.

Further, our model simulation results suggest a patterning of basal tension (Case 6B) and the adhesion of cells with the ECM (Case 7A) (Fig 2.4 D-i, Appendix A Fig A.7), which can also impact nuclear positioning (Fig 2.6 B). To validate this experimentally, we knocked down *myospheroid* (*mys*) predominantly in the dorsal compartment of the wing disc. As a result, we observed more migration of nuclei to the basal surface of cells in the dorsal compartment compared to the ventral side, semi-quantitatively validating the model predictions (Fig 2.6 D').

Both our experimental data and computational simulations suggest that nuclei are shifted basally in the center of the wing disc as development progresses. In summary, our results in this section indicate that the apical-basal polarization of myosin and the patterning of basal tension and cell-ECM adhesion influence nuclear positioning within the epithelium.

2.4.6 Increasing Cell Proliferation Enhances Local Basal Curvature

To study how cell proliferation impacts tissue geometry along the AP axis, we incorporated the proliferation of the columnar cells in our computational model (Fig 2.7). For these simulation scenarios, the initial geometry of the wing disc specified in simulations reflects the curvature observed in experimental wing discs at approximately 72 h AEL. We varied cell proliferation rates by increasing or decreasing the cell cycle length (C.C.L.) in the posterior compartment of the wing imaginal disc (Fig 2.7 Ai-iii, Supplementary Movies 5-7 in [1]). Note that an increase in C.C.L. induces a decrease in proliferation, while a decrease in C.C.L. increases proliferation. In particular, we set the posterior-to-anterior cell cycle length ratio of 400% for Fig 2.7 A-i or 50% for Fig 2.7 A-iii, which was compared to the "wild type" control simulation that exhibits a spatially homogeneous cell division rate (Fig 2.7 A-ii). A decrease in proliferation reduced basal curvature and cell height (Fig 2.7 A-i, B-i, Appendix A Fig A.16 A, B). In contrast, increasing cell proliferation in the posterior compartment increased the local basal curvature (Fig 2.7 B-iii). In other words, an increase in proliferation rate results in increased inwards bending of the pouch (Fig 2.7 B-iii, Supplementary Movie 7 in [1]). Finally, cell height slightly increases in a compartment-specific manner if cell proliferation is increased (Appendix A Fig A.16A, B).

2.4.7 Targeting Proliferation via Different Signaling Pathways Results in Distinctive Tissue Morphologies

To qualitatively validate the model simulation's predictions, we investigated the impact of genetically perturbing the growth signaling pathways in a compartment-specific fashion on the morphology of the wing disc pouch. First, we inhibited proliferation in the posterior compartment by expressing the dominant-negative (DN) form of the *Drosophila* insulin receptor (InsR^{DN}) in the posterior compartment (Fig 2.8 A). We confirmed that downregulation of insulin signaling activity through the expression of InsR^{DN} reduced the number of mitotic cells [37] (Appendix A Fig A.14). Strikingly, inhibiting insulin signaling in the posterior compartment reduced tissue bending (Fig 2.8 B, C-i). Additionally, we observed

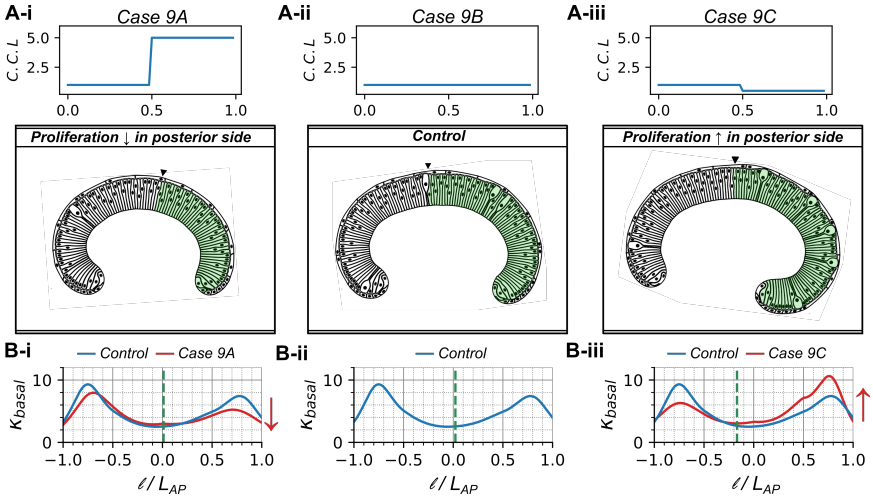

Figure 2.7: **Stimulating cell proliferation increases tissue curvature.** Comparison of the local basal curvature between simulated wing disc cross sections with compartment-specific variation of proliferation rates. These simulations assumed increased actomyosin contractility on the basal region of the columnar cells. (A i-iii) Cell cycle duration in the posterior compartment is varied compared to the constant anterior compartment. (B i-iii) Plots quantifying and comparing the distribution of local basal curvature corresponding to cases (A i-iii). Red arrows denote a decrease or increase in curvature.

that the tissue height decreased (Fig 2.8 C-ii). We also expressed constitutively active forms of insulin receptors ($InsR^{CA}$) in the whole pouch. We found that such discs showed a significant increase in the inwards bending (Fig 2.8 G, G', H-i) and tissue height (Fig 2.8 H-ii).

Insulin signaling can also regulate contractility via a PI3K-mediated activation of pMyoII [38, 39]. Consequently, we assessed if there were changes in the spatial patterning of cytoskeletal regulators such as Integrin or Rho1, an upstream activator of pMyoII. We found that the relative Integrin levels measured across multiple samples did not change significantly (Fig 2.8 F-i). However, there is a statistically significant decrease in Rho1 (Fig 2.8 D, D', F-ii). We also report a compartment-specific reduction in pMyoII levels upon expression of $InsR^{DN}$, suggesting that insulin signaling interacts with Rho GTPases to regulate contractility within the tissue (Fig 2.8 F-iii). As a loss in contractility can also

result in a loss of bending, it is difficult to decouple the individual role of proliferation in generating bending across the tissue.

To further test how growth regulators impact tissue geometry, we studied the effect of downregulating *mTOR*, a direct regulator of the cell cycle and cellular growth in the wing disc [40] (Appendix A Fig A.15). First, we expressed the dominant negative form of *mTOR* in the posterior compartment with engrailed-*Gal4*. However, the progeny was lethal. Hence, we expressed $mTOR^{DN}$ in the dorsal compartment of the wing disc with *apterous-Gal4*. The expression of $mTOR^{DN}$ resulted in the loss of bending in a compartment-specific manner compared to the control Gal4 driver (Appendix A Fig A.15 B-ii, E-ii). We also report a decrease in cell height upon expression of $mTOR^{DN}$ (Appendix A Fig A.15 E-i). Finally, while we did not observe changes in βPS (Appendix A Fig A.15 D-i), we report a compartment-specific decrease in both basal Rho and basal pMyoII along the AP axis upon expression of $ap{>}mTOR^{DN}$ in the dorsal compartment (Appendix A Fig A.15 D-ii).

Similar to the findings from our computational model, our experimental data captures the trends predicted by our model, that an overall increase or decrease in cell proliferation can result in an increase and decrease of both cell height and basal curvature, respectively. Additionally, quantitative analysis of the experimental data shows that changing proliferation through InsR or *mTOR* can also cause changes in cytoskeletal regulators such as pMyoII. Cytoskeletal regulation and cell proliferation are correlated, which makes it impossible to decouple the relative importance of the two through experiments. As a result, we ran additional simulations where we decreased both cell proliferation and basal contractility in half of the pouch (Appendix A Fig A.16 C, D). The simulations qualitatively recapitulate the tissue flattening observed within the InsR and *mTOR* genetically perturbed samples. Moreover, our simulations show that decreased basal contractility further decreases the tissue's ability to fold. However, by genetically downregulating mTOR in an 84 hr AEL wing discs, we observed that the tissue geometry for loss of mTOR seems similar to the control during the early stages of development, suggesting that there are no noticeable initial alterations in tissue morphology (Appendix A Fig A.17). Based on this evidence, it

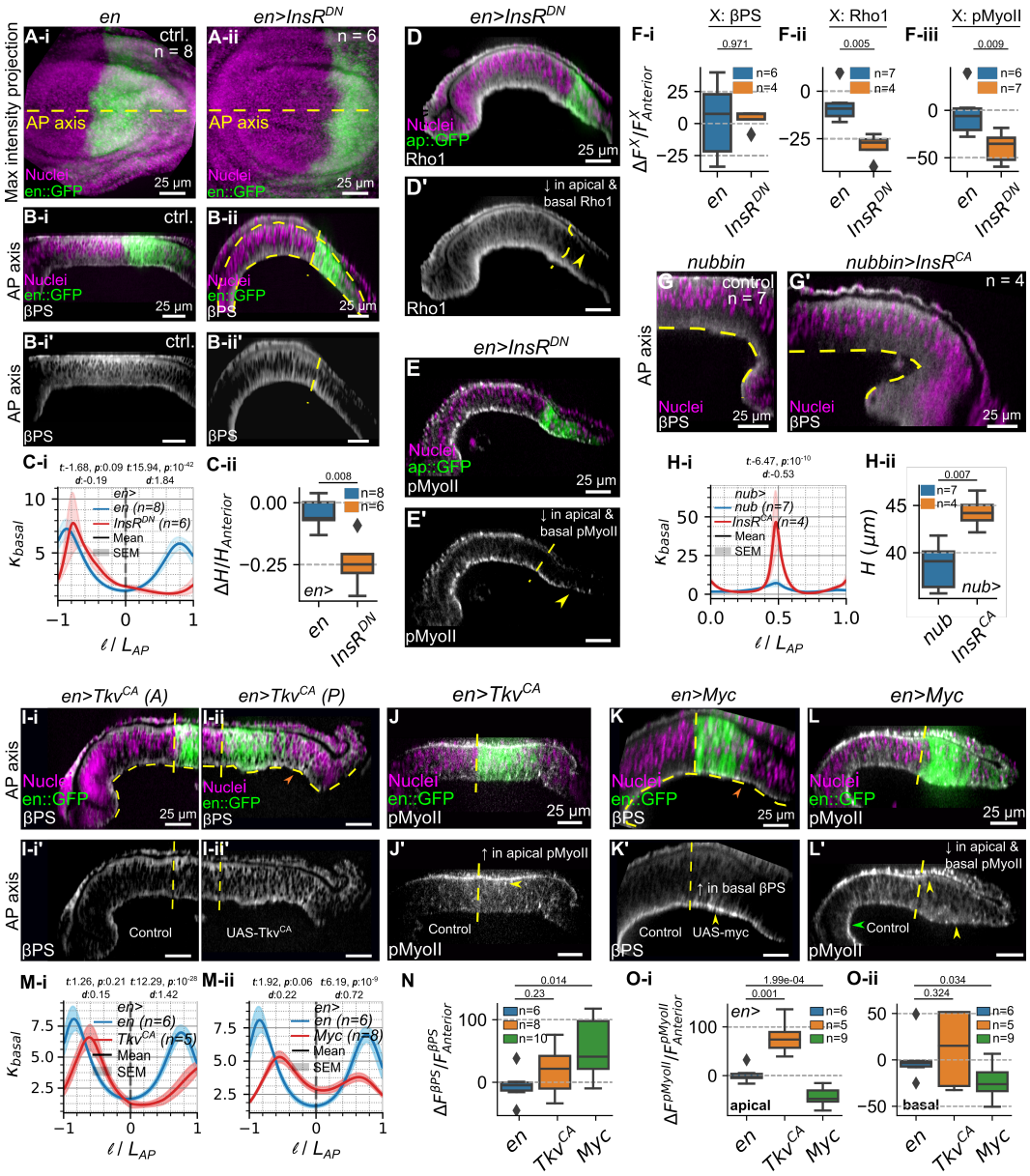
en
en>InsR^DN
en>InsR^DN
X: βPS
X: Rho1
X: pMyoII
Max intensity projection
A-i
ctrl.
n = 8
A-ii
n = 6
AP axis
Nuclei
en::GFP
25 μm
D
Nuclei
ap::GFP
Rho1
D'
↓ in apical & basal Rho1
F-i
0.971
F-ii
0.005
F-iii
0.009
n=6
n=4
n=7
ΔF^X/F^X_Anterior
B-i
B-ii
βPS
B-i'
B-ii'
E
pMyoII
E'
↓ in apical & basal pMyoII
nubbin
nubbin>InsR^CA
G
control
n = 7
G'
n = 4
C-i
t:-1.68, p:0.09 t:15.94, p:10^-42
d:-0.19
d:1.84
en>
en (n=8)
InsR^DN (n=6)
Mean
SEM
κ_basal
ℓ / L_AP
C-ii
0.008
n=8
n=6
ΔH/H_Anterior
H-i
t:-6.47, p:10^-10
d:-0.53
nub>
nub (n=7)
InsR^CA (n=4)
H-ii
0.007
n=7
n=4
H (μm)
nub>
nub
InsR^CA
en>Tkv^CA (A)
en>Tkv^CA (P)
en>Tkv^CA
en>Myc
en>Myc
I-i
I-ii
J
K
L
I-i'
I-ii'
J'
↑ in apical pMyoII
K'
↑ in basal βPS
L'
↓ in apical & basal pMyoII
Control
UAS-Tkv^CA
UAS-myc
M-i
t:1.26, p:0.21 t:12.29, p:10^-28
d:0.15
d:1.42
Tkv^CA (n=5)
M-ii
t:1.92, p:0.06 t:6.19, p:10^-9
d:0.22
d:0.72
Myc (n=8)
N
0.014
0.23
n=6
n=8
n=10
ΔF^βPS/F^βPS_Anterior
O-i
1.99e-04
0.001
n=6
n=5
n=9
apical
ΔF^pMyoII/F^pMyoII_Anterior
O-ii
0.034
0.324
basal
en
Tkv^CA
Myc

Figure 2.8: **Stimulating cell proliferation by different growth-promoting pathways results in two distinct phenotypes.** (A) Maximum intensity projection of (i-i') control and (ii-ii') samples expressing dominant negative insulin receptor InsR^{DN} in the posterior compartment driven by en-Gal4. Proliferating cells are marked by PH3. (B) Cross-section along AP-axis for (i-i') control and (ii-ii') InsR^{DN}. (C) Plots quantifying the (i) basal curvature profile and (ii) difference in average cell heights between the perturbed posterior and control anterior compartment (ΔH). ΔH is normalized by the average height of the control anterior compartment. (D, E) (D-D') Rho1 and (E-E') pMyoII expression across the AP axis for pouches expressing InsR^{DN} in the posterior compartment. (F) Quantification of the differences in average fluorescence intensities (ΔF^X) of (i) X: βPS, (ii) X: Rho1 and (iii) X: pMyoII between the posterior and anterior compartment for *en>Ins*^{DN} in the wing disc posterior compartment. ΔF^X is further normalized by average fluorescence intensity of X in the control anterior compartment. (G-G') Cross section along AP axis (medial to lateral, half the pouch) for discs expressing nubbin Gal4 driver and nubbin>InsR^{CA}. (H) Quantification of (i) basal curvature and cell height (ii) for disc expressing *InsR*^{CA}. (I-J') Optical section along the dorsal-ventral compartment boundary taken in the anterior (left) and posterior (right) compartments of the wing disc. (I-I') expressing a constitutively active form of Tkv receptor (*Tkv*^{CA}) and (J-J') AP cross sections of wing discs expressing *en> Tkv*^{CA} stained with pMyoII. Fluorescent labels have been indicated within the figure. (K-K') overexpressing *Myc* in the posterior compartment. Scale bars correspond to 25 μm unless indicated. (L-L') AP cross sections of wing discs expressing *en>Myc* stained with pMyoII. Fluorescent labels have been indicated within the figures. (Mi-ii) Quantification of local basal curvature (κ_{basal}) for discs overexpressing *Tkv*^{CA} and *Myc*. (N) Boxplot visualizing differences in average βPS ($\Delta\beta$PS) expression between posterior (perturbation) and anterior (control) compartments on *en> Tkv*^{CA} or *en>Myc*. $\Delta\beta$PS was normalized by average fluorescence intensity computed within the anterior compartment. (O) Similar quantification for pMyoII was carried out at the pouch apical and basal surfaces for *en> Tkv*^{CA} and *en>Myc*.

appears that our simplifying assumptions for different developmental stages are suitable for the present study.

To further test the effect of increasing cell proliferation on tissue morphology, we perturbed other growth signaling pathways. We next overexpressed the constitutively active form of DPP receptors, Tkv^{CA}, in the posterior compartment [41] (Fig 2.8 I-I'). Finally, we also overexpressed Myc in the posterior compartment (Fig 2.8 K-K'), since it is a known regulator of cellular growth in developing *Drosophila* wing imaginal discs [42]. Since both constitutive active Dpp signaling and Myc stimulate the overgrowth phenotype in the pouch [30, 43], an increase in local basal curvature upon expression of Tkv^{CA} and Myc was expected. Surprisingly and in contrast to perturbations in insulin signaling, both the Tkv^{CA} and Myc overexpression conditions decreased inward bending in the posterior compartment (Fig 2.8 Mi-ii).

Based on these counter-intuitive results, we reasoned that both Tkv^{CA} and Myc may also impact the relative concentration levels of cytoskeletal regulators. Hence, we next explored how perturbing cell proliferation through the expression of Tkv^{CA} and Myc affects cytoskeletal regulation. In particular, we examined changes in cell-ECM adhesion (βPS) and actomyosin contractility (Rho1, pMyoII) (Fig 2.8 I-L, Appendix A Figs A.18, A.19). We found no statistically significant change in the expression of βPS upon expression of Tkv^{CA} in the posterior compartment when compared to the internal control, which is the anterior compartment (Fig 2.8 I, N). However, an increase in both Rho1 and pMyoII was observed in the posterior compartment when Tkv^{CA} was expressed therein (Fig 2.8 J, J', Appendix A Fig A.18). More specifically, there is a statistically significant increase in pMyoII in the apical surface of the posterior compartment where Tkv^{CA} was expressed (Fig 2.8 Oi-ii). Conversely, overexpression of Myc in the posterior compartment resulted in a statistically significant increase in βPS levels (Fig 2.8 K-K', N). Nevertheless, we documented a decrease in Rho1 and pMyoII at the pouch lateral domain upon Myc overexpression (Fig 2.8 L, L', Oi-ii, Appendix A Fig A.19). Additionally, as a check for our Rho1 antibody staining studies, we also tested Rho1 biosensors and observed similar expressions proving that the Rho1 antibody

staining likely provide a reasonable proxy for activity (Appendix A Fig A.22). However, in the future, additional studies will be needed to understand how growth regulators control Rho1 dynamics and activity. In the subsequent section, we computationally validate whether the changes as mentioned earlier are capable of rescuing the increased epithelial bending associated with enhanced cell proliferation.

2.4.8 A Dual Regulation of Proliferation and Mechanical Regulators Causes a Loss in Tissue Bending

To resolve the apparent contradiction of the prediction that increases in cell proliferation enhance basal curvature, we ran additional simulations where we changed both cell proliferation and cell mechanics. More specifically, we divided the in silico tissue into anterior and posterior compartments and computationally increased proliferation in one half of the pouch by 50% (posterior side) and then systematically varied the parameters controlling cytoskeletal regulators in the region of perturbation (Fig 2.9 A, B). Based on a comparison of the ratio of average basal curvature of the posterior to the anterior compartment (Fig 2.9 A), we identified that an increase in basal cell-ECM adhesion (k_{adhB}, 50% increase in the posterior compartment), ECM stiffness ($k_{ecm,c}$, 100% increase in the posterior compartment) or apical actomyosin contractility ($k_{api,cont}$, 300% increase in the posterior compartment) (Fig 2.9 Bii-iv) could effectively counter the increase in bending upon increased proliferation (Fig 2.9 B-i) (see Supplementary Movies 7-10 in [1]). Similar to the Tkv and Myc perturbation data, our simulations capture the trend of loss in tissue bending in the compartment of perturbation.

Through a comparison between experimental data on cytoskeletal regulation in $en{>}Tkv^{CA}$ genetic perturbations (Fig 2.8 I-J') and the best simulation cases identified (Fig 2.9 A), we conclude that an increase in apical to basal ratio of pMyoII (Fig 2.8 O) serves as one of the essential driving forces for flattening of the pouch basal surface despite of an increase in proliferation. An increase in apical pMyoII can be attributed to an increase in Rho, as observed in $ap{>}Tkv^{CA}$ genetic perturbations and supported by previous studies [11].

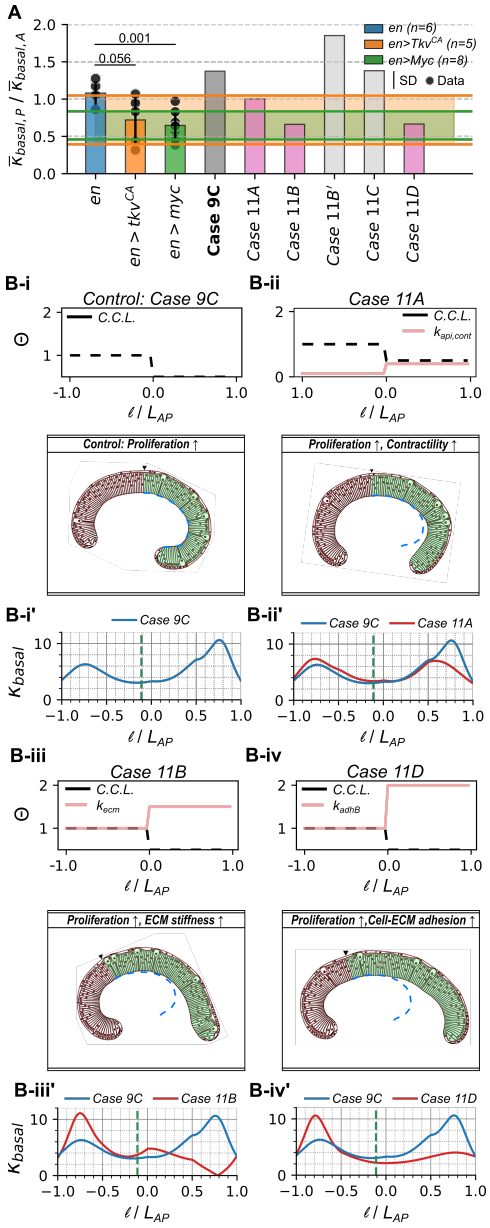

Figure 2.9: **Effects of increased proliferation can be buffered by concomitant changes in cytoskeletal regulation.** (A) Comparison of ratio of average basal curvature in the posterior to anterior compartment in Fig 2.8 (I-K) and for (B i-iv). (B i-iv) The simulated cases closely replicate shape changes in the form of κ_{basal} reduction as observed in Tkv^{CA} and *Myc* genetic perturbations. Two perturbations were performed in these simulations. First, cell proliferation was increased in the posterior (P) compartment of the model wing disc compared to the anterior (A) compartment. Second, parameters controlling cytoskeletal regulators were varied in the region of increased proliferation. (B i'-iv') Quantification of the basal curvature for each case corresponding to (B i-iv).

Further, downregulation of *Tkv* in the posterior compartment reduced both Rho1 levels and basal curvature (Appendix A Fig A.18). This supports a mechanism where Dpp regulates pMyoII through Rho GTPases to control contractility [11]. In addition, Rho1-mediated phosphorylation of pMyoII can increase contraction along the apical and basal surfaces of the pouch, and this further promotes the local increase in cell height. Hence, the analysis of the experimental data also suggests an increase in cell height upon expression of Tkv^{CA} in the wing imaginal disc [11] (Appendix A Fig A.18 G). This agrees with simulations that show an increase in columnar cell height upon an increase in the apical to basal contractility ratio (Fig 2.5 A-A").

An analysis of experimental data on cytoskeletal regulation in *en>Myc* genetic perturbation reveals that an increase in βPS mediated cell-ECM adhesion (Fig 2.8 K, N) and a decrease in pMyoII mediated basal contractility (Fig 2.8 L, O) can result in pouch flattening despite the concurrent increase in proliferation. Currently, there is limited experimental data on how Myc regulates cytoskeletal dynamics during development. To investigate the pMyoII mechanism, we carried out a Rho antibody staining, revealing a similar decrease in Rho levels as observed for pMyoII upon Myc overexpression (Appendix A Fig A.19). Additionally, previous studies have also found that c-Myc suppresses the activity of RhoA affecting Actin dynamics in cancer cells [44]. Previous literature findings also demonstrate a strong correlation between ITGA1 (Integrin subunit alpha 1) and c-Myc expression in colorectal cancer cells [45]. This suggests that the changes in βPS observed in *en>Myc* genetic perturbations may be generalized to multiple biological contexts.

Our model also predicts that an increase in ECM stiffness by increasing $k_{ecm,c}$ can reduce the folding of tissue along the AP axis (Fig 2.9 B-iii). One of the scenarios where the stiffness of the tissue can increase is when the rate of ECM production is less than the growth rate in the cellular layer. The effect of Tkv and Myc mutations on ECM stiffness remains a point for future inquiry.

In summary, our experimental data, along with computational simulations, reveal that a balance in cell proliferation and differential patterning of cytoskeletal regulators determines

the overall shape of the wing imaginal disc. A temporal change in both facilitates shape changes during morphogenesis, and different growth-promoting pathways lead to divergent changes in cytoskeletal regulation. This flexibility leads to the ability to tune both overall organ shape and size.

2.5 Discussion

One of the most important unresolved problems in developmental biology is how tissue morphogenesis is coordinated through the regulation of both cell proliferation and the cellular cytoskeleton. The relative contributions of cell proliferation and cell mechanics to the final morphology of an organ are context-dependent. In some situations, proliferation and morphogenesis are separated into nonoverlapping temporal stages. For example, cell proliferation halts before gastrulation begins in the fly [46]. This strategy is likely important when developmental speed is of the essence, and the tissue cannot reach a pseudo-steady state before a new developmental event occurs. In other contexts, proliferation and cell shape changes occur simultaneously, as in the developing vertebrate optic cup [47].

In this chapter, a multi-scale (in space) SCE computational model, closely integrated with experiments, was used to quantitatively investigate the emergent features of tissue morphogenesis. The biologically calibrated SCE model describing both tissue growth and morphogenesis incorporates the spatial patterning of fundamental subcellular properties (Fig 2.2). Additionally, the model implements for the first time the dynamics of interkinetic nuclear migration within the simulated pseudostratified epithelium. This includes the basal to apical motion of the nucleus, mitotic rounding, and cell division dynamics (Fig 2.2). Key characteristics of global tissue architecture, such as the local curvature of the basal wing disc epithelium, cell height, and nuclear positioning, serve as metrics for model calibration. Our experiments show how these physical features are jointly regulated through spatiotemporal dynamics in the localization of pMyoII, β-Integrin, and ECM stiffness (Fig 2.3). As the disc

grows in size, there are progressive changes in the patterning of key subcellular features such as actomyosin contractility (Fig 2.3).

Here, we show that the patterning of actomyosin contractility, ECM stiffness and cell-ECM adhesion along the AP axis near the DV compartment boundary are vital regulators of tissue shape changes, specifically driving the flattening of the midsection (Fig 2.4) and increasing the cell height (Fig 2.5). Moreover, changes in cell shape across the AP axis pattern the positioning of nuclei (Fig 2.6). The predictions made by the model simulations agree with the observed changes in contractility and cell-ECM adhesion during wing disc morphogenesis. In fact, they are validated through perturbations of either actomyosin contractility ($\text{Rho1}^{\text{RNAi}}$) or basal cell tension and cell-ECM adhesion (mys^{RNAi}).

Through multiple case studies, our computational model identifies the primary regulators of cell height to be the apical to basal ratio of actomyosin contractility, basal membrane tension, and cell volume (Fig 2.5). In particular, we show that variation in pressure (modeled as target volume) is sufficient to generate a gradient of cell height across the pouch AP axis [36]. To further validate the model's predictions, we demonstrate that dysregulation in either actomyosin contractility or cell-ECM adhesion through *Rho* and *mys* perturbations cause severe morphological defects (Fig 2.5 B-E).

Our experimental studies also show that changes in proliferation using multiple different pathways also substantially regulate the cytoskeleton. Using the computational model simulations, we show that a decrease or increase in proliferation alone can decrease or increase the tissue basal curvature and height, respectively. We experimentally validated these findings by perturbing *InsR* and *mTOR* signaling in specific compartments. Downregulation of either pathway caused a reduction in basal curvature and tissue height (Fig 2.8 C). However, perturbing cell proliferation via other cell signaling pathways of growth also cause changes in cytoskeletal regulation. For example, inhibition of *InsR* signaling causes a reduction in pMyoII through a *Rho* signaling pathway (Fig 2.8 D, E).

Notably, we show that increasing proliferation through distinct mechanisms results in two very different wing disc phenotypes (Fig 2.10). While increasing proliferation through

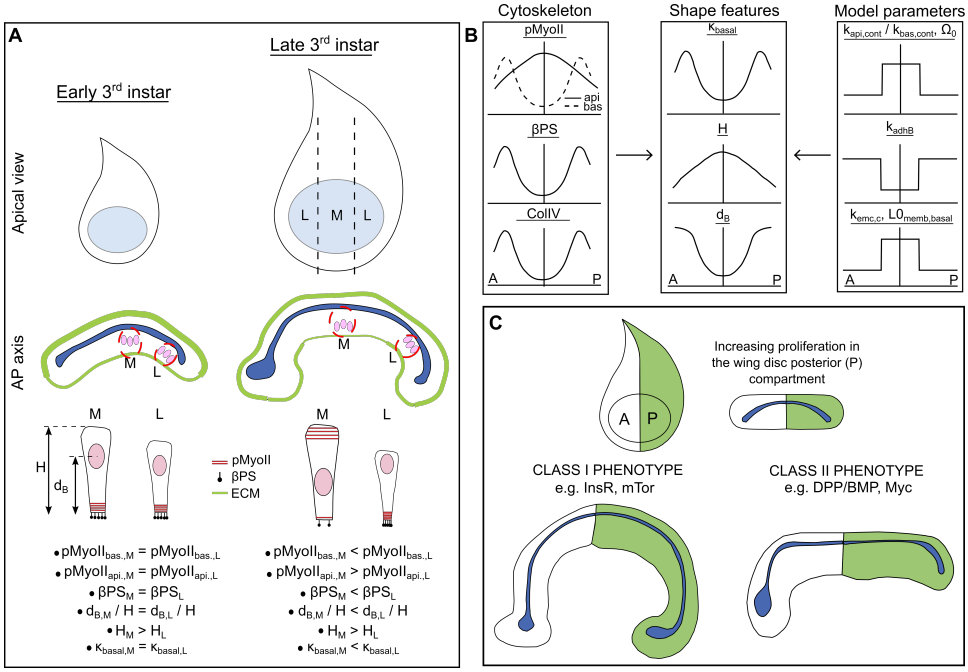

Figure 2.10: **Summary of mechanistic insights into how perturbations to various growth signaling pathways impact tissue shape.** (A) As the wing disc grows, the central, medial (M) domain of the pouch flattens and thickens while cells in the lateral (L) region increase their curvature. The cytoskeletal dynamics and morphological parameters are consistently adjusted with the age of the tissue. (B) Patterning of model parameters that produce shape features consistent with patterning of cytoskeletal components. (C) Increasing the proliferation rate through genetic perturbation in a compartment-specific manner resulted in distinct classes of morphological phenotypes.

the expression of $InsR^{CA}$ causes an increase in basal curvature of the tissue, expressions of Tkv^{CA} and *Myc* flatten the tissue even with increased proliferation. Model simulations show that upregulation of either apical contractility or basal cell-ECM adhesion in the genetic perturbations can drive tissue flattening despite increasing proliferation. Thus, our study shows that a combination of spatial patterning of cytoskeletal regulators and proliferation shapes the organ locally during development to prepare the wing imaginal disc for later pre-pupal and pupal stages of development [48].

Our experimental data and model simulations also highlight the existence and role of spatial heterogeneity in ECM stiffness (Fig 2.4). The experimentally observed flattening of the pouch medial domain can be explained by patterning the local stiffness of ECM

associated with the columnar pouch cells along the AP axis. This result extends our previous findings, where we showed that a difference of stiffness between the two ECM layers, either adhering to the peripodial squamous cells or columnar disc pouch cells, maintains the bent shape of wing imaginal disc [24]. Recently, Harmansa et al. [25] further showed that a difference in the growth rate of the pouch cells and their corresponding ECM leads to the variation of stiffness of ECM across pouch cells and squamous cells [25]. However, in that model, the stiffness ECM associated with the pouch is assumed to be homogeneous throughout the entire tissue and does not explore the spatial patterning of ECM stiffness in the planar direction or near the lateral bends. Collectively, these studies suggest that future investigations are needed to understand the spatial patterning of ECM stiffness across all anatomical axes and to perform biophysical measurements.

Future developments of our multi-scale computational model will include a more detailed, microscale stochastic description of the interaction between the actin filaments and myosin motors such that the directionality of the contractile forces can be explicitly incorporated and the mitotic rounding process along with cell division be extended to include a complete representation of mechanistic details. Developing fully chemical-mechanical models based on the approach from Ramezani et al. will also enable a fully integrated perspective of organ size control [49]. The experimentally calibrated computational framework opens avenues for exploring feedback loops between tissue shape and cell proliferation. Moreover, it will facilitate exploring further the independent modulation of various parameters controlling the cell mechanical properties.

Our findings reflect similar mechanisms of morphogenesis in other developmental contexts. For example, the dynamic and autonomous morphogenetic process of formation of the optic cup, i.e., retinal primordium, is reminiscent of the tissue flattening that occurs before subsequent eversion of the wing imaginal disc [47]. During the formation of the mammalian optic cup, the invagination happens in four stages. Flattening of the distal region of the initially hemispherical vesicle is observed in the first two stages. The angle at the hinge then begins to become narrower, following which, in phase four, the neural retina epithelium

starts to expand as an apically convex structure, forming a cup via progressive invagination. This morphogenetic process, specifically the last two phases, resembles the tissue bending and flattening in the wing disc. Balancing mutually antagonistic morphogenetic processes is also seen in mammalian development, including the developing mouse lens [50]. Overall, the principal findings identified in our work can be generalized and incorporated into our understanding of development across multiple organ systems in animals due to the underlying biochemical and biomechanical similarities that drive morphogenesis [16, 51].

2.6 Code and Data Availability

2.6.1 Code Availability

An open-source C++ and CUDA implementation of the computational model presented in this chapter is available in Zenodo (https://zenodo.org/badge/latestdoi/468540858) [82] or on GitHub (https://github.com/jenniferrangel/Episcale_CrossSectionalView.git).

2.6.2 Data Availability

Representative experimental data and any files to analyze the experimental data are provided under the section Source data of [1]. The 3D confocal microscopy data are available upon request from the corresponding authors of [1]: Jeremiah J. Zartman and Mark Alber.

Chapter 3

Mathematical Model of Actomyosin Network Dynamics Towards Integration With the Wing Disc SCE Model

3.1 Preface

The mathematical and computational models presented in this chapter were developed by me with the help of Dr. Mark Alber. Any experimental data used in this chapter was either provided by Dr. Jeremiah Zartman's lab, our collaborators from the University of Notre Dame, or obtained from literature. Whenever data is used, either source will be clearly stated.

3.2 Introduction

3.2.1 Biological Role and Importance of Actomyosin Contractility

The actomyosin network, comprising actin filaments and phosphorylated non-muscle myosin II (pMyoII), is a highly conserved subcellular contractile machinery in muscle and non-muscle cells. The mechanical forces generated by this network are commonly known as actomyosin contractility, a mechanism that plays an important role in cell shape changes and deformations, cell growth and tissue morphogenesis [13, 48, 125–127]. In addition, actomyosin contractility plays an important role in other biological processes such as cell division, endocytosis, cell migration, gastrulation, ventral furrow formation, embryo development, remodeling of the extracellular matrix (ECM), and wound healing to name a few [81, 126, 128–136]. Moreover, as reviewed in [137], during development, the subcellular contractile forces propagating through the tissue lead to drastic tissue shape changes such as elongation, bending, and budding. Although the actomyosin contractile network in these different biological processes may differ in structure, components, location, and purpose, the network consists of the essential building blocks: actin filaments and pMyoII [128].

In our biological system of study, the *Drosophila* wing imaginal disc, actomyosin contractility is a key regulator of cell- and tissue-level processes during organ development that facilitate the proper final size and shape of the wing. For example, a combined experimental and modeling study of the early stages of wing disc development demonstrates that the actomyosin contractile forces in the basal region of the columnar cells generate the bent "dome" shape of the wing disc pouch along the anterior-posterior (AP) axis [24]. This characteristic shape must be achieved to guarantee the success of subsequent stages of development and avoid misshapen wings [24]. In Chapter 2, we demonstrate that actomyosin contractility is also a key regulator of local tissue curvature, cell height and nuclear positioning of the wing disc epithelium [1]. Additionally, as described in the previous chapter, actomyosin contractility drives interkinetic nuclear migration (IKNM) during cell division of the *Drosophila* wing disc [13]. However, the exact mechanism of how actomyosin generates and coordinates

the contractile forces to facilitate IKNM is poorly understood [138]. Hence, in this chapter, we develop an actomyosin network model and its computational implementation with the goal of coupling this subcellular network model with the SCE model presented in Chapter 2 in order to understand how actomyosin contractility drives IKNM in the wing disc. To do so, we must first gain a more profound understanding of the actomyosin components, how the actin-pMyoII interactions give rise to contractility, and what is known about actomyosin contractility during interkinetic nuclear migration.

3.2.2 Actomyosin Network Components, Structure and Contractility

Actin filaments and non-muscle myosin II mini-filaments are the core components of the actomyosin network (Fig 3.1). The actin filaments are semi-flexible polymers that resist tension but can undergo compressive forces, i.e., the filaments cannot be stretched but can be bent [125, 139]. An actin filament is formed via the polymerization of globular actin (G-actin) monomers [140]. This process gives rise to a double-stranded helical polymer with $\sim 7 - 9nm$ diameter and a well-defined polarity [141] (see Fig 3.1 A). In other words, the two ends of the actin filament are different: one is denoted the barbed or plus end, while the other is the pointed or minus end. Although polymerization and depolymerization can occur on both ends, polymerization occurs at a faster rate on the barbed (+) end, while depolymerization is preferred on the pointed (-) end [142] (Fig 3.1 A). Thus, the barbed and pointed ends are commonly classified as the fast-growing and slow-growing ends, respectively. During actin-pMyoII binding dynamics, the actin filament polarity is extremely important as it guides the pMyoII to move along the actin filament in a single direction.

Non-muscle myosin II (MyoII), the second component of the network, is a molecular motor that binds to and translocates actin filaments via ATP hydrolysis. The structure of MyoII is composed of three different domains: (1) a head domain with two heads that are responsible for binding to the actin filaments and ATP hydrolysis, (2) a neck domain consisting of two essential (ELCs) and two regulatory (RLCs) light chains responsible for the activation of MyoII, and (3) a tail domain [126, 143] (see Fig 3.1 B, top panel). In

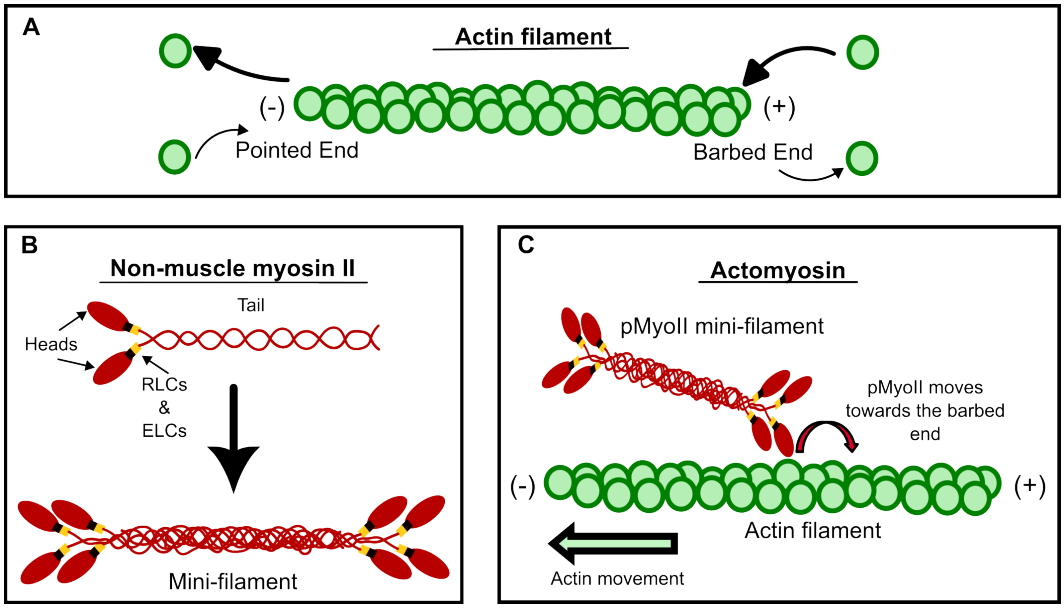

Figure 3.1: **Schematics of the biological components of the actomyosin network.** (A) Representative schematic of an actin filament showing the barbed (+) and pointed (-) ends of the filament. The arrows represent the polymerization (arrows pointing inwards) and depolymerization (arrows pointing outwards) of actin monomers. Big bold and small thin arrows represent faster and slower polymerization or depolymerization rates, respectively. This helps denote the barbed end as the fast-growing end while the minus end is the slow-growing end [142]. (B) Representation of a phosphorylated non-muscle myosin II (pMyoII) molecule (top) that ensembles via the tail domain with several other pMyoIIs to form a mini-filament (bottom) with multiple motor heads on both ends. A single pMyoII has two heads, two regulatory light chains (RLCs), two essential light chains (ELCs), and a tail domain [126, 143]. (C) Illustration of actin-pMyoII dynamics. A pMyoII mini-filament will move on an actin filament in a directed manner (always towards the barbed end). As it moves, it will exert a pulling force that will translocate the filament in the opposite direction of the pMyoII movement (green arrow). Note that illustrations (A)-(C) were drawn in accordance to the biological descriptions found in reviews [81, 125, 126, 128, 145, 150].

an inactive state, MyoII remains in a "folded" state where it cannot interact with other MyoII molecules or actin filaments. Upon phosphorylation of the RLCs via Rho-associated kinase (ROCK), myosin light chain kinase (MLCK) or Cdc42-binding kinase (MRCK), MyoII becomes phosphorylated non-muscle myosin II (pMyoII), unfolds, and enters its "active" state [126, 144–149]. Once activated, pMyoII molecules can ensemble together via their tail domain and form bipolar mini-filaments [126] with several heads on both ends of the pMyoII mini-filament (see Fig 3.1 B, bottom panel). Once a pMyoII mini-filament has been formed, its motor heads bind to actin filaments.

Actomyosin contractility is the end product of the pulling forces the non-muscle myosin II mini-filaments exert on anti-parallel actin filaments (filaments of opposite polarity), causing filaments to translocate past one another [128, 150]. More specifically, once bound to actin, pMyoII mini-filaments interact with actin via an ATP-powered mechanochemical cross-bridge cycle [151]. The bound pMyoII motor heads will always "walk" towards the barbed end of the actin filament and as they move, pMyoII will exert a pulling force that slides the actin filament [81, 125] (see Fig 3.1 C). These molecular-level interactions give rise to the mechanical forces we know as actomyosin contractility. In theory, depending on the arrangement of the actin filament polarity and where the pMyoII mini-filament is positioned between the two filaments, their interactions can give rise to contractile or extensile forces [81, 125]. However, studies of reconstituted actomyosin networks show that the networks are predominantly contractile [128, 152, 153]. In a later section of this chapter, we will use our proposed mathematical model to run simulations with different arrangements of actin filament polarity and explore whether the different setups give rise to contractile or extensile forces.

Several studies have shown that contractility is affected by the actin filament network organization [81, 125, 154, 155]. In other words, some structures are more prone to produce higher contractility than others. For example, in muscle cells, the actomyosin complex has an organized sarcomere structure with anti-parallel actin filaments (filaments with pointed ends in the center and barbed ends outwards) and myosin mini-filaments between the actin

filaments, which optimize contractile forces [125, 156]. However, in the case of non-muscle cells, the actomyosin network can have less organized and more versatile structures. Some of these structures include but are not limited to, rings, bundles, stress fibers, asters, cables, and meshworks [128]. During morphogenesis, it appears that pulsatile networks and supracellular cables are common actomyosin structures. As reviewed in [145], pulsatile actomyosin networks and supracellular cables are necessary for *Drosophila* gastrulation and dorsal closure as well as during wound healing. In addition, pulsatile networks alone constrict the apical cell surface during *Drosophila* ventral furrow formation and *Xenopus* mesoderm invagination (see Figure 1 of [145]).

In addition to network architecture, there are other factors that can impact the contractility of the network. Some of these factors include actin filament depolymerization, bending, and cross-linking [81]. Cross-linkers, which are actin-binding proteins that link actin filaments together, have been shown to either enhance or limit contractility. In other words, in some networks, a small amount of cross-linkers is necessary to facilitate contractility, but when too many cross-linkers are part of the network, contractility will be hindered [128, 157–159]. Aside from cross-linkers, actin filaments can also bind to E-cadherin and integrin proteins, which mediate cell-cell and cell-ECM adhesions, respectively [126]. These adhesions allow the actomyosin contractile forces to be transmitted to its external environment and propagate throughout the tissue. In addition, these adhesion sites can actively affect contractility, as is the case during *Drosophila* egg chamber elongation [160].

For more details and extensive reviews on actomyosin dynamics and contractility, please see the following references [81, 125, 126, 128, 145, 150].

3.2.3 Importance of Actomyosin During Interkinetic Nuclear Migration (IKNM)

As mentioned in the previous chapter, the columnar cells (also known as pouch cells) of the *Drosophila* wing disc are pseudostratified epithelial cells (Fig 3.2 A), meaning that these cells are tightly packed, thin and elongated [1, 19]. During division, these cells undergo

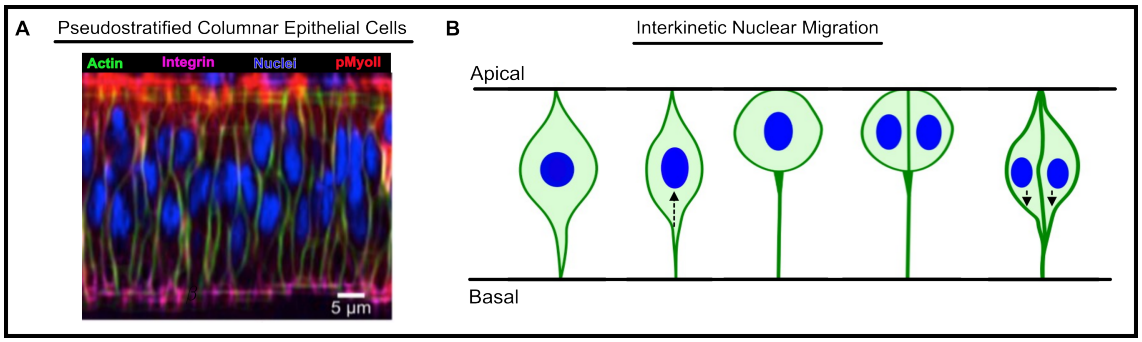

Figure 3.2: **Pseudostratified epithelial cells and their interkinetic nuclear migration process (IKNM) during cell division.** (A) An experimental image of columnar cells in the *Drosophila* wing disc, which are classified as pseudostratified epithelial cells. Fluorescence signals in green, magenta, blue and red denote Actin, Integrin, Nuclei and pMyoII respectively. Image courtesy of Dr. Zartman's lab. (B) Representative diagram of the IKNM process, capturing the apical migration of the nuclei, mitotic rounding and the production of two new daughter cells at the end of cell division. This illustration was prepared with the help of Dr. Zartman's lab.

IKNM (Fig 3.2B), a process that consists of the migration of the nuclei to the apical region of columnar cells in order to divide [13, 19, 138]. Once the nucleus is in the apical region, the cell undergoes mitotic rounding and proceeds with the remaining stages of the division cycle [12, 32].

A previous study conducted by Meyer et al. demonstrates that actomyosin contractility drives IKNM [13]. More specifically, in this study, the actin and pMyoII dynamics are disrupted with latrunculin A (LatA) and Rho kinase inhibitor Y-27632 treatments, respectively, and as a result, the nuclei became more basally located [13]. This suggests that hindering actomyosin contractility disrupts IKNM. Furthermore, during the process of IKNM and mitotic rounding, a basal constriction is observed in [13], forming a predominantly actin enriched tail. This observation is consistent with our experimental data presented in Chapter 2 (see Fig 2.2) [1]. Finally, IKNM appears to be driven by actomyosin contractility in other biological systems, such as the retinal epithelia of zebrafish [161].

Although previous studies have shown that actomyosin contractility is a key regulator of IKNM, the exact mechanism of how actomyosin generates the forces that facilitate IKNM

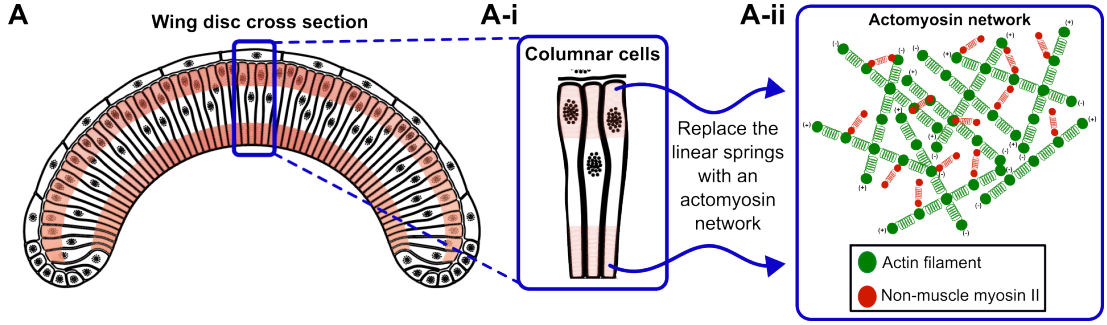

Figure 3.3: **Illustration of the end goal.** (A) Simulated wing disc cross-section produced from the SCE model presented in Chapter 2 [1, 24]. The light red-colored regions in the apical and basal parts of the tissue represent the actomyosin contractile springs in the model. (A-i) Zoomed-in view of simulated columnar cells. (A-ii) Replace the simplified representation of actomyosin in the columnar cells with an actomyosin network composed of actin filaments (green) and non-muscle myosin II mini-filaments (red).

remains an open question [138]. A study by Badugu et al. proposes that the actomyosin contraction in the basal region of the cells causes cytoplasmic flows, which in turn drives IKNM [162]. In addition, Kirkland et al. confirmed the importance of actin and pMyoII dynamics and tissue architecture during IKNM [12]. Hence, there is a need to take a closer look and investigate how actomyosin constricts the basal membrane, leading to IKNM, and maintains the basal constriction for the remainder of the division process.

3.2.4 Synopsis

In this chapter, we propose a detailed actomyosin network model intended to extend the simplified representation of actomyosin from Chapter 2. This will allow us to capture a complete representation of the mechanistic details during cell proliferation of the *Drosophila* columnar cells and also get a deeper understanding of how actomyosin contractility drives IKNM. In the previous chapter, actomyosin is represented as several apical and basal linear springs connecting the lateral sides of each columnar cell [1] (see Fig 3.3 A, A-i). Here, we propose to extend this simplified representation of actomyosin with a detailed model of subcellular-level actomyosin network dynamics that has a separate representation of the network components: actin filaments and non-muscle myosin II (Fig 3.3 A-i, A-ii).

This two-dimensional network model provides a detailed description of the actin-myosin interactions that explicitly capture the contractile forces. Moreover, once coupled with the multi-scale SCE model from Chapter 2, it will enable us to explore the possible mechanism(s) of how these contractile forces lead to the basal narrowing of cells that drive the (1) apical migration of nuclei during IKNM and (2) mitotic rounding, processes required for successful cell division.

3.3 Methods

3.3.1 Mathematical and Computational Modeling Background

Several mathematical and computational modeling approaches have been developed to model the actomyosin network according to the specific question of study. These models vary from continuum models to agent-based models to chemical-mechanical models. For example, continuum models have been used to study the contraction of actomyosin rings, disordered actomyosin networks, and actomyosin bundles [175–177]. In a study by Mirza et al., a continuum model is presented where the actin cytoskeleton is described as an active gel and used to investigate how the actin cytoskeleton organizes into bundles [178]. Although these continuum models are capable of providing critical insights into the contractile behavior of different actomyosin network structures, the continuum modeling approach does not capture the molecular-level properties of the actomyosin network components and the interactions between actin filaments and pMyoII mini-filaments. On the other hand, agent-based models are capable of explicitly modeling actin filaments and pMyoII at the molecular level and have been used to investigate the role of pMyoII in reorganizing and contracting the actin network [179, 180]. Finally, chemical-mechanical (mechanochemical) models have also been developed to study how chemical signals and mechanical forces regulate actomyosin contractility. MEDYAN is one of the most well-known mechanochemical models, which was developed by Popov et al. [181]. In addition to investigating the effect of mini-filaments and cross-linkers

on the contractile behavior of the actomyosin network, the MEDYAN model has been used to investigate actomyosin network reorganization and formation of actin rings [182, 183].

Other coarse-grained modeling approaches have been developed to represent the actomyosin network where actin filaments are represented as beads or point-like elements connected via linear springs [165, 166, 184]. In other cases, actin filaments are represented by cylindrical segments, whereas pMyoII mini-filaments tend to be represented as either cylindrical segments or Hookean springs [171, 185].

In this chapter, we represent the actomyosin network using a bead and spring modeling approach, a method that is commonly used to study actomyosin networks and other systems of polymers [163–168]. This approach allows us to represent the mechanical and physical properties of model components in detail, where model parameters can be calibrated directly using experimental data. For more details about the model and its novel components, please see the following sections 3.3.2 - 3.3.4.

3.3.2 Model Description

In this chapter, we assume that the actomyosin network is composed of actin filaments and phosphorylated non-muscle myosin II (pMyoII) mini-filaments (Fig 3.4 A). In particular, a node and spring modeling approach is utilized to describe both of the network components [1, 163–166] (Fig 3.4 B, C), where overdamped Langevin equations describe the actin and pMyoII dynamics. Specifically, a previously developed model [165] is extended and modified for our biological application of interest. Different from [165], we represent pMyoII mini-filaments as a pair of nodes connected via a linear spring to resemble the known biological structure of the mini-filaments and to be able study the potential impact of varying the number of actin filaments each mini-filament node can bind to on the overall contractile behavior of the network. Moreover, we introduce a stochastic force term on the pMyoII nodes to account for the thermal and random forces acting on the pMyoII mini-filaments. For a detailed description of the actin filament and pMyoII mini-filament submodels, please see sections 3.3.3 and 3.3.4 below.

Note that once the actomyosin network model is incorporated into the mechanical model of wing disc development presented in Chapter 2, additional novel components will be introduced. First, we will need to consider boundary conditions since the actomyosin network will be embedded inside the columnar cells. Second, additional force terms will be added to the Langevin equations of the actin nodes to account for external forces. These additional terms include the adhesion forces between the cell membrane and the actomyosin network and, potentially, interactions between the network and the cell nucleus.

3.3.3 Actin Filament Sub-Model

Each actin filament in the actomyosin network is represented as a set of equidistant nodes connected by linear springs (Fig 3.4 B). Consecutive filament segments have a bending force term modeled as a linear bending spring (Fig 3.4 B, zoomed section). Note that we define a filament segment as node-spring-node. Furthermore, we assume that the mass of the individual actin filament is lumped together at its nodes, similar to [163]. Since the actin nodes are equally spaced, this assumption allows for a uniform distribution of mass of the actin filament. To account for the intrinsic polarity of an actin filament, the first and last nodes of a simulated filament will be the barbed (fast-growing/polymerizing) or pointed (fast depolymerizing) end [81]. For example, if the first node in a filament is labeled with a "(+)" to represent the barbed end, then the last node is labeled with a "(-)" to represent the pointed end (Fig 3.4 B). Finally, each node in the actin filament will serve as a possible binding site for the non-muscle myosin II mini-filaments. Although actin filaments are known to polymerize and depolymerize, we will not account for these processes in this model. However, this modeling approach accounts for actin filament stretching and bending and actin-myosin interactions.

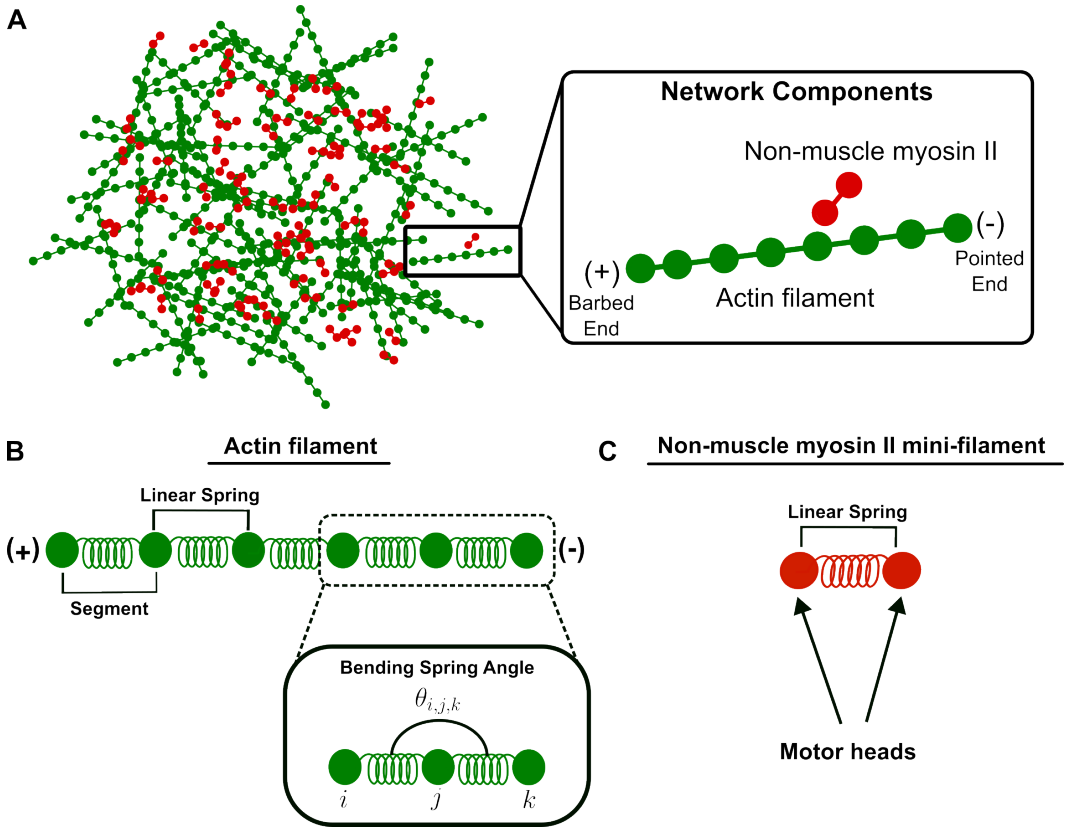

Figure 3.4: **Diagram of the actomyosin network components.** (A) Simulated two-dimensional actomyosin network. The zoomed section shows the detailed description of the individual network components. Actin filaments are shown in green with their barbed end denoted with a (+) and their pointed end denoted with a (-). The non-muscle myosin II (pMyoII) mini-filaments are shown in green. (B) A single actin filament is modeled as a set of nodes connected by linear springs. The first and last nodes denote the filament polarity where as before the (+) and (-) denote the barbed and pointed ends, respectively. A filament segment consists of two consecutive nodes connected by a linear spring. The zoomed section illustrates a bending spring between nodes i, j and j with a bending angle denoted by $\theta_{i,j,k}$. (C) Representation of a single non-muscle myosin II mini-filament. Each mini-filament is modeled as a pair of nodes connected by a linear spring. The nodes represent the motor heads as these interact with and exert a pulling force on the actin filament nodes.

The actin nodes in a filament are free to move in a 2D space and are attached by linear springs with bending springs between neighboring segments (Fig 3.4 B). Moreover, the actin nodes are subject to stochastic and pMyoII-associated forces. The position $\boldsymbol{x}_{a,i}$ of the i^{th} actin filament node of interest is determined via the following Langevin equation of motion:

$$m_{a,i}\ddot{\boldsymbol{x}}_{a,i} \;=\; -C_a\dot{\boldsymbol{x}}_{a,i} \;+\; F_{a,i}^{spr} \;+\; F_{a,i}^{bend} \;+\; F_{a,i}^{actomyo-conn} \;+\; F_{a,i}^{myo-pull} \;+\; F_{a,i}^{stoch} \quad (3.1)$$

where $i \;\in\; \{1, ..., N\}$, N is the total number of actin nodes in a filament, C_a represents the drag coefficient, $F_{a,i}^{spr}$ is the spring force, $F_{a,i}^{bend}$ is the bending force and $F_{a,i}^{stoch}$ is the stochastic force satisfying the Fluctuation-Dissipation Theorem [78]. The forces due to the actin-myosin interactions are defined by $F_{a,i}^{actomyo-conn}$ and $F_{a,i}^{myo-pull}$, which represent the actomyosin connection forces (pMyoII binding to actin) and the pMyoII pulling force on actin, respectively.

Due to the relatively small mass of the actin filaments in the network and the viscous environment with a low Reynolds' number that surrounds them, we assume that the actin node dynamics are in an overdamped regime as in [1, 24, 32, 163, 164]. Hence, we neglect the inertial term, $m_{a,i}\ddot{\boldsymbol{x}}_{a,i}$, in Equation 3.1. Moving the damping term to the left-hand side, results in the following equation:

$$C_a\dot{\boldsymbol{x}}_{a,i} \;=\; F_{a,i}^{spr} \;+\; F_{a,i}^{bend} \;+\; F_{a,i}^{actomyo-conn} \;+\; F_{a,i}^{myo-pull} \;+\; F_{a,i}^{stoch}. \quad (3.2)$$

Next, we solve Equation 3.2 above using a Forward Euler scheme. This results in the following equation:

$$\boldsymbol{x}_{a,i}^{n+1} \;=\; \boldsymbol{x}_{a,i}^{n} \;+\; \frac{dt}{C_a}\left(F_{a,i}^{spr,n} + F_{a,i}^{bend,n} + F_{a,i}^{actomyo-conn,n} + F_{a,i}^{myo-pull,n} + F_{a,i}^{stoch,n}\right). \quad (3.3)$$

Here the supercripts n and $n+1$ represent subsequent time points and dt represents the time step.

The forces $F_{a,i}^{spr,n}$, $F_{a,i}^{bend,n}$ and $F_{a,i}^{actomyo-conn,n}$ on the right-hand side of Equation 3.3 are calculated using the negative gradient of energy, $F_{a,i} = -\nabla E_{a,i}$, where $E_{a,i}$ is a representative energy term associated with each actin filament node. More specifically,

$$\begin{aligned} F_{a,i}^{spr,n} &= -\nabla E_{a,i}^{spr,n} \\ F_{a,i}^{bend,n} &= -\nabla E_{a,i}^{bend,n} \\ F_{a,i}^{actomyo-conn,n} &= -\nabla E_{a,i}^{actomyo-conn,n}. \end{aligned}$$

The linear spring energy potential of the i^{th} actin node can be explicitly written as follows [1, 165, 166, 169]:

$$E_{a,i}^{spr,n} = \sum_{j} \frac{1}{2} k_{actin,spr} (|\boldsymbol{x}_{a,j} - \boldsymbol{x}_{a,i}| - L0_{actin})^2 \tag{3.4}$$

where $k_{actin,spr}$ is the actin spring coefficient and $L0_{actin}$ is the resting length of the spring. Note that the sum is taken over the neighboring j actin nodes that are connected to the i^{th} actin node via a linear spring.

The bending energy is defined as follows [1, 163, 169]:

$$E_{a,i}^{bend,n} = \sum_{j \in S(i)} \frac{1}{2} k_{actin,bend} (\theta_{jik} - \theta_0)^2. \tag{3.5}$$

Here, the sum is taken over all of the actin node triplets (two adjacent segments), $S(i)$, that include node i. In this case, θ_{jik} represents the current angle between actin nodes j, i and k, where (j, i, k) represents three consecutive nodes in $S(i)$. Finally, θ_0 is the resting or equilibrium angle (i.e. the preferred angle) and $k_{actin,bend}$ is the bending spring constant.

When a pMyoII mini-filament node and an actin filamnet node are within a distance r_{conn}, chosen based on the length of a pMyoII mini-filament, an actomyosin connection is established. This connection is simulated based on a linear spring energy potential defined by [165]:

$$E_{a,i}^{actomyo-conn,n} \;=\; \frac{1}{2}k_{actomyo}(|\boldsymbol{x}_{a,i} - \boldsymbol{x}_{m,j}| \;-\; L0_{actomyo})^2 \tag{3.6}$$

where $k_{actomyo}$ is the spring constant, $L0_{actomyo}$ is the resting length, and $\boldsymbol{x}_{a,i}$ and $\boldsymbol{x}_{m,j}$ represent the positions of the i^{th} actin and j^{th} pMyoII nodes, respectively.

Upon establishing an actomyosin connection, the pMyoII node will exert a pulling force ($F_{a,i}^{myo-pull,n}$) on the actin filament node of magnitude $F_0^{myo-pull}$ [165, 166]. This pulling force is exerted tangentially along the actin filament and directed towards the barbed end ("+"), causing the filament to slide and allowing the pMyoII mini-filament to get closer to the barbed end.

Finally, each actin filament node experiences a stochastic force. This stochastic force term satisfies the Fluctuation-Dissipation Theorem [78] and is defined by

$$F_{a,i}^{stoch,n} \;=\; \sqrt{\frac{2k_BTC_a}{dt}}\xi_i \tag{3.7}$$

where k_B is the is the Boltzmann constant, T is the temperature, C_a is the actin drag coefficient, dt is the time step and ξ_i is sampled from a standard normal distribution.

3.3.4 Non-Muscle Myosin II Mini-Filament Sub-Model

The pMyoII mini-filaments in the actomyosin network are represented as a pair of nodes connected by a stiff linear spring (Fig 3.4 C), resembling the biological structure of the mini-filaments with several motor heads at both ends of the mini-filament [126]. Hence, each node that makes up the mini-filament represents a number of motor heads. Moreover, each pMyoII node in the mini-filament will interact with an actin filament node within range (within the length of the mini-filament) to form an actomyosin connection. Based on biological literature, we assume that once a connection is formed, the connected myosin node

moves along the actin filament in a single direction: towards the positive/barbed end of the actin filament [81, 125]. This movement is due to the pulling force a pMyoII node exerts on the actin filament nodes as it "walks" toward the barbed end of the filament. In return, this causes the actin filament to slide and leads to contraction of the actomyosin network.

Similar to the actin dynamics, the dynamics of pMyoII nodes are determined by the following Langevin equations in an overdamped regime [1, 24, 32, 163, 164]:

$$C_m \dot{\boldsymbol{x}}_{m,j} \;=\; F^{spr}_{m,j} \;+\; F^{actomyo-conn}_{m,j} \;+\; F^{myo-pull}_{m,j} \;+\; F^{stoch}_{m,j}. \tag{3.8}$$

Here C_m represents the pMyoII drag coefficient and $\boldsymbol{x}_{m,j}$ is the position of the j^{th} node of the m^{th} pMyoII mini-filament where $j \in 1, 2$. $F^{spr}_{m,j}$ represents the force due to the stiff linear spring connecting the pair of pMyoII nodes while $F^{actomyo-conn}_{m,j}$ represents the spring forces that connect the actin and pMyoII nodes upon an actomyosin connection. $F^{myo-pull}_{m,j}$ is the pMyoII pulling force that is exerted when a myosin node connects to an actin node. Finally, each pMyoII node experiences a stochastic force, $F^{stoch}_{m,j}$, satisfying the Fluctuation-Dissipation Theorem [78].

As before, the system of equations 3.8 is solved using a Forward Euler scheme:

$$\boldsymbol{x}^{n+1}_{m,j} \;=\; \boldsymbol{x}^{n}_{m,j} \;+\; \frac{dt}{C_m}\left(F^{spr,n}_{m,j} \;+\; F^{actomyo-conn,n}_{m,j} \;+\; F^{myo-pull,n}_{m,j} \;+\; F^{stoch,n}_{m,j}\right). \tag{3.9}$$

Similar to Equation 3.3, the supercripts n and $n+1$ in Equation 3.9 represent subsequent time points and dt represents the time step.

The spring force exerted on each pMyoII node is calculated based on the negative gradient of energy. Mainly, we define $F^{spr,n}_{m,j} \;=\; -\nabla E^{spr,n}_{m,j}$ where

$$E^{spr,n}_{m,j} \;=\; \sum_{j=1}^{2} \frac{1}{2} k_{myo,spr}(|\boldsymbol{x}_{m,j} - \boldsymbol{x}_{m,k}| \;-\; L0_{myo})^2 \tag{3.10}$$

where $k_{myo,spr}$ is the pMyoII spring coefficient and $L0_{myo}$ is the resting length of the spring. Since we have established that each m^{th} pMyoII mini-filament is composed of two nodes

with positions $\boldsymbol{x}_{m,j}$ where $j \in 1, 2$ ($\boldsymbol{x}_{m,1}$ and $\boldsymbol{x}_{m,2}$), then we can rewrite Equation 3.10 in terms of each node in the mini-filament:

$$E_{m,1}^{spr,n} = \frac{1}{2} k_{myo,spr}(|\boldsymbol{x}_{m,2} - \boldsymbol{x}_{m,1}| - L0_{myo})^2 \tag{3.11}$$

$$E_{m,2}^{spr,n} = \frac{1}{2} k_{myo,spr}(|\boldsymbol{x}_{m,1} - \boldsymbol{x}_{m,2}| - L0_{myo})^2. \tag{3.12}$$

When an actomyosin connection is established, the connected pMyoII node will experience $F_{m,j}^{actomyo-conn}$ defined similarly to Equation 3.6 of the previous section. Upon this connection, the node will also experience a pulling force $F_{m,j}^{myo-pull,n}$, which is of equal and opposite magnitude to $F_{a,i}^{myo-pull,n}$ (the force the pMyoII node exerts on the actin node).

Each pMyoII mini-filament node will also experience a stochastic force, satisfying the Fluctuation-Dissipation Theorem [78], to represent the thermal and random forces acting on each pMyoII node:

$$F_{m,j}^{stoch,n} = \sqrt{\frac{2k_B T C_m}{dt}} \xi_j \tag{3.13}$$

where k_B is the is the Boltzmann constant, T is the temperature, C_m is the pMyoII drag coefficient, dt is the time step and ξ_j is sampled from a standard normal distribution.

3.3.5 Actin-pMyoII Connections

Unbound pMyoII mini-filaments move freely within the network until they find a neighboring actin filament to bind to (Fig 3.5 A). Initially and for simplicity, we assume that an actomyosin connection is formed when an unbound pMyoII mini-filament and an actin filament are within range. In other words, if the distance between an actin filament node ($\boldsymbol{x}_{a,i}$) and a pMyoII mini-filament node ($\boldsymbol{x}_{m,j}$) is less than or equal to a connection radius (r_{conn}), a connection is established (Fig 3.5 A). We assume that the connection radius is equal to the equilibrium length of a pMyoII mini-filament. Moreover, similar to [165], the actomyosin connection is represented by a linear spring denoted by $F^{actomyo-conn}$ in Equations 3.3 and 3.9 and defined in Equation 3.6. The pMyoII node will move along the actin filament until it reaches the barbed end by exerting a pulling force, $F^{myo-pull}$ (Fig

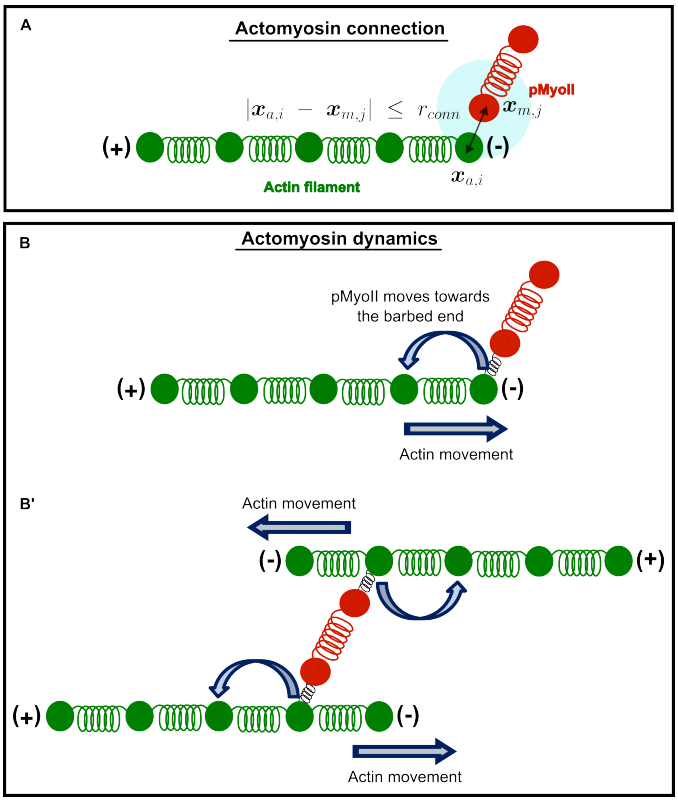

Figure 3.5: **Diagram of actomyosin connections.** (A) A connection is formed when an actin filament node and a pMyoII mini-filament node are within range (r_{conn}). The connection radius is colored in light blue. The actin filament is shown in green with its barbed (+) and pointed (-) ends labeled. The pMyoII mini-filament is shown in red. (B) The connected mini-filament will move towards the barbed end of the filament. As it moves, it will exert a pulling force that will slide the actin filament. (B') Representation of the dynamics of a pMyoII mini-filament bound to two anti-parallel actin filaments.

3.5 B, B'). Once the barbed end is reached, the actin and pMyoII nodes will disconnect, setting $F^{actomyo-conn} = 0$. If, at any point in time, the distance between the connected nodes (actin-pMyoII) becomes greater than r_{conn}, the nodes will disconnect as they are no longer in range and $F^{actomyo-conn} = 0$. Since each mini-filament is composed of a pair of nodes ($\boldsymbol{x}_{m,1}$ and $\boldsymbol{x}_{m,2}$), we assume that if one of the nodes (for example $\boldsymbol{x}_{m,1}$) forms a connection with an actin filament, the pairing pMyoII node ($\boldsymbol{x}_{m,2}$) cannot bind to the same actin filament.

3.3.6 Measuring Contraction of the Simulated Actomyosin Network

Previous studies have shown that an actomyosin network can either contract or expand, although most networks are predominantly contractile [125, 128, 152, 153]. To be able to determine whether contraction or expansion of the network is taking place, we need to estimate the size of the network. To do so, we developed a pipeline on MATLAB to estimate the simulated network's size, which consists of surrounding the actomyosin network with a disc or border (Fig 3.6), similar to Belmonte et al. [170].

First, we calculate the center of the network C as the mean of all network nodes:

$$C \;=\; \frac{1}{N}\sum_{i} \boldsymbol{X}_i \tag{3.14}$$

where $\boldsymbol{X}_i$ is the position of the i^{th} node in the actomyosin network and N is the total number of nodes in the network. Note that for $\boldsymbol{X}_i$ and N, we consider both types of nodes, i.e. actin and pMyoII nodes.

Then, the size of the network is determined based on the network radius R, which we define as the maximum distance between the center C and the furthest network node:

$$R \;=\; max(dist(C, \boldsymbol{X}_i)). \tag{3.15}$$

Please see Figure 3.6 for an example of the implementation of this pipeline.

To determine whether the actomyosin network undergoes contraction or expansion, we compare the network size at the start and end of a simulation. More specifically, we compare the initial ($R_{initial}$) and final (R_{final}) radii associated with the initial and final network configurations, respectively. Note that both $R_{initial}$ and R_{final} are defined according to Equation 3.15. If $R_{initial} > R_{final}$, then the network condenses, meaning that contraction occurs. On the other hand, if $R_{initial} < R_{final}$, then we have a case of network expansion.

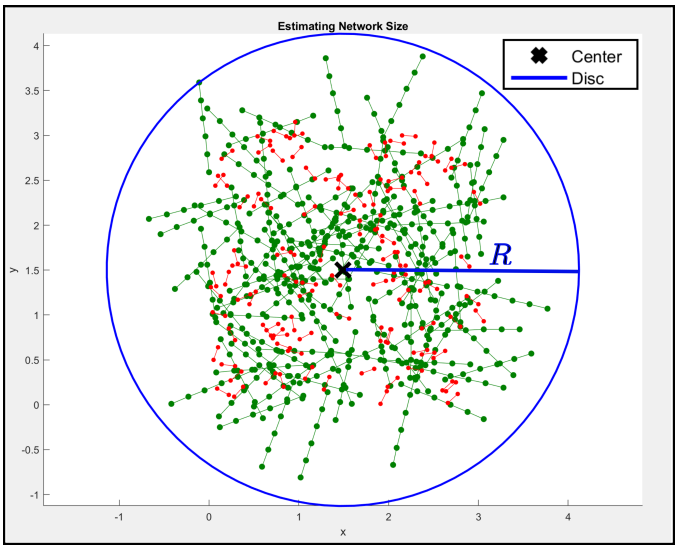

Figure 3.6: **Estimating the size of the actomyosin network.** A MATLAB script is used to surround the actomyosin network with a disc of radius R. The actin filaments are shown in green, while the pMyoII mini-filaments are in red. The disc that surrounds the network is shown in blue and the center of the network is marked by a bold **x**. The network was overlaid with a blue line connecting the center of the network to the disc to show the definition of the radius R.

3.3.7 Plans for Model Calibration

Once the actomyosin network model is integrated with the SCE model of the wing disc presented in Chapter 2, we will calibrate the network model for our specific biological application using experimental data. This data will be provided by our collaborators in Dr. Zartman's Lab. For example, we can use the local actin and pMyoII densities to determine the number of actin filaments and pMyoII mini-filaments in the network. If experimentally feasible, experimental images of the wing disc that provide information about the stress distribution of the network or the elastic properties of the actin filaments would be crucial data sets for model calibration.

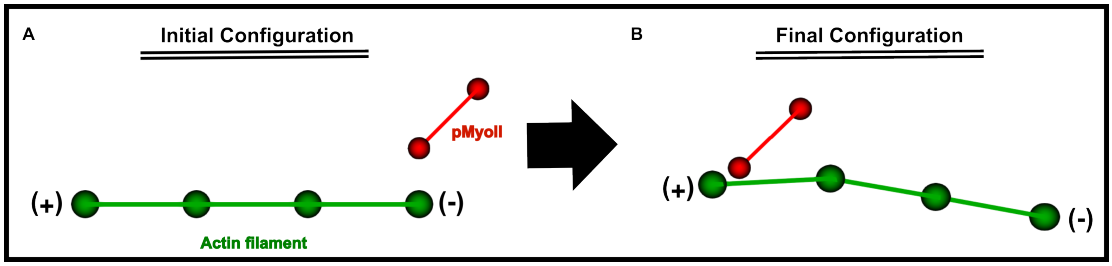

Figure 3.7: **Simulated actomyosin interactions.** (A) Initial configuration of the simulation. An actin filament and a pMyoII mini-filament are shown in green and red, respectively. The actin filament barbed (+) and pointed (-) ends have been labeled. (B) Final configuration. The pMyoII mini-filament reached the barbed end and translocated the actin filament.

3.4 Preliminary Simulation Results

As previously mentioned, the end goal of this study is to create an actomyosin network submodel that can be incorporated with our multi-scale model from Chapter 2 [1] to replace the simplified representation of actomyosin in the multi-scale model and allow us to capture the dynamics of actin filaments and pMyoII mini-filaments. For model verification purposes, we first present the results of model simulations at the single actin filament and pMyoII mini-filament level. Note that all simulations presented in this section were run using the parameter values presented in Appendix B Table B.1.

As a first study and proof of concept, we focused on capturing the interactions between the network components based on their known biological interactions. More specifically, simulations at the single actin and pMyoII levels were conducted. Based on biological literature, pMyoII mini-filaments are assumed to move along the actin filament in a directed manner: always towards the barbed end. This directed movement causes the actin filaments to slide and translocate in space (see Fig 3.7). Additionally, in a simulation where two actin filaments are interacting with a single mini-filament, we observe that the actin filaments will slide relative to one another as the pMyoII move towards the barbed end of their respective actin filament (see Fig 3.8). In particular, we notice that the actin filaments end up being parallel to one another as compared to their initial configuration (Fig 3.8 B).

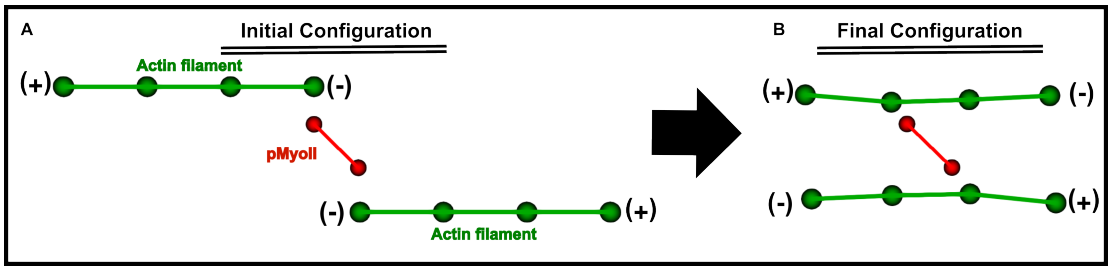

Figure 3.8: **Simulated actomyosin interactions between two actin filaments and a pMyoII mini-filament.** (A) Initial configuration of a simulation with two anti-parallel actin filaments (shown in green). (B) The pMyoII mini-filament (shown in red) connects with each actin filament and slides them past one another causing the filaments to contract.

It is worth noting that the number of actin filaments in these initial simulations, along with their number of nodes, were chosen at random. However, the computational model has the capability of accounting for several actin filaments at a time, each composed of more nodes than shown in these simulations. Moreover, the actin filaments in the network can either have the same number of nodes or differ in node number (i.e. the number of nodes varies per filament). Regardless of the scenario, the mini-filament will move the actin filament as it exerts a pulling force. Finally, the number of nodes we choose in each actin filament will depend on the level of coarse-graining and the experimental data available to us during the calibration of the model for our specific biological application.

3.4.1 Testing Contraction vs Extension With Two Actin Filaments and a Single pMyoII Mini-Filament

As mentioned earlier, depending on the arrangement of the actin filament polarity with respect to their bound pMyoII mini-filaments, contractile or extensile forces can be produced [81, 125, 128]. In other words, some configurations might give rise to network contraction while others will cause network expansion. A review by Murrell et al. proposes two different network configurations that are expected to give rise to either contraction or expansion (see Figure 2 of [81]). We ran simulations using these setups, which consisted of two anti-parallel actin filaments and a pMyoII mini-filament between them (see Fig 3.9).

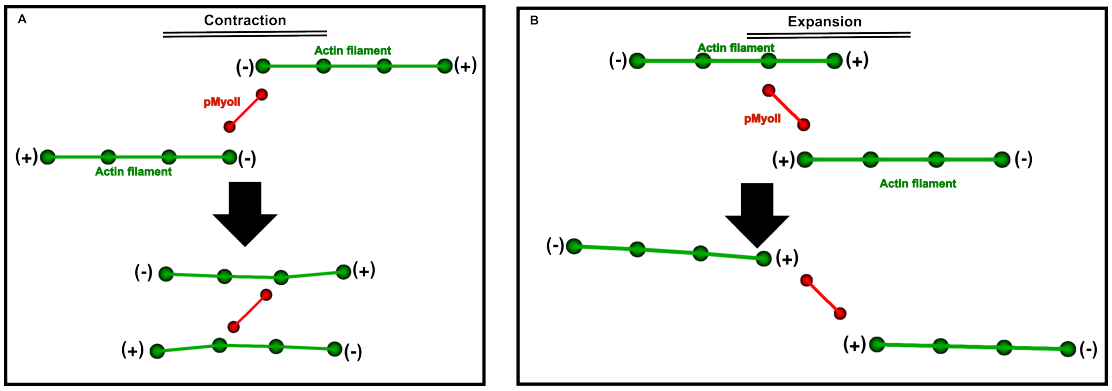

Figure 3.9: **Simulated scenarios of actomyosin contraction vs expansion.** (A) Sample simulation result of contraction. As the pMyoII mini-milament (in red) moves along the actin filaments towards the barbed end (+) and exerts a pulling force on them, the actin filaments will move. This interaction induces contraction (bottom panel under the black arrow). (B) Sample simulation result of expansion. In this case, the pMyoII mini-filament force being exerted on the actin filaments (shown in green) causes the filaments to slide further away from one another, resulting in expansion.

In the first simulation (Fig 3.9 A), the first filament has its barbed end at the first node (bottom filament), while the second filament's barbed end is the last node (top filament). Our simulation result captures contraction, where the simulated filaments are now parallel to each other. On the other hand, in the second simulation (Fig 3.9 B), where the barbed end of both actin filaments is towards the center and very close to the pMyoII mini-filament, we observe expansion, as suggested in [81]. In this case, the pMyoII pulling force moves the actin filaments further away from each other. Thus, our model is capable of recapitulating both contraction and expansion as proposed by Murrell et al. [81].

3.4.2 The Arrangement of the Actin Filament Polarity Affects the Overall Contractility of the Actomyosin Network

As previously mentioned, an actomyosin network can either contract or expand, although most networks favor contraction [125, 128, 152, 153]. One factor that is believed to influence the contractility of a network is the polarity of actin filaments [81, 125]. To test the effect of polarity arrangement on the overall contractility or expansion of the network, we ran

simulations with different actin filament polarity configurations. In these simulations, we used a randomly organized actomyosin network structure, meaning that the actin filaments' positions and orientations were chosen at random. We then changed the polarity of the actin filaments by changing the position of the barbed ends. In the first simulation (Fig 3.10), the barbed ends of the actin filaments were predominantly positioned facing toward the periphery of the network. In the second simulation (Fig 3.11), we set the barbed ends of the actin filaments facing toward the center of the network. Note that in both simulations, we used the same network configuration and only changed the polarity of the actin filaments, i.e., the position of the barbed ends. We then used the MATLAB pipeline presented in section 3.3.6 of Methods to determine the contractile performance of the actomyosin network in each simulation scenario.

In the first simulation scenario, $R_{initial} > R_{final}$ meaning that the network condensed and favored contractility (Fig 3.10 B'). In comparison, $R_{initial} < R_{final}$ in the second simulation, capturing a case of network expansion (Fig 3.11 B'). Notice that in this second case, the pMyoII mini-filaments are mainly concentrated in the center of the network. This is because the barbed ends of the actin filaments are majorly facing toward the center of the network, and since the mini-filaments only move towards the barbed end, they end up being "trapped" in the center. This type of behavior is in accordance with studies of aster formation such as Miller et al., where the barbed ends of the filaments are concentrated toward the center of the network and, similarly, confine the mini-filaments to the aster core [171].

Overall, these sample simulations are in agreement with other studies [81, 125] that suggest that the polarity arrangement of the actin filaments (the position of the barbed ends) does influence the network's capability to favor contractile or extensile forces.

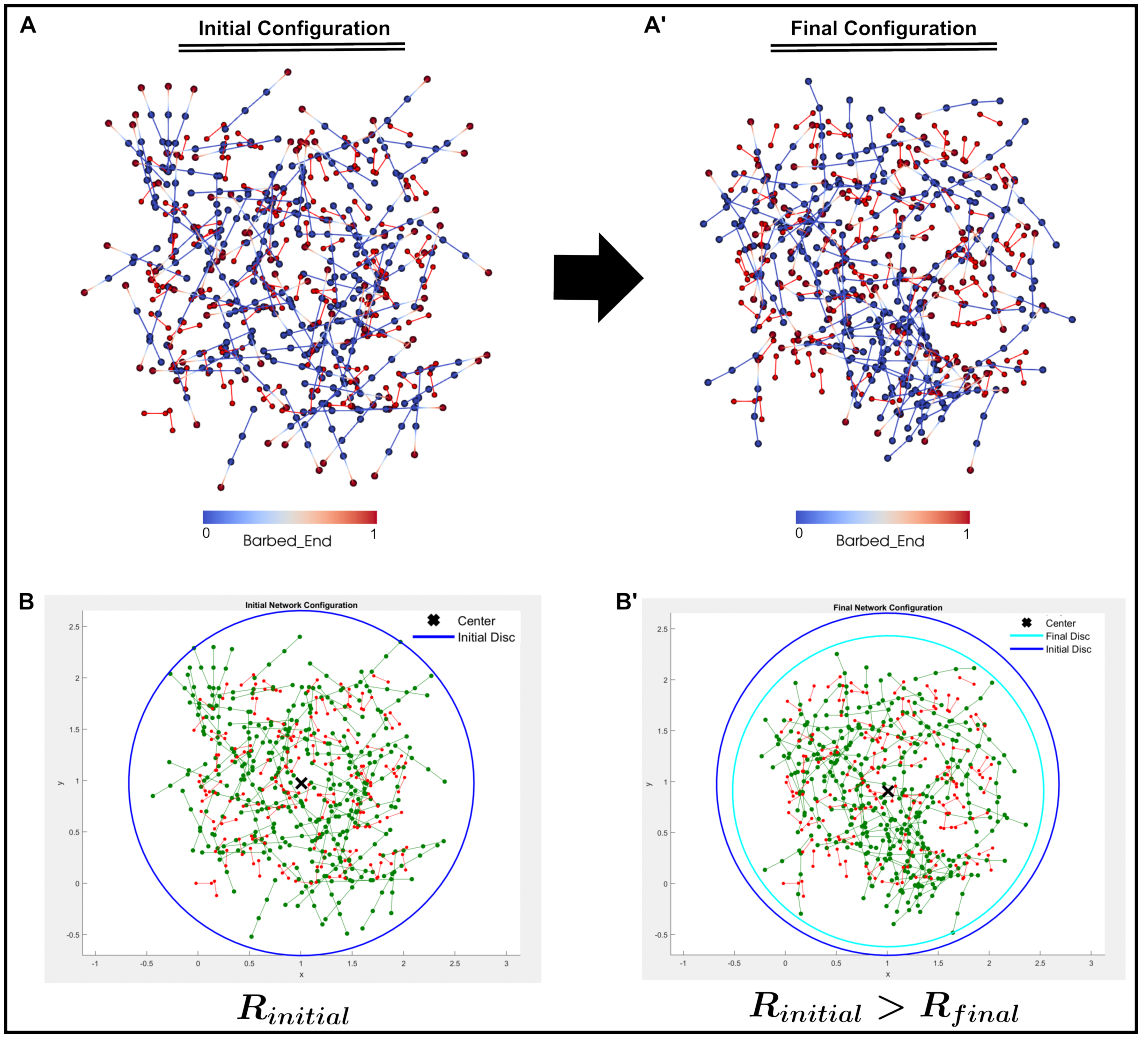

Figure 3.10: **Results of the first simulation scenario testing the effect of the actin filament polarity configuration on the overall contractility of the network.** (A) Initial network configuration with the barbed ends of the actin filaments mainly concentrated towards the periphery of the network. The actin filaments are colored blue, with their respective barbed end colored dark red. The pMyoII mini-filaments are in red. (A') Final network configuration. (B) Estimating the network size of the initial network configuration using the MATLAB pipeline. Actin filaments are in green while mini-filaments are in red. (B') Estimating the network size of the final configuration. Comparison between the initial and final network size shows that $R_{initial} > R_{final}$. This denotes a case of network contraction.

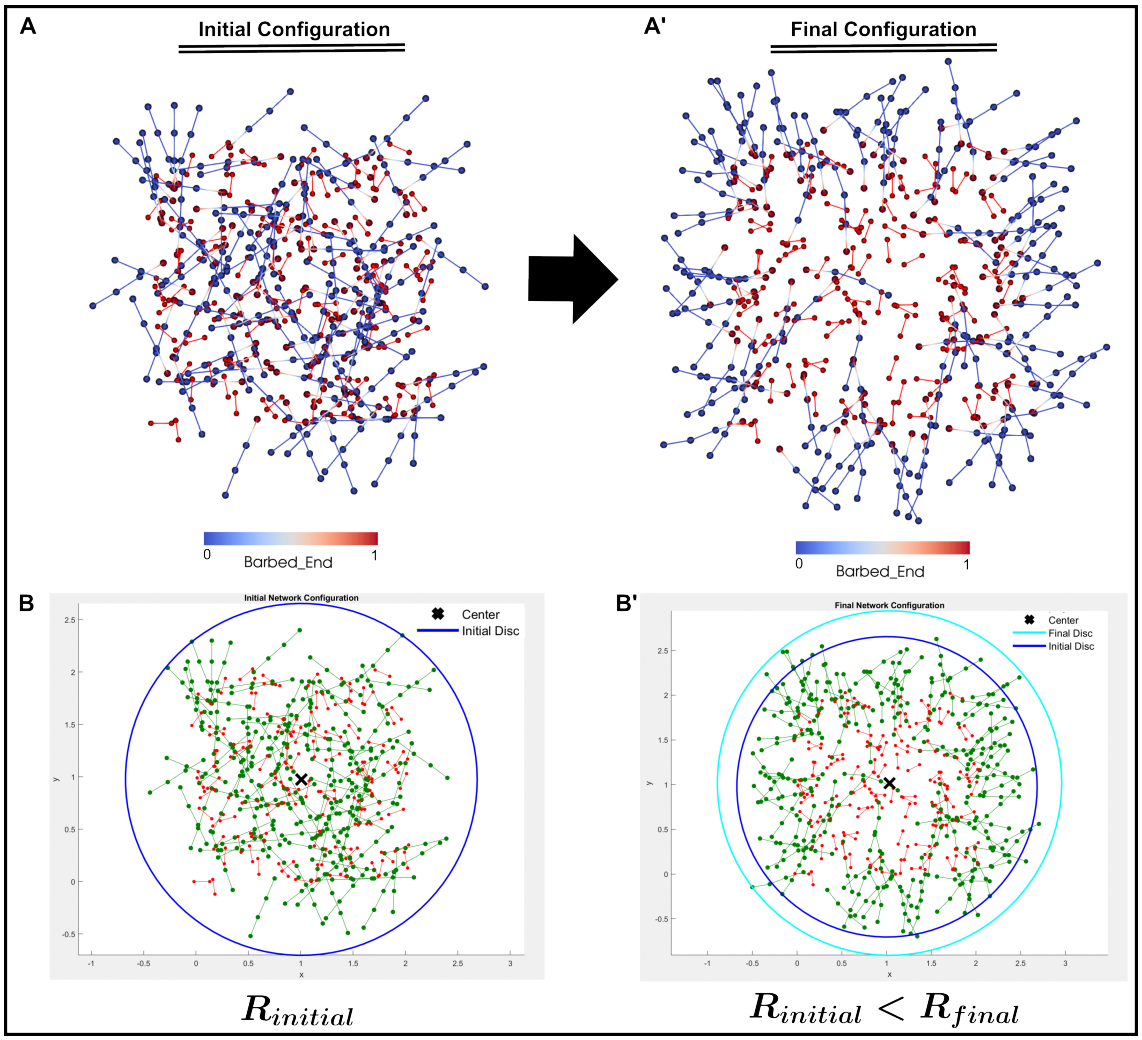

Figure 3.11: **Results of the second simulation scenario testing the effect of the actin filament polarity configuration on the overall contractility of the network.** (A) Initial network configuration. In this case, the barbed ends of actin filaments are positioned towards the center of the network. As before, the actin filaments are colored blue, the barbed ends are colored dark red and the pMyoII mini-filaments are in red. (A') Final network configuration. (B) Utilized the MATLAB pipeline to estimate the network size of the initial network configuration. Actin filaments and pMyoII mini-filaments are colored in green and red, respectively. (B') Estimating the network size of the final configuration (light blue disc). Comparison between the initial and final network size shows that $R_{initial} < R_{final}$. This denotes a case of network expansion.

3.5 Discussion and Future Work

In this chapter, we develop a mathematical and computational framework of the actomyosin network dynamics. We assume that the network is composed of actin filaments and pMyoII mini-filaments, the two most essential components for contractility of the network [128]. In this model, a node and spring modeling approach is used to simulate both of the model components where actin and pMyoII dynamics are described by overdamped Langevin equations. In other words, the motion of each type of node (actin or pMyoII) is represented by solving stochastic ordinary differential equations using a forward Euler numerical scheme. In accordance with previous studies, our model also demonstrates that the polarity arrangement of the actin filaments plays a key role in the overall contractility of the network [81, 125, 128, 154, 155].

This modeling framework is the first step towards a larger and more complex end goal. More specifically, this actomyosin network model will be coupled with the SCE model of the *Drosophila* wing disc development presented in Chapter 2, in order to replace the simplified representation of actomyosin in the SCE model. The coupled model will be used to test a novel biological hypothesized mechanism of how the actomyosin network constricts the basal membrane of columnar cells leading to interkinetic nuclear migration. We refer to this mechanism as the "zipping-up" mechanism, where we believe a combination of both vertical and horizontal contractile forces constrict the membrane. Thus, to test this mechanism, there is a need for a coupling between models. During the coupling, a linear spring will be introduced to connect the actomyosin network with the membrane nodes, resembling adhesion proteins. In addition, introducing a Morse potential might also be necessary to ensure the network stays within the cells. Once coupled, the actomyosin network model will be calibrated using experimental data. The plans for model calibration have been provided in subsection 3.3.7 of Methods.

In addition to testing the hypothesized "zipping-up" mechanism, once the models have been coupled and the actomyosin network model has been calibrated, we also want to explore

other possible mechanisms that can influence the network contractility and its ability to constrict the basal membrane of simulated columnar cells. For example, testing the effect of the actin filament polarity arrangement is important as it can either produce network contraction or expansion [81, 125, 128]. In addition, a study by Popov et al. has shown that increasing the pMyoII concentration increases the contractility of the network [181]. Hence, we will need to explore the role of varying the pMyoII mini-filament concentration relative to the actin filament concentration on the overall contractile behavior of the network. Finally, another mechanism we can test is to vary the number of actin filaments the pMyoII mini-filaments can bind to in order to explore whether a mini-filament's ability to bind to more than one actin at a time will either enhance or hinder contractility.

Another important focus of future work would be to introduce more biological model components impacting the dynamics of the actomyosin network and study their effect on the overall network contractility in the context of columnar epithelial cells. Some of these new modeling components include introducing binding and unbinding rates of pMyoII mini-filaments and polymerization and depolymerization of actin filaments. Note that implementing polymerization and depolymerization would be done at a coarse-grained level.

Finally, since the actomyosin network generates the actomyosin contractility within cells, it is important to other biological processes outside of tissue morphogenesis. Hence, the model presented in this chapter is not limited to its novelty and biological relevance in early development but can be applied to study the role of actomyosin contractility in other processes, such as cancer invasion, wound healing, and plant growth.

3.6 Code Availability

A C++ implementation of the computational model and any MATLAB scripts presented in this chapter are available upon request from the first author (Jennifer Rangel Ambriz) or faculty advisor (Mark Alber).

Chapter 4

Conclusions and Future Work

Mathematical and computational modeling has become an increasingly popular and powerful tool for studying outstanding questions in developmental biology. Some of the many benefits of mathematical and computational modeling include (1) efficiently simulating complex biological systems, (2) using simulations to run *in silico* experiments, and (3) motivating new experiments based on the model predictions. In this work, specifically Chapter 2, we combine mathematical and computational modeling with experimental data to reverse-engineer mechanisms regulating proper *Drosophila* wing disc development. In particular, we present a novel multi-scale SCE model of the wing disc cross-section along the AP axis. Novel features of the model include the non-homogeneous spatial patterning of mechanical regulators and a detailed algorithm of cell proliferation and growth, which captures the interkinetic nuclear migration process of the pseudostratified epithelium. In Chapter 3, we present a mathematical model of a two-dimensional actomyosin network and its computational implementation towards the goal of coupling this model with the SCE model of the wing disc. This coupling will allow us to get insights into the mechanism of how actomyosin coordinates and gives rise to the contractile forces that constrict the basal membrane of columnar cells, driving the apical migration of the nuclei and leading to successful cell division.

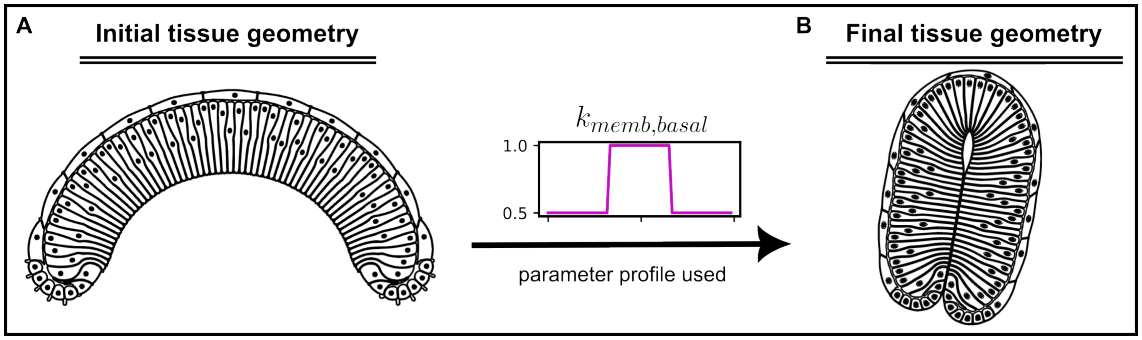

Figure 4.1: **Preliminary simulation gives insights into a possible mechanism driving wing disc eversion and motivates future work.** (A) Simulated initial tissue geometry produced from the multi-scale model presented in Chapter 2 [1]. A spatial patterning of the parameter $k_{memb,basal}$ is applied where $k_{memb,basal}$ is higher in the center of the pouch. (B) Final tissue geometry capturing an eversion-like phenotype.

In the future, we would also like to use the subcellular element modeling approach to investigate later stages of *Drosophila* wing development. Particularly, we would like to study eversion, a late-stage morphogenetic process that involves the outward folding of the wing disc [172]. Successful eversion consists of several processes including but not limited to cellular rearrangements and shape changes, bending of the pouch, a decrease in pouch cell height, and expansion of the wing blade [11, 162, 172–174]. A preliminary simulation using the multi-scale model presented in Chapter 2, where the basal membrane tension is spatially patterned (higher in the center of the pouch), generates an eversion-like phenotype (Fig 4.1). Thus, the non-uniform spatial patterning of basal membrane tension might be a possible mechanism driving wing disc eversion that is worth exploring further, both computationally and experimentally. Overall, the multi-scale model described in this dissertation can be extended and used to obtain insights into other biological processes and developmental stages of wing disc morphogenesis.

Bibliography

[1] Nilay Kumar, Jennifer Rangel Ambriz, Kevin Tsai, Mayesha Sahir Mim, Marycruz Flores-Flores, Weitao Chen, Jeremiah J. Zartman, and Mark Alber, *Balancing competing effects of tissue growth and cytoskeletal regulation during Drosophila wing disc development*, Nat Commun **15** (2024), no. 2477.

[2] T. E. Saunders and P. W. Ingham, *Open questions: how to get developmental biology into shape?*, BMC Biol **17** (2019), no. 17.

[3] S. Urdy, N. Goudemand, and S. Pantalacci, *Chapter Seven - Looking Beyond the Genes: The Interplay Between Signaling Pathways and Mechanics in the Shaping and Diversification of Epithelial Tissues*, Curr Top Dev Biol **119** (2016), 227–290.

[4] Thomas Iskratsch, Haguy Wolfenson, and Michael P. Sheetz, *Appreciating force and shape—the rise of mechanotransduction in cell biology*, Nat. Rev. Mol. Cell Biol. **15** (2014), 823–833.

[5] Nicole Gorfinkiel and Alfonso Martinez Arias, *The cell in the age of the genomic revolution: Cell Regulatory Networks*, Cells Dev. **168** (2021), no. 203720.

[6] Vijay Velagala, Weitao Chen, Mark Alber, and Jeremiah J. Zartman, *Chapter 4.1 - Multiscale Models Coupling Chemical Signaling and Mechanical Properties for Studying Tissue Growth*, Mechanobiology (Elsevier) (2020), 173–195.

[7] Cody Narciso and Jeremiah J. Zartman, *Reverse-engineering organogenesis through feedback loops between model systems*, Curr. Opin. Biotechnol. **52** (2018), 1–8.

[8] Q. Wu, N. Kumar, V. Velagala, and J.J. Zartman, *Tools to reverse-engineer multicellular systems: case studies using the fruit fly*, J. Biol. Eng. **13** (2019), no. 33.

[9] Alejandro F. Villaverde and Julio R. Banga, *Reverse engineering and identification in systems biology: strategies, perspectives and challenges*, J. R. Soc. Interface **11** (2014), no. 20130505.

[10] Marie E. Csete and John C. Doyle, *Reverse engineering of biological complexity*, Science **295** (2002), 1664–1669.

[11] Thomas J. Widmann and Christian Dahmann, *Dpp signaling promotes the cuboidal-to-columnar shape transition of Drosophila wing disc epithelia by regulating Rho1*, J. Cell Sci. **122** (2009), 1362–1373.

[12] N.J. Kirkland, A.C. Yuen, M. Tozluoglu, N. Hui, E.K. Paluch, and Y. Mao, *Tissue Mechanics Regulate Mitotic Nuclear Dynamics during Epithelial Development.*, Curr. Biol. **30** (2020), 2419–2432.e4.

[13] E. J. Meyer, A. Ikmi, and M. C. Gibson, *Interkinetic nuclear migration is a broadly conserved feature of cell division in pseudostratified epithelia*, Curr. Biol. **21** (2011), 485—491.

[14] R. M. Neto-Silva, B. S. Wells, and L. A. Johnston, *Mechanisms of growth and homeostasis in the Drosophila wing*, Annu. Rev. Cell Dev. Biol. **25** (2009), 197–220.

[15] E. Hannezo, J. Prost, and J.-F. Joanny, *Theory of epithelial sheet morphology in three dimensions*, Proc. Natl Acad. Sci. **111** (2014), 27–32.

[16] Jeremiah J. Zartman and Stanislav Y. Shvartsman, *Unit operations of tissue development: epithelial folding*, Annu. Rev. Chem. Biomol. Eng. **1** (2010), 231–246.

[17] J. Walpole, J. A. Papin, and S. M. Peirce, *Multiscale computational models of complex biological systems*, Annu. Rev. Biomed. Eng. **15** (2013), 137–154.

[18] G. W. Brodland, *How computational models can help unlock biological systems*, Semin. Cell Dev. Biol. **47–48** (2015), 62–73.

[19] Bipin K. Tripathi and Kenneth D. Irvine, *The wing imaginal disc*, Genetics **220** (2020), iyac020.

[20] Paloma Dominguez-Gimenez, Nicholas H. Brown, and Maria D. Martin-Bermudo, *Integrin-ECM interactions regulate the changes in cell shape driving the morphogenesis of the Drosophila wing epithelium*, J. Cell Sci. **120** (2007), 1061–1071.

[21] J. C. Pastor-Pareja and T. Xu, *Shaping cells and organs in drosophila by opposing roles of fat body-secreted Collagen IV and Perlecan*, Dev. Cell **21** (2011), 245–256.

[22] C. M. Nelson, *Geometric control of tissue morphogenesis*, Biochim. Biophys. Acta **1973** (2009), 903–910.

[23] M. Tozluoğlu, M. Duda, N. J. Kirkland, R. Barrientos, J. J. Burden, J. J. Muñoz, and Y. Mao, *Planar differential growth rates initiate precise fold positions in complex epithelia*, Dev. Cell **51** (2019), 299–312.e4.

[24] A. Nematbakhsh, M. Levis, N. Kumar, W. Chen, J. J. Zartman, and M. Alber, *Epithelial organ shape is generated by patterned actomyosin contractility and maintained by the extracellular matrix*, PLoS Comput Biol. **16** (2020), e1008105.

[25] S. Harmansa, A. Erlich, C. Eloy, G. Zurlo, and T. Lecuit, *Growth anisotropy of the extracellular matrix shapes a developing organ*, Nat. Commun. **14** (2023), no. 1220.

[26] Raphaël Etournay, Marko Popović, Matthias Merkel, Amitabha Nandi, Corinna Blasse, Benoît Aigouy, Holger Brandl, Gene Myers, Guillaume Salbreux, Frank Jülicher, and Suzanne Eaton, *Interplay of cell dynamics and epithelial tension during morphogenesis of the Drosophila pupal wing*, eLife **4** (2015), e07090.

[27] Boris Guirao, Stéphane U. Rigaud, Floris Bosveld, Anaïs Bailles, Jesús López-Gay, Shuji Ishihara, Kaoru Sugimura, François Graner, and Yohanns Bellaïche, *Unified quantitative characterization of epithelial tissue development*, eLife **4** (2015), e08519.

[28] M. C. Diaz de la Loza and B. J. Thompson, *Forces shaping the Drosophila wing*, Mech. Dev. **144** (2017), 23–32.

[29] J. Gou, J. A. Stotsky, and H. G. Othmer, *Growth control in the Drosophila wing disk*, WIREs Syst. Biol. Med. **12** (2020), e1478.

[30] J. Capdevila and I. Guerrero, *Targeted expression of the signaling molecule decapentaplegic induces pattern duplications and growth alterations in Drosophila wings*, EMBO J. **13** (1994), 4459–4468.

[31] R. P. Ray, T. Nakata, P. Henningsson, and R. J. Bomphrey, *Enhanced flight performance by genetic manipulation of wing shape in Drosophila*, Nat. Commun. **7** (2016), 10851.

[32] A. Nematbakhsh, W. Sun, P. A. Brodskiy, A. Amiri, C. Narciso, Z. Xu, J. J. Zartman, and M. Alber, *Multi-scale computational study of the mechanical regulation of cell mitotic rounding in epithelia*, PLoS Comput. Biol. **13** (2017), e1005533.

[33] Christopher R. Sweet, Santanu Chatterjee, Zhiliang Xu, Katharine Bisordi, Elliot D. Rosen, and Mark Alber, *Modelling platelet–blood flow interaction using the subcellular element Langevin method*, J. R. Soc. Interface **8** (2011), 1760–1771.

[34] O. Wartlick et al., *Dynamics of Dpp Signaling and Proliferation Control*, Science **331** (2011), 1154–1159.

[35] F. Hamaratoglu, A. M. de Lachapelle, G. Pyrowolakis, S. Bergmann, and M. Affolter, *Dpp Signaling Activity Requires Pentagone to Scale with Tissue Size in the Growing Drosophila Wing Imaginal Disc*, PLoS Biol. **9** (2011), e1001182.

[36] M. Chugh, A. Munjal, and S. G. Megason, *Hydrostatic pressure as a driver of cell and tissue morphogenesis*, Semin. Cell. Dev. Biol. **131** (2022), 134–145.

[37] D. S. Straus, *Effects of insulin on cellular growth and proliferation*, Life Sci. **29** (1981), 2131–2139.

[38] B. D. Hopkins, M. D. Goncalves, and L. C. Cantley, *Insulin–PI3K signalling: an evolutionarily insulated metabolic driver of cancer*, Nat. Rev. Endocrinol. **16** (2020), 276–283.

[39] I. Orlova, L. Silver, and G. Gallo, *Regulation of actomyosin contractility by PI3K in sensory axons*, Dev. Neurobiol. **67** (2007), 1843–1851.

[40] H. Zhang, J. P. Stallock, J. C. Ng, C. Reinhard, and T. P. Neufeld, *Regulation of cellular growth by the Drosophila target of rapamycin dTOR*, Genes Dev. **14** (2000), 2712–2724.

[41] A. Ducuing, C. Keeley, B. Mollereau, and S. Vincent, *A DPP-mediated feed-forward loop canalizes morphogenesis during Drosophila*, Dors. Clos. J. Cell Biol. **208** (2015), 239–248.

[42] L. A. Johnston, D. A. Prober, B. A. Edgar, R. N. Eisenman, and P. Gallant, *Drosophila myc Regulates Cellular Growth during Development*, Cell **98** (1999), 779–790.

[43] D. Nellen, R. Burke, G. Struhl, and K. Basler, *Direct and Long-Range Action of a DPP Morphogen Gradient*, Cell **85** (1996), 357–368.

[44] V. Sauzeau, I. M. Berenjeno, C. Citterio, and X. R. Bustelo, *A transcriptional cross-talk between RhoA and c-Myc Inhibts the RhoA/Rock-dependent cytoskeleton*, Oncogene **29** (2010), 3781–3792.

[45] S. Boudjadi, J. C. Carrier, J.-F. Groulx, and J.-F. Beaulieu, *Integrin $\alpha 1\beta 1$ expression is controlled by c-MYC in colorectal cancer cells*, Oncogene **35** (2016), 1671–1678.

[46] T. C. Seher and M. Leptin, *Tribbles, a cell-cycle brake that coordinates proliferation and morphogenesis during Drosophila gastrulation*, Curr. Biol. **10** (2000), 623–629.

[47] M. Eiraku et al., *Self-organizing optic-cup morphogenesis in three-dimensional culture*, Nature **472** (2011), 51–56.

[48] S. Aldaz, L. M. Escudero, and M. Freeman, *Dual role of myosin II during Drosophila imaginal disc metamorphosis*, Nat. Commun. **4** (2013), no. 1761.

[49] A. Ramezani et al., *A multiscale chemical-mechanical model predicts impact of morphogen spreading on tissue growth*, Npj Syst. Biol. Appl. **9** (2023), 1–12.

[50] B. K. Chauhan, M. Lou, Y. Zheng, and R. A. Lang, *Balanced Rac1 and RhoA activities regulate cell shape and drive invagination morphogenesis in epithelia*, Proc. Natl Acad. Sci. **108** (2011), 18289–18294.

[51] O. Aydin et al., *Principles for the design of multicellular engineered living systems*, APL Bioeng. **6** (2022), 010903.

[52] P.A. Brodskiy et al., *QuickStitch for seamless stitching of confocal mosaics through high-pass filtering and recursive normalization*, bioRxiv (2016), 075440.

[53] M. Weigert et al., *Content-aware image restoration: pushing the limits of fluorescence microscopy*, Nat. Methods **15** (2018), 1090–1097.

[54] C. A. Schneider, W. S. Rasband, and K. W. Eliceiri, *NIH Image to ImageJ: 25 years of image analysis*, Nat. Methods **9** (2012), 671–675.

[55] U. Schmidt, M. Weigert, C. Broaddus, and G. Myers, *Cell Detection Star.-convex Polyg.*, Journal (use abbreviations if appropriate **11071** (2018), 265–273.

[56] G. Snecdecor and W. Cochran, *Statistical Methods, 8th Edition*, Wiley, Iowa State University Press, Ames, 1989.

[57] J. Cohen, *Statistical Power Analysis for the Behavioral Sciences*, Academic Press, 2013.

[58] P. Virtanen et al., *SciPy 1.0: fundamental algorithms for scientific computing in Python*, Nat. Methods **17** (2020), 261–272.

[59] H. Honda and T. Nagai, *Mathematical Models of Cell-Based Morphogenesis: Passive and Active Remodeling.*, Springer Nature, Singapore, 2022.

[60] A. G. Fletcher, M. Osterfield, R. E. Baker, and S. Y. Shvartsman, *Vertex Models of Epithelial Morphogenesis*, Biophys. J. **106** (2014), 2291–2304.

[61] J. M. Osborne, A. G. Fletcher, J. M. Pitt-Francis, P. K. Maini, and D. J. Gavaghan, *Comparing individual-based approaches to modelling the self-organization of multicellular tissues*, PLOS Comput. Biol. **13** (2017), e1005387.

[62] A. Buchmann, M. Alber, and J. J. Zartman, *Sizing it up: the mechanical feedback hypothesis of organ growth regulation*, Semin. Cell Dev. Biol. **35** (2014), 73–81.

[63] G. R. Mirams et al., *Chaste: An Open Source C++ Library for Computational Physiology and Biology*, PLOS Comput. Biol. **9** (2013), e1002970.

[64] B. A. Camley and W.-J. Rappel, *Physical models of collective cell motility: from cell to tissue*, J. Phys. Appl. Phys. **50** (2017), 113002.

[65] N. Chen, J. A. Glazier, J. A. Izaguirre, and M. S. Alber, *A parallel implementation of the Cellular Potts Model for simulation of cell-based morphogenesis*, Comput. Phys. Commun. **176** (2007), 670–681.

[66] R. Chaturvedi et al., *On multiscale approaches to three-dimensional modelling of morphogenesis*, J. R. Soc. Interface **2** (2005), 237–253.

[67] J. A. Glazier and F. Graner, *Simulation of the differential adhesion driven rearrangement of biological cells*, Phys. Rev. E Stat. Phys. Plasmas Fluids Relat. Interdiscip. Top. **47** (1993), 2128–2154.

[68] J. A. Izaguirre et al., *CompuCell, a multi-model framework for simulation of morphogenesis*, Bioinforma. Oxf. Engl. **20** (2004), 1129–1137.

[69] Z. Xu, N. Chen, M. M. Kamocka, E. D. Rosen, and M. Alber, *A multiscale model of thrombus development*, J. R. Soc. Interface **5** (2008), 705–722.

[70] S. Okuda, Y. Inoue, and T. Adachi, *Three-dimensional vertex model for simulating multicellular morphogenesis*, Biophys. Physicobiology **12** (2015), 13–20.

[71] M. Osterfield, X. Du, T. Schüpbach, E. Wieschaus, and S. Y. Shvartsman, *Three-dimensional epithelial morphogenesis in the developing Drosophila egg*, Dev. Cell **24** (2013), 400–410.

[72] R. Farhadifar, J.-C. Röper, B. Aigouy, S. Eaton, and F. Jülicher, *The influence of cell mechanics, cell-cell interactions, and proliferation on epithelial packing*, Curr. Biol. CB **17** (2007), 2095–2104.

[73] T. Aegerter-Wilmsen et al., *Integrating force-sensing and signaling pathways in a model for the regulation of wing imaginal disc size*, Dev. Camb. Engl. **139** (2012), 3221–3231.

[74] J. C. Yu and R. Fernandez-Gonzalez, *Quantitative modelling of epithelial morphogenesis: integrating cell mechanics and molecular dynamics*, Semin. Cell Dev. Biol. **67** (2017), 153–160.

[75] D. M. Sussman, *cellGPU: massively parallel simulations of dynamic vertex models*, Comput. Phys. Commun. **219** (2017), 400–406.

[76] T. J. Newman, *Modeling multicellular systems using subcellular elements*, Math. Biosci. Eng. MBE **2** (2005), 613–624.

[77] S. A. Sandersius, M. Chuai, C. J. Weijer, and T. J. Newman, *Correlating Cell Behavior with Tissue Topology in Embryonic Epithelia*, PLOS ONE **6** (2011), e18081.

[78] R. Kubo, *The fluctuation-dissipation theorem*, Rep. Prog. Phys. **29** (1966), no. 255.

[79] T. J. Newman and R. Grima, *Many-body theory of chemotactic cell-cell interactions*, Phys. Rev. E Stat. Nonlin. Soft Matter Phys. **70** (2004), 051916.

[80] S. A. Sandersius, C. J. Weijer, and T. J. Newman, *Emergent cell and tissue dynamics from subcellular modeling of active biomechanical processes*, Phys. Biol. **8** (2011), 045007.

[81] M. Murrell, P. W. Oakes, M. Lenz, and M. L. Gardel, *Forcing cells into shape: the mechanics of actomyosin contractility*, Nat. Rev. Mol. Cell Biol. **16** (2015), 486–498.

[82] K. Tsai and J. Rangel Ambriz, *jenniferrangel/Episcale$_C$rossSectionalView : Episcale$_C$rossSectionalView*, Zenodo https://doi.org/10.5281/zenodo.8045712 (2023).

[83] I. Adam, F. Bagnoli, D. Fanelli, L. Mahadevan, and P. Paoletti, *Prestrain-induced contraction in one-dimensional random elastic chains*, Phys. Rev. E **105** (2022), 065002.

[84] J. W. Freeman and F. H. Silver, *The Effects of Prestrain and Collagen Fibril Alignment on In Vitro Mineralization of Self-Assembled Collagen Fibers*, Connect. Tissue Res. **46** (2005), 107–115.

[85] A. Keller, F. Lanfranconi, and C. M. Aegerter, *The influence of geometry on the elastic properties of the Drosophila wing disc*, Phys. Stat. Mech. Its Appl. **510** (2018), 208–218.

[86] M. Levis et al., *Microfluidics on the fly: Inexpensive rapid fabrication of thermally laminated microfluidic devices for live imaging and multimodal perturbations of multicellular systems.*, Biomicrofluidics **13** (2019), 024111.

[87] R. W. Pryor, *Multiphysics Modeling Using COMSOL®: A First Principles Approach*, (Jones Bartlett Publishers, 2009.

[88] H. Honda and T. Nagai, *Cell models lead to understanding of multi-cellular morphogenesis consisting of successive self-construction of cells*, J. Biochem. (Tokyo) **157** (2015), 129–136.

[89] N. J. Popławski, M. Swat, J. S. Gens, and J. A. Glazier, *Adhesion between cells, diffusion of growth factors, and elasticity of the AER produce the paddle shape of the chick limb*, Phys. A **373** (2007), 521–532.

[90] F. Graner and J. A. Glazier, *Simulation of biological cell sorting using a two-dimensional extended Potts model*, Phys. Rev. Lett. **69** (1992), 2013–2016.

[91] T. Nagai and H. Honda, *Computer simulation of wound closure in epithelial tissues: cell basal-lamina adhesion*, Phys. Rev. E Stat. Nonlin. Soft Matter Phys. **80** (2009), 061903.

[92] T. Nagai, H. Honda, and M. Takemura, *Simulation of Cell Patterning Triggered by Cell Death and Differential Adhesion in Drosophila Wing*, Biophys. J **114** (2018), 958–967.

[93] R. Smallwood, *Computational modeling of epithelial tissues*, WIREs Syst. Biol. Med. **1** (2009), 191–201.

[94] M. Rauzi, A. Hočevar Brezavšček, P. Ziherl, and M. Leptin, *Physical Models of Mesoderm Invagination in Drosophila Embryo*, Biophys. J **105** (2013), 3–10.

[95] A. Micoulet, J. P. Spatz, and A. Ott, *Mechanical response analysis and power generation by single-cell stretching*, Chemphyschem Eur. J. Chem. Phys. Phys. Chem. **6** (2005), 663–670.

[96] T. G. Kuznetsova, M. N. Starodubtseva, N. I. Yegorenkov, S. A. Chizhik, and R. I. Zhdanov, *Atomic force microscopy probing of cell elasticity*, Micron Oxf. Engl. 1993 **38** (2007), 824–833.

[97] Laurent et al. V. M., *Gradient of Rigidity in the Lamellipodia of Migrating Cells Revealed by Atomic Force Microscopy*, Biophys. J. **89** (2005), 667–675.

[98] J. Y. Sim et al., *Spatial distribution of cell-cell and cell-ECM adhesions regulates force balance while maintaining E-cadherin molecular tension in cell pairs*, Mol. Biol. Cell **26** (2015), 2456–2465.

[99] Y.-S. Chu et al., *Force measurements in E-cadherin–mediated cell doublets reveal rapid adhesion strengthened by actin cytoskeleton remodeling through Rac and Cdc42.*, J. Cell Biol. **167** (2004), 1183–1194.

[100] S. Marino, I. B. Hogue, C. J. Ray, and D. E. Kirschner, *A methodology for performing global uncertainty and sensitivity analysis in systems biology*, J. Theor. Biol. **254** (2008), 178–196.

[101] E. Fazeli et al., *Automated cell tracking using StarDist and TrackMate*, F1000Research **9** (2020), no. 1279.

[102] M. Marin-Riera, M. Brun-Usan, R. Zimm, T. Välikangas, and I. Salazar-Ciudad, *Computational modeling of development by epithelia, mesenchyme and their interactions: aunified model*, Bioinformatics **32** (2016), 219–225.

[103] I. V. Pivkin and G. E. Karniadakis, *Accurate coarse-grained modeling of red blood cells*, Phys. Rev. Lett. **101** (2008), 118105.

[104] F. Ioannou, M. A. Dawi, R. J. Tetley, Y. Mao, and J. J. Muñoz, *Development of a New 3D Hybrid Model for Epithelia Morphogenesis*, Front. Bioeng. Biotechnol. **8** (2020).

[105] A. J. Hughes et al., *Engineered Tissue Folding by Mechanical Compaction of the Mesenchyme*, Dev. Cell **44** (2018), 165–178.e6.

[106] C. Zmurchok, D. Bhaskar, and L. Edelstein-Keshet, *Coupling mechanical tension and GTPase signaling to generate cell and tissue dynamics*, Phys. Biol. **15** (2018), 046004.

[107] The MathWorks Inc., *MATLAB 9.9 (2020b)*, Natick Mass (2020).

[108] O. Kramer, *Scikit-Learn. in Machine Learning for Evolution Strategies (ed. Kramer, O.)*, Springer International Publishing, Cham, 2016.

[109] D. C. Montgomery, G. C. Runger, and N. F. Hubele, *Book Title*, Wiley, 2007.

[110] R. M. Bethea, B. S. Duran, and T. L. Boullion, *Statistical Methods for Engineers and Scientists*, (M. Dekker, 1975.

[111] J. Schindelin et al., *Fiji: an open-source platform for biological-image analysis*, Nat. Methods **9** (2012), 676–682.

[112] Y. Mao et al., *Differential proliferation rates generate patterns of mechanical tension that orient tissue growth*, EMBO J. **32** (2013), 2790–2803.

[113] J. B. Duffy, *GAL4 system in drosophila: A fly geneticist's swiss army knife*, genesis **34** (2002), 1–15.

[114] K. Kimura et al., *Regulation of myosin phosphatase by Rho and Rho-associated kinase (Rho-kinase)*, Science **273** (1996), 245–248.

[115] Eisenhoffer et al. G. T., *Crowding induces live cell extrusion to maintain homeostatic cell numbers in epithelia*, Nature **484** (2012), 546–549.

[116] E. Marinari et al., *Live-cell delamination counterbalances epithelial growth to limit tissue overcrowding*, Nature **484** (2012), 542–545.

[117] S. Ohsawa, J. Vaughen, and T. Igaki, *Cell Extrusion: A Stress-Responsive Force for Good or Evil in Epithelial Homeostasis.*, Dev. Cell **44** (2018), 284–296.

[118] R. Fernandez-Gonzalez and J. A. Zallen, *Feeling the Squeeze: Live-Cell Extrusion Limits Cell Density in Epithelia*, Cell **149** (2012), 965–967.

[119] S.A. Gudipaty et al., *Mechanical stretch triggers rapid epithelial cell division through Piezo1*, Nature **543** (2017), 118–121.

[120] A. Munjal, J.-M. Philippe, E. Munro, and T. Lecuit, *A self-organized biomechanical network drives shape changes during tissue morphogenesis*, Nature **524** (2015), 351–355.

[121] G. Bradski and A. Kaehler, *OpenCV*, Dr. Dobb's journal of software tools (2000).

[122] H. Prautzsch, W. Boehm, and M. Paluszny, *Bézier and B-Spline Techniques*, Springer BerlinHeidelberg, Berlin, Heidelberg, 2002.

[123] H. Mary and G. J. Brouhard, *Kappa (κ): Analysis of Curvature in Biological Image Data using B-splines* **14**.

[124] E. Bisong, *Matplotlib and Seaborn. in Building Machine Learning and Deep Learning Models on Google Cloud Platform: A Comprehensive Guide for Beginners (ed. Bisong, E.)*, Apress, Berkely, CA, 2019.

[125] G. H. Koenderink and E. K. Paluch, *Architecture shapes contractility in actomyosin networks*, Curr. Opin. Cell Biol. **50** (2018), 79–85.

[126] A. Munjal and T. Lecuit, *Actomyosin networks and tissue morphogenesis*, Development **141** (2014), no. 9, 1789–1793.

[127] L. Sui, S. Alt, and M. Weigert et al., *Differential lateral and basal tension drive folding of Drosophila wing discs through two distinct mechanisms*, Nat. Commun. **9** (2018), no. 4620.

[128] P. Agarwal and R. Zaidel-Bar, *Principles of Actomyosin Regulation In Vivo*, Trends in Cell Biology **29** (2019), no. 2, 150–163.

[129] I. Chandrasekar et al., *Nonmuscle myosin II is a critical regulator of clathrin-mediated endocytosis*, Traffic **15** (2014), 418–432.

[130] V. Ruprecht et al., *Cortical contractility triggers a stochastic switch to fast amoeboid cell motility*, Cell **160** (2015), 673–685.

[131] Y. J. Liu et al., *Confinement and low adhesion induce fast amoeboid migration of slow mesenchymal cells*, Cell **160** (2015), 659–672.

[132] A. A. Anlas and C. M. Nelson, *Tissue mechanics regulates form, function, and dysfunction*, Curr. Opin. Cell Biol. **54** (2018), 98–105.

[133] N. C. Heer and A. C. Martin, *Tension, contraction and tissue morphogenesis*, Development **144** (2017), 4249–4260.

[134] M. L. Gardel, I. C. Schneider, Y. Aratyn-Schaus, and C. M. Waterman, *Mechanical integration of actin and adhesion dynamics in cell migration*, Annu. Rev. Cell Dev. Biol. **26** (2010), 315–333.

[135] M. Vicente-Manzanares, X. Ma, R. S. Adelstein, and A. R. Horwitz, *Non-muscle myosin II takes centre stage in cell adhesion and migration*, Nat. Rev. Mol. Cell Biol. **10** (2009), 778–790.

[136] G. Salbreux, G. Charras, and E. Paluch, *Actin cortex mechanics and cellular morphogenesis.*, Trends Cell Biol. **10** (2012), 536–545.

[137] M. J. Siedlik and C. M. Nelson, *Regulation of tissue morphodynamics: an important role for actomyosin contractility*, Curr. Opin. Genet. Dev. **32** (2015), 80–85.

[138] C. Norden, *Pseudostratified epithelia – cell biology, diversity and roles in organ formation at a glance*, J. Cell Sci. **130** (2017), no. 11, 1859–1863.

[139] H. Kang, M. J. Bradley, B. R. McCullough, A. Pierre, E. E. Grintsevich, E. Reisler, and E. M. De La Cruz, *Identification of cation-binding sites on actin that drive polymerization and modulate bending stiffness*, PNAS **109** (2012), no. 42, 16923–16927.

[140] L. Blanchoin, R. Boujemaa-Paterski, C. Sykes, and J. Plastino, *Actin dynamics, architecture, and mechanics in cell motility*, Physiol. Rev. **94** (2014), no. 1, 235–263.

[141] H. Lodish, A. Berk, P. Matsudaira, C. A. Kaiser, M. Krieger, M. P. Scott, L. Zipursky, and J. Darnell, *Molecular Cell Biology, 5th edn.*, W. H. Freeman and Company, New York, NY., 2003.

[142] L. Artman, V. Dormoy-Raclet, C. von Roretz, and I. E. Gallouzi, *Planning your every move: the role of β-actin and its post-transcriptional regulation in cell motility*, Semin. Cell Dev. Biol. **34** (2014), 33–43.

[143] M. A. Hartman and J. A. Spudich, *The myosin superfamily at a glance*, J. Cell Sci. **125** (2012), no. 7, 1627–1632.

[144] F. Matsumura, *Regulation of myosin II during cytokinesis in higher eukaryotes*, Trends Cell Biol. **15** (2005), no. 7, 371–377.

[145] H. Miao and J. T. Blankenship, *The pulse of morphogenesis: actomyosin dynamics and regulation in epithelia*, Development **147** (2020), no. 17.

[146] M. Ikebe and D. J. Hartshorne, *Phosphorylation of smooth muscle myosin at two distinct sites by myosin light chain kinase*, J. Biol. Chem. **260** (1985), no. 18.

[147] M. Amano, M. Ito, K. Kimura, Y. Fukata, K. Chihara, T. Nakano, Y. Matsuura, and K. Kaibuchi, *Phosphorylation and activation of myosin by Rho-associated kinase (Rho-kinase)*, J. Biol. Chem. **271** (1996), no. 34, 20246–20249.

[148] G. Totsukawa, Y. Yamakita, S. Yamashiro, D. J. Hartshorne, Y. Sasaki, and F. Matsumura, *Distinct roles of ROCK (Rho-kinase) and MLCK in spatial regulation of MLC phosphorylation for assembly of stress fibers and focal adhesions in 3T3 fibroblasts*, J. Cell Biol. **150** (2000), no. 4, 797–806.

[149] I. Tan, J. Yong, J. M. Dong, L. Lim, and T. Leung, *A tripartite complex containing MRCK modulates lamellar actomyosin retrograde flow*, Cell **135** (2008), no. 1, 123–136.

[150] R. Levayer and T. Lecuit, *Biomechanical regulation of contractility: spatial control and dynamics*, Trends Cell Biol. **22** (2012), no. 2, 61–81.

[151] J. Walklate, Z. Ujfalusi, and M. A. Geeves, *Myosin isoforms and the mechanochemical cross-bridge cycle*, J. Exp. Biol. **219** (2016), no. 2, 168–174.

[152] V. Wollrab, J. M. Belmonte, L. Baldauf, M. Leptin, F. Nédeléc, and G. H. Koenderink, *Polarity sorting drives remodeling of actin-myosin networks*, J. Cell Sci. **132** (2019), no. 4.

[153] S. Stam, S. L. Freedman, S. Banerjee, K. L. Weirich, A. R. Dinner, and M. L. Gardel, *Filament rigidity and connectivity tune the deformation modes of active biopolymer networks*, PNAS **114** (2017), no. 47.

[154] P. Chugh, A. G. Clark, M. B. Smith, D. A. D. Cassani, K. Dierkes, A. Ragab, P. P. Roux, G. Charras, G. Salbreux, and E. K. Paluch, *Actin cortex architecture regulates cell surface tension*, Nat. Cell Biol. **19** (2017), 689–697.

[155] W. Y. Ding, H. T. Ong, Y. Hara, J. Wongsantichon, Y. Toyama, R. C. Robinson, F. Nedelec, and R. Zaidel-Bar, *Plastin increases cortical connectivity to facilitate robust polarization and timely cytokinesis*, J. Cell Biol. **216** (2017), 1371–1386.

[156] M. Gautel and K. Djinović-Carugo, *The sarcomeric cytoskeleton: from molecules to motion*, J. Exp. Biol. **219** (2016), no. 2, 135–145.

[157] M. P. Murrell and M. L. Gardel, *F-actin buckling coordinates contractility and severing in a biomimetic actomyosin cortex*, Proc. Natl Acad. Sci. **51** (2012), 20820–20825.

[158] L. W. Janson, J. Kolega, and D. L. Taylor, *Modulation of contraction by gelation/solation in a reconstituted motile model*, J. Cell Biol. **114** (1991), 1005–1015.

[159] P. M . Bendix et al., *A quantitative analysis of contractility in active cytoskeletal protein networks*, Biophys. J. **94** (2008), 3126–3136.

[160] X. Qin et al., *Cell-matrix adhesion and cell-cell adhesion differentially control basal myosin oscillation and Drosophila egg chamber elongation*, Nat. Commun. **8** (2017).

[161] C. Norden, S. Young, B. A. Link, and W. A. Harris, *Actomyosin is the main driver of interkinetic nuclear migration in the retina*, Cell **138** (2009), no. 6, 1195–1208.

[162] A. Badugu and A. Käch, *Cytoplasmic flows caused by actomyosin contraction drive interkinetic nuclear migration*, bioRxiv (2020).

[163] S. Britton, O. Kim, F. Pancaldi, Z. Xu, R. I. Litvinov, J. W. Weisel, and M. Alber, *Contribution of nascent cohesive fiber-fiber interactions to the non-linear elasticity of fibrin networks under tensile load*, Acta Biomater. **94** (2019), 514–523.

[164] C. Michael, F. Pancaldi, and S. Britton et al., *Combined computational modeling and experimental study of the biomechanical mechanisms of platelet-driven contraction of fibrin clots*, Commun. Biol. **6** (2023), no. 869.

[165] D. Laporte, N. Ojkic, D. Vavylonis, and J. Q. Wu, *α-Actinin and fimbrin cooperate with myosin II to organize actomyosin bundles during contractile-ring assembly*, Mol. Biol. Cell **23** (2012), no. 16, 3094–3110.

[166] H. Tang, D. Laporte, and D. Vavylonis, *Actin cable distribution and dynamics arising from cross-linking, motor pulling, and filament turnover*, Mol. Biol. Cell **25** (2014), no. 19, 3006–3016.

[167] B. Lee, X. Zhou, K. Riching, K. W. Eliceiri, P. J. Keely, S. A. Guelcher, A. M. Weaver, and Y. Jiang, *A three-dimensional computational model of collagen network mechanics*, PLoS One **9** (2014), no. 11.

[168] M. C. Kim, J. Whisler, Y. R. Silberberg, R. D. Kamm, and H. H. Asada, *Cell Invasion Dynamics into a Three Dimensional Extracellular Matrix Fibre Network*, PLoS Comput. Biol. **11** (2015), no. 10.

[169] M. Christian, M. Banwarth-Kuhn, K. Rodriguez, C. K. Ta, A. Roy-Chowdhury, W. Chen, G. Venugopala Reddy, and A. Mark, *Role of turgor-pressure induced boundary tension in the maintenance of the shoot apical meristem of Arabidopsis thaliana*, J. R. Soc. Interface **20** (2023), no. 203.

[170] J. M. Belmonte, M. Leptin, and F. Nédélec, *A theory that predicts behaviors of disordered cytoskeletal networks*, Mol. Syst. Biol. **13** (2017), no. 9.

[171] C. J. Miller, D. Harris, R. Weaver, G. B. Ermentrout, and L. A. Davidson, *Emergent mechanics of actomyosin drive punctuated contractions and shape network morphology in the cell cortex*, PLoS Comput. Biol. **14** (2018), no. 9.

[172] J. F. Fuhrmann et al., *Active shape programming drives Drosophila wing disc eversion*, Sci. Adv. **10** (1776), no. 32.

[173] S. Eaton, P. Auvinen, L. Luo, Y. N. Jan, and K. Simons, *CDC42 and Rac1 control different actin-dependent processes in the Drosophila wing disc epithelium*, J. Cell Biol. **131** (1995), no. 1, 151–164.

[174] T. J. Widmann and C. Dahmann, *Wingless signaling and the control of cell shape in Drosophila wing imaginal discs*, Journal (use abbreviations if appropriate **334** (2009), no. 1, 161–173.

[175] D. Oelz and A. Mogilner, *Actomyosin contraction, aggregation and traveling waves in a treadmilling actin array*, Physica D. (2016), 70–83.

[176] I. Linsmeier, S. Banerjee, and P. Oakes et al., *Disordered actomyosin networks are sufficient to produce cooperative and telescopic contractility*, Nat. Commun. **7** (2016), no. 12615.

[177] J. P. S. Ferreira, M. P. L. Parente, and R. M. Natal Jorge, *Continuum mechanical model for cross-linked actin networks with contractile bundles*, Journal of the Mechanics and Physics of Solids **110** (2018), 100–117.

[178] W. Mirza, M. De Corato, M. Pensalfini, G. Vilanova, A. Torres-Sànchez, and A. Marino, *Theory of active self-organization of dense nematic structures in the actin cytoskeleton*, eLife **13** (2024).

[179] D. Gordon, A. Bernheim-Groswasser, C. Keasar, and O. Farago, *Hierarchical self-organization of cytoskeletal active networks*, Phys. Biol. **9** (2012).

[180] S. L. Freedman, S. Banerjee, G. M. Hocky, and A. R. Dinner, *A Versatile Framework for Simulating the Dynamic Mechanical Structure of Cytoskeletal Networks*, Biophysical Journal **113** (2017), no. 2, 448–460.

[181] K. Popov, J. Komianos, and G. A. Papoian, *MEDYAN: Mechanochemical Simulations of Contraction and Polarity Alignment in Actomyosin Networks*, PLoS Comput. Biol. **12** (2016), no. 4.

[182] M. V. Ciocanel, A. Chandrasekaran, C. Mager, Q. Ni, G. A. Papoian, and A. Dawes, *Simulated actin reorganization mediated by motor proteins*, PLoS Comput Biol. **18** (2022), no. 4.

[183] Q. Ni, K. Wagh, A. Pathni, H. Ni, V. Vashisht, A. Upadhyaya, and G. A. Papoian, *A tug of war between filament treadmilling and myosin induced contractility generates actin rings*, eLife **11** (2022).

[184] F. Nedelec and D. Foethke, *Collective Langevin dynamics of flexible cytoskeletal fibers*, New J. Phys. **9** (2007), no. 427.

[185] W. Jung, A. P. Tabatabai, J. J. Thomas, S. M. A. Tabei, M. P. Murrell, and T. Kim, *Dynamic motions of molecular motors in the actin cytoskeleton*, Cytoskeleton **76** (2019), 517–531.

A

Appendix - Chapter 2

A.1 Preface

The content of this Appendix is a reproduction of the Supplementary Information file of our published paper presented in Chapter 2 [1]. All of the experiments and analyses of the experimental data presented in this Appendix were performed by Nilay Kumar and members of Dr. Zartman's lab. All of the simulations and corresponding analyses were done by me. Sections associated with the model were mainly written by me with the guidance and help of Dr. Mark Alber, Dr. Weitao Chen, and Dr. Kevin Tsai.

A.2 Supplemental Details of Methods and Image Analysis

A.2.1 Additional Method Details for Fig 2.3

Drosophila wing imaginal discs belonging to varying stages of larval development were dissected, fixed, and stained with Phalloidin and DAPI to mark Actin and nuclei, respectively (Fig 2.3 A). Principally, cross-sections along the AP axis were analyzed (Fig 2.3 B). An in-house pipeline for quantifying local basal curvature (κ_{basal}) (Appendix A subsection "Quantification of Local Basal Curvature") and tissue height (H) (Appendix A subsection "Quantification of Morphological and Signaling-Related Features from the Wing Imaginal

Discs") was used to measure shape changes as the disc ages. For each stage, κ_{basal} was quantified for samples whose number has been indicated as an inset within the plot (Fig 2.3 C, top panel). The average κ_{basal} is plotted against the distance of the point of calculation from the center of the disc (ℓ). This is further normalized using half of the length of the basal surface (L_{AP}) along the AP axis. The standard deviation in prediction of κ_{basal} is shown as the shaded region within the plots. A similar analysis for H was performed, as shown in Fig 2.3 C (bottom panel).

Drosophila wing imaginal discs belonging to varying stages of larval development were dissected, and antibody staining of pMyoII and βPS, respectively, were carried out to measure the spatiotemporal dynamics of cytoskeletal regulation within the developing epithelia (Fig 2.3 D, D'). First, we analyzed how the ratio of apical to basal levels of pMyoII ($\text{pMyoII}_{\text{apical}}$ / $\text{pMyoII}_{\text{basal}}$) varies across the pouch medial and lateral domains (Fig 2.3 E). The pouch was discretized into 90 regional cells as described in Appendix A subsection "Quantification of Morphological and Signaling-Related Features from the Wing Imaginal Discs". The middle 30 cells constitute the medial domain, while the remaining 60 cells on the anterior/posterior ends constitute the lateral ends of the pouch. Then, the difference between the average of $\text{pMyoII}_{\text{apical}}$ / $\text{pMyoII}_{\text{basal}}$ across the pouch medial (M) and lateral (L) domains was computed and normalized by the average value of $\text{pMyoII}_{\text{apical}}$ / $\text{pMyoII}_{\text{basal}}$ in the pouch lateral (L) domain. This quantity was calculated for multiple discs (sample sizes indicated in the inset of the plot) belonging to different stages of development (72-96 h AEL). Next, a box plot was used to visualize the variation of this ratio $((\text{X}_\text{M} - \text{X}_\text{L})/\text{X}_\text{L}$ where X represents $\text{pMyoII}_{\text{apical}}$ / $\text{pMyoII}_{\text{basal}}$) across different stages of wing disc development (Fig 2.3 E). Since βPS is primarily localized in the pouch basal surface, an in-house pipeline (Appendix A subsection "Quantification of Morphological and Signaling-Related Features from the Wing Imaginal Discs") was used to quantify the expression of βPS across the basal surface of the AP axis. The data was then exported to MATLAB [107] where the AP axis was split into three equal parts and at each of these sections, the averaged βPS fluorescence was evaluated. Next, we used these averaged values to compute the difference of βPS in

the medial to lateral domain of the pouch ($\beta\text{PS}_{\text{medial}}$ / $\beta\text{PS}_{\text{lateral}}$). The difference is further normalized by $\beta\text{PS}_{\text{lateral}}$. The ratio is next plotted for multiple samples belonging to different stages of development as a box plot (Fig 2.3 E').

Using the same pipeline (Appendix A subsection "Quantification of Morphological and Signaling-Related Features from the Wing Imaginal Discs"), we calculated the fluorescence intensity of Actin, pMyoII and βPS for discs stained with the aforementioned cytoskeletal regulators. We plotted the values of Actin, pMyoII and βPS for multiple samples belonging to 72 and 96 h AEL larval stages of development (Fig 2.3 F, F'). A straight line was fit, and the R^2 value was calculated to measure the correlation strength. We first fit straight lines (color-coded) to the correlations for individual samples. We also fit a line to the aggregated data to measure the global correlation.

We also used the image analysis pipeline (Appendix A subsection "Quantification of Morphological and Signaling-Related Features from the Wing Imaginal Discs") on discs belonging to different stages of development for quantifying correlations between the ratio of $\text{pMyoII}_{\text{apical}}$ to $\text{pMyoII}_{\text{basal}}$ and local tissue height (H). A 2D scatter plot was first plotted with the x-axis and y-axis representing $\text{pMyoII}_{\text{apical}}$ / $\text{pMyoII}_{\text{basal}}$ and H, respectively (Fig 2.3 G, G'). Data extracted from each sample was plotted using unique colors. First, linear regression models were fitted individually to points extracted from each sample using scikit-learn. A solid color-coded line represents the predictions made by the model. Next, a single linear model was fit to the aggregated data from different samples represented by a solid black colored line. Averaged R^2 values for sample-wise model fits, along with the R^2 value of the global model fit, have been reported. A p-value for an F-test was calculated to evaluate the statistical significance of the global fit. Plotting and statistical tests were carried out in Python.

Lastly, we used our in-house codes (Appendix A subsections "Quantification of Local Basal Curvature" and "Quantification of Morphological and Signaling-Related Features from the Wing Imaginal Discs") to calculate the correlation between basal βPS localization and κ_{basal} (Fig 2.3 H, H'). A scatter plot was used to plot the variation of κ_{basal} with changes

in βPS for multiple discs belonging to two different stages of development. Points were color-coded based on their position along the pouch AP axis (medial: blue or lateral: red). Two straight lines were fit to study the correlation between βPS and κ_{basal} specific to pouch medial and lateral domains, and the corresponding domain-specific R^2 values have been indicated as an inset within the plots.

A.2.2 Additional Method Details for Fig 2.4

An in-house pipeline (Appendix A subsection "Quantification of Local Basal Curvature") was used to quantify the basal curvature (κ_{basal}) for multiple discs belonging to 72 and 96 h AEL of larval development (Fig 2.4 A", B"). The solid line indicates the averaged κ_{basal} value for multiple discs, while the shaded area indicates the standard deviation in prediction. The AP axis was further subdivided into three equal regions based on the overall length of the basal surface. The middle region corresponds to the medial domain, while the remaining two regions correspond to the lateral domains. Next, we calculated the ratio of the average curvature in the lateral ends to the medial domain ($\bar{\kappa}_{basal,lateral}/\bar{\kappa}_{basal,medial}$, Fig 2.4 D-ii). This ratio was computed over multiple discs whose average value was plotted as a bar graph. The ratio for individual samples is plotted as a scatter plot overlaid over the bar. Further, we use the same pipeline to calculate the same ratio ($\bar{\kappa}_{basal,lateral}/\bar{\kappa}_{basal,medial}$) for the simulation test cases that have been plotted as a bar graph on the right of the experimental data (Fig 2.4 D-ii).

For Fig 2.4 F-I, fluorescent intensities along the apical, basal, or lateral cell sides were plotted against the distance of the point from the center of the pouch. It was further normalized by averaging the overall length of the measured axis. Averaged fluorescence intensities and the standard deviation in prediction were plotted to visualize the spatial patterning. Analysis of several samples belonging to multiple stages of development shows temporal changes in spatial patterning of cytoskeletal regulators along the AP axis. Detailed steps for image normalization and intensity quantification can be found in Appendix A

subsection "Quantification of Morphological and Signaling-Related Features from the Wing Imaginal Discs".

A.2.3 Additional Method Details for Fig 2.5

To downregulate βPS expression, the GAL4/UAS [113] system was used to express an RNAi against *mys*, a beta subunit of the integrin dimer. The MS1096- Gal4 driver was used to drive the expression of mys^{RNAi} spatially, leading to more βPS inhibition in the dorsal compartment than the ventral side of the wing imaginal disc. A βPS antibody staining was carried out to validate the mutation. DAPI and Phalloidin dyes were used to visualize changes in cell shape (Actin) and nuclear positioning (Nuclei). Cross sections along the indicated DV axis were analyzed for these genetic perturbations (Fig 2.5 B, B').

We also used an MS1096-Gal4 driver to knock down Rho1 expression in the dorsal compartment of the wing disc with a commercially available UAS-$\mathrm{Rho1}^{\mathrm{RNAI}}$ line. DAPI and Phalloidin dyes labeled the nuclei and Actin, respectively. The cross-section along the DV axis was analyzed (Fig 2.5 C, C'). We also looked into how perturbations in βPS and Rho1 expression affect pMyoII. The details for these perturbations can be found in text corresponding to Appendix A Fig A.11.

An in-house MATLAB [107] code (Appendix A subsection "Quantification of Morphological and Signaling-Related Features from the Wing Imaginal Discs") was used to calculate the average height of cells for dorsal and ventral compartments of the cross-sections analyzed. Differences between the average height of dorsal and ventral compartments (ΔH) was computed and then normalized by the average height of the lateral compartment ($H_{Lateral}$) for multiple samples across all the genetic perturbations analyzed (Figure 2.5 D, D').

A.2.4 Additional Method Details for Fig 2.6

Unless otherwise indicated, cross sections along the AP axis for wing imaginal discs belonging to 72 h and 96 h AEL larval stages were analyzed. The proximity of nuclei with respect to the basal surface ($\bar{d}_B$) has been defined as the ratio of the distance of nuclei from the basal

surface (d_B) over the sum of the distances of nuclei from apical (d_A) and basal surfaces (d_B). Details about the quantification pipeline are mentioned in Appendix A subsection "Quantification of Nuclear Positioning" (Appendix A Fig A.25). As described in previous sections, the cross-section was subdivided into three regions, i.e., one medial and two lateral regions. Nuclei in each subregion were identified, and their proximity to the basal surface was calculated. We then calculated the average ($\bar{d}_B$) value for nuclei belonging to the different subregions. We use the ratio of average ($\bar{d}_B$) in the medial to lateral regions of the wing disc as a metric of comparison with results obtained using the computational model. The average value of this ratio calculated over multiple samples for discs belonging to 72 h and 96 h AEL larval stage of development has been plotted as a bar graph (Fig 2.6 B). The data from individual samples has been plotted as a scatter plot overlaid over the bar graph.

We also used an MS1096-Gal4 driver to express UAS-mys$^{\mathrm{RNAi}}$to knock down βPS predominantly in the dorsal compartment of the wing disc (Fig 2.6 D). The disc was additionally stained with βPS antibody to validate the mutations. The nuclei for the mutant have been color-coded with their relative distance from the basal surface of the pouch ($\bar{d}_B$). Details about the quantification pipeline for nuclear positioning can be found in Appendix A subsection "Quantification of Nuclear Positioning".

A.2.5 Additional Method Details for Fig 2.8

The GAL4/UAS [113] system was used to express dominant negative form of insulin receptors (InsR$^{\mathrm{DN}}$) in the posterior compartment of the wing imaginal disc using an engrailed-Gal4 driver (Fig 2.8 A-ii, B-ii, ii'). The engrailed-Gal4 also expresses a UAS-GFP marker to fluorescently label the posterior half, i.e., the region of perturbation. The parental engrailed-Gal4 driver was used as a control in addition to the internal control (Fig 2.8 A-i, B i-i'). Wing imaginal discs belonging to 100-120 h AEL (wandering larvae, early 3$^{\mathrm{rd}}$ instar) were dissected and fixed. The AP axis of the pouch was analyzed for these genetic perturbations. For both control and mutant samples, κ_{basal} was quantified using the in-house pipeline described in Appendix A subsection "Quantification of Local Basal Curvature" (Fig 2.8 C-i). The average

basal curvature (κ_{basal}) along with the standard error in mean have been plotted for points sampled on the basal surface. The x-axis indicates the normalized distance of the point from the pouch center (ℓ/L_{AP}). The normalization was carried out by dividing the distance by half of the length of the basal surface (L_{AP}). A student t-test was used to compare the average curvature profiles for control (en Gal4) and disc expressing en>InsR$^{\mathrm{DN}}$ samples in the anterior and posterior compartments respectively. The t-statistic (t), along with the p-value (p) for the test have been indicated on the top panels of the plot. Further, a Cohen's d (d) has also been indicated to measure the effect of sample sizes in statistical analysis. We also used our in-house pipeline to calculate the average height of the anterior ($\mathrm{H_{Anterior}}$) and posterior ($\mathrm{H_{Posterior}}$) compartments of the control (en-Gal4) and perturbed (en>InsR$^{\mathrm{DN}}$) samples. We next calculated the difference between $\mathrm{H_{Anterior}}$ and $\mathrm{H_{Posterior}}$ and normalized it by $\mathrm{H_{Anterior}}$. The quantity was calculated for multiple samples and has been visualized as a box plot (Fig 2.8 C-ii). A student t-test was used to compare the average curvature profiles for control (en-Gal4) and disc expressing en>InsR$^{\mathrm{DN}}$ samples ($^{***}: p < 0.001$, $^{**}: 0.001 < p < 0.01$, $^{*}: 0.01 < p < 0.05$). Furthermore, antibody staining for βPS (Fig 2.8 B ii-ii'), Rho1 (Fig 2.8 D, D') and pMyoII (Fig 2.8 E, E') were carried out to measure changes in cytoskeletal regulation. We then calculated the difference in average fluorescence levels of the protein studied between the posterior and anterior compartments. Once this difference was computed, it was normalized by the average fluorescence of the anterior compartment for both the Gal4 control and genetically perturbed en>InsR$^{\mathrm{DN}}$ samples (Fig 2.8 F i-iii). Statistical significance of the differences between the control and mutant group were assessed using a t-test ($^{***}: p < 0.001$, $^{**}: 0.001 < p < 0.01$, $^{*}: 0.01 < p < 0.05$).

We expressed the constitutively active form of InsR (InsR$^{\mathrm{CA}}$) in the whole wing imaginal disc using a nubbin-Gal4 driver (Semi AP axis cross section visualized in Fig 2.8 G'). The progeny was grown at 18°C as it was lethal at 25°C. The control for this experiment were the wing discs belonging to the parental nubbin-Gal4 driver grown at 18°C (Fig 2.8 G). Expression of InsR$^{\mathrm{CA}}$ caused a substantial increase in tissue size along with an increase in proliferation. Since the whole pouch was out of the sensor area of the microscope, we

imaged half of the disc at a time (medial to anterior and medial to posterior) (Fig 2.8 G, G'). The discs were stained with βPS to measure cell shape changes. Half of the DV section at a time was analyzed for both control and mutant cases (Fig 2.8 G-H). Quantification of κ_{basal} (Fig 2.8 H i) and H (Fig 2.8 H ii) was carried out as described in the previous paragraph of this section.

GAL4/UAS system was used to express the constitutively active form of Dpp receptors, Thickveins (Tkv), in the posterior compartment of the wing imaginal disc using an en-Gal4 driver (Fig 2.8 I). Samples dissected from 100-120 h AEL (physiological stage: wandering 3rd instar larvae) were fixed. DAPI was used to label the nuclei. A PMAD antibody staining was performed to validate the UAS-Tkv^{CA} line (Appendix A Fig A.18 C, C'). A βPS (Fig 2.8 I) and pMyoII (Fig 2.8 J) antibody staining was also carried out to measure changes in cytoskeletal regulation and tissue geometry. The cross-section along the AP axis was analyzed for the genetic perturbations.

We also used the en-Gal4 driver to overexpress Myc [42], a transcription factor contributing towards cell growth, in the posterior compartment of the wing imaginal disc (Fig 2.8 K). Wing imaginal discs belonging to 100-120 h AEL were physiologically staged. Wandering 3rd instar larvae were dissected, and the wing imaginal disc was fixed. A βPS and pMyoII antibody staining was carried out to measure changes in tissue shape while DAPI was used to label nuclei (Fig. 2.8 K, L). Cross sections along the AP axis were analyzed for the genetic perturbations. For both of the genetic perturbations, quantification of κ_{basal} (Fig 2.8 M) and fluorescence intensities of cytoskeletal regulators (Fig 2.8 N, O) were carried out as described in the first paragraph of this section. Additional methods for quantification of basal curvature, tissue height, and expression of cytoskeletal regulators from the imaging data can be found in Appendix A section A.1 of the text.

A.3 Supplementary Results and Figures

A.3.1 Integrin (βPS) and Collagen IV (ColIV) Co-Localize With Actin Within the Cortical Region of a Dividing Cell.

Wing imaginal disc belonging to early 3rd instar larval stage of development was dissected and fixed. A phosphohistone H3 (PH3) and a β-Integrin (βPS) antibody staining were carried out to measure the expression of integrins around the dividing cell. Based on the PH3 and nuclei markers (DAPI), cells belonging to different stages of division undergoing interkinetic nuclear migration were selected (Fig A.1 A). Optical cross-sections along the division axis were analyzed. It can be seen that βPS is initially localized near the filamentous actin tail of the dividing nuclei. As the nuclei move towards the apical surface for division, its accumulation near the cell cortical region increases. Finally, when the cell has divided βPS localizes more towards the boundary of the daughter cells.

Wing imaginal discs from the early 3rd instar larval stage were dissected and fixed. DAPI and Phalloidin were used to label the nuclei and Actin, respectively (Fig A.1 B). An antibody staining against anti-Collagen IV was carried out to visualize spatial patterning of Collagen IV (ColIV) within the fixed tissue. Based on the data from Actin and nuclei fluorescence channels, a couple of representative mitotic nuclei were selected within the pouch (Fig A.1 B). An optical slice along the long axis of the dividing cells was taken to have a lateral perspective of ColIV during mitosis (Fig A.1 B-ii). A major highlight of a dividing cell is the presence of higher levels of Actin around the cortical region of a dividing cell [109]. Along with Actin and Integrin (Fig A.1 A), ColIV (Fig A.1 B-ii) also colocalizes at the cortical region of the dividing cell.

A.3.2 The Wing Imaginal Disc is Flat Across the AP Axis at Earlier Stages of Development (<72h AEL)

Wing imaginal discs belonging to earlier stages of development were dissected and fixed. An antibody staining against Actin, pMyoII and βPS was carried out to study cytoskeletal

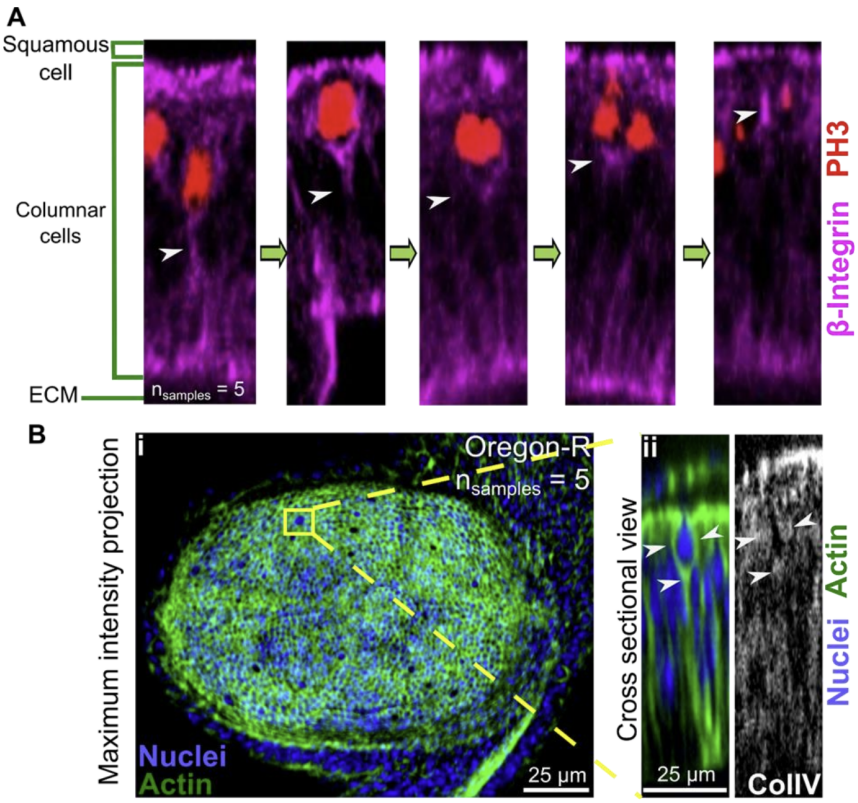

Figure A.1: **Localization of βPS and ColIV around a dividing cell.** (A) Cross-sectional view of a wing imaginal disc showing localization of βPS around a dividing cell. Different images from left to right represent different stages of interkinetic nuclear migration. Discs are labeled with phosphohistone-h3 (PH3) to mark the dividing cells. Fluorescent labels have been indicated as an inset. Sample sizes have been indicated as a bottom inset. (B) (i) (ii) Cross-sectional view of wing cells undergoing mitosis. Discs are labeled with Collagen IV (ColIV) to visualize its expression around a dividing cell. Sample sizes have been indicated on the top-right inset.

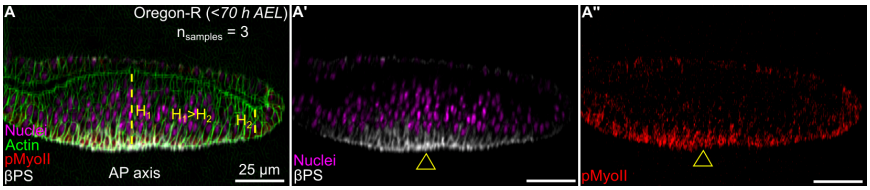

Figure A.2: **Cytoskeletal regulation at earlier stages of development.** Wing imaginal discs belonging to <72 h AEL larval stage of development were dissected and fixed. (A) Optical slice along the AP axis showing localization of Nuclei, Actin, (A') βPS and (A") pMyoII. Sample sizes have been indicated on the top-right inset of (A).

regulation at early developmental stages (Fig A.2). Although the tissue is flat, the cell height is qualitatively patterned across the AP axis. In particular, the cell height is higher at the middle as compared to the lateral ends of the pouch (Fig A.2 A). Moreover, both βPS (Fig A.2 A') and pMyoII (Fig A.2 A") are qualitatively polarized to the basal membrane of the pouch cells. Specifically, βPS is more localized near the central domains.

A.3.3 Correlation Between $\text{pMyoII}_{\text{apical}}$ / $\text{pMyoII}_{\text{basal}}$ and Local Cell Height (H) Increases with the Age of the Disc. The Gradient of H Across the DV Axis Increases with the Age of the Disc

We used the image processing pipeline described in Appendix A subsection "Quantification of Morphological and Signaling-Related Features from the Wing Imaginal Discs" to calculate the ratio of apical to basal fluorescence of pMyoII for 90 discretized cells along the AP axis. We also calculate the average lateral cell heights for the discretized cells to evaluate the correlation between $pMyoII_{apical}/pMyoII_{basal}$ and local cell height (H) (Fig A.3 A). A straight line is fit using scikit-learn [108]. An averaged R^2 value calculated over multiple samples denoted by $R^2(l)$ and an R^2 value for the combined data denoted by $R^2(g)$ from multiple samples are presented as separate insets in the plot (Fig A.3 D i-v). Different colors indicate data from different samples. We also carry out an F-test to estimate the statistical significance of the fit model [109, 110]. The p-values of the F-test have been indicated as insets. The average R^2 value for discs belonging to late developmental stages ($\geq$ 84 h AEL)

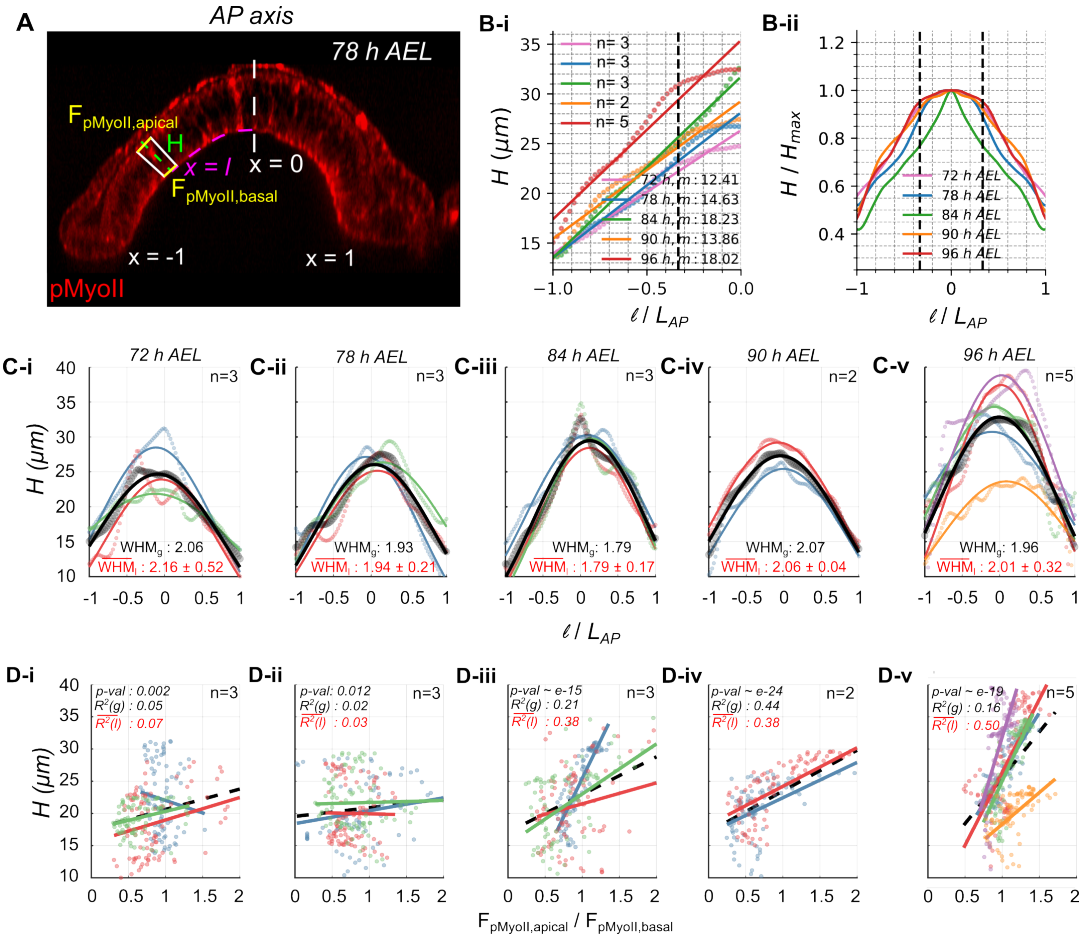
A
AP axis
78 h AEL
F pMyoII,apical
H
x = l
x = 0
F pMyoII,basal
x = -1
x = 1
pMyoII
B-i
H (μm)
n= 3
n= 3
n= 3
n= 2
n= 5
72 h, m : 12.41
78 h, m : 14.63
84 h, m : 18.23
90 h, m : 13.86
96 h, m : 18.02
ℓ / L_AP
B-ii
H / H_max
72 h AEL
78 h AEL
84 h AEL
90 h AEL
96 h AEL
ℓ / L_AP
C-i
72 h AEL
n=3
WHM_g : 2.06
WHM_l : 2.16 ± 0.52
C-ii
78 h AEL
n=3
WHM_g: 1.93
WHM_l : 1.94 ± 0.21
C-iii
84 h AEL
n=3
WHM_g: 1.79
WHM_l : 1.79 ± 0.17
C-iv
90 h AEL
n=2
WHM_g: 2.07
WHM_l : 2.06 ± 0.04
C-v
96 h AEL
n=5
WHM_g: 1.96
WHM_l : 2.01 ± 0.32
H (μm)
ℓ / L_AP
D-i
p-val : 0.002
R²(g) : 0.05
R²(l) : 0.07
n=3
D-ii
p-val: 0.012
R²(g) : 0.02
R²(l) : 0.03
n=3
D-iii
p-val ~ e-15
R²(g) : 0.21
R²(l) : 0.38
n=3
D-iv
p-val ~ e-24
R²(g) : 0.44
R²(l) : 0.38
n=2
D-v
p-val ~ e-19
R²(g) : 0.16
R²(l) : 0.50
n=5
H (μm)
F pMyoII,apical / F pMyoII,basal

Figure A.3: (A) The wing disc cross section was discretized into 60 computational cells as described in Appendix A subsection "Quantification of Morphological and Signaling-Related Features from the Wing Imaginal Discs". $F_{Myosin,apical/basal}$ and indicates the fluorescence intensity of pMyoII in the apical and basal cell surface of the computational cell, respectively. l denotes the distance of the cell along the basal surface from the pouch center. The distance is further normalized by dividing l by half of the length of the pouch basal surface (L). (B-i) Plot showing the variation of cell height between the lateral and medial pouch domains. Each trend line in different colors represents averaged height values for discs at varying stages of development. The sample size associated with the averaging has been included as the top right inset. Further, a straight line was fitted to the trend, and the slope of the fitted lines across different development times has been reported within the plot. (B-ii) Plot showing normalized average height across the AP axis. Lines are color-coded based on the developmental stage. (C) Plot showing variation of cell height across the DV axis. Solid lines indicate the Gaussian model fit, while points (transparent) are the actual cell heights derived from the imaging data. The solid black line indicates the model fit for the combined data from multiple samples. WHM represents width of the curve at half maximum where the height was fitted to a curve to create statistical models of height regulation. Sample sizes have been indicated on the top-right inset of each plot. (D) Correlation between $pMyoII_{apical}/pMyoII_{basal}$ and cell height H for discs belonging to different stages of development. Different colors indicate data from different samples. Sample sizes have been indicated on the top-right inset of each plot. A straight line is fit to model correlations for data from individual samples (color lines). Average R^2 values of the fits have been indicated as $R^2(l)$. A linear model is next fit to the aggregated data using multiple samples (black dashed line). $R^2(g)$ represents the R^2 value of the model fit.

is greater than that of younger discs (< 84 h AEL). Moreover, the linear fits are statistically significant only for discs belonging to 84-96 h AEL.

Next, we analyzed the variation of cell height across the AP axis (Fig A.3 B, C). We first plotted the normalized cell height along the pouch AP axis for discs belonging to different developmental stages. The normalization was carried out by dividing the height of each cell by the maximum cell height (Fig A.3 B-ii). MATLAB [107] was then used to fit Gaussian models for modeling cell height across the AP axis for each sample across different developmental stages (Fig A.3 C i-v). Different colors are used to indicate data and models for different samples within the same developmental stage. We additionally evaluated the width at half maximum (WHM) for all the fits and reported the averaged WHM across all of the samples and also for a fit across the entire data. There is no statistically significant observed change in WHM across the age of the disc. Lastly, to study how the cell height varies across the AP axis during development, we fit straight lines to averaged cell height profiles across half of the pouch (Fig A.3 B-i). An analysis of slopes of fits reveals that the slope is greater for discs belonging to late development stages ($\geq$ 84 h AEL) as compared to the early development stages ($\leq$ 78 h AEL). Thus, the medial tissue height increases at a greater rate as compared to the lateral height of the tissue during development.

A.3.4 Colocalization of Actin, pMyoII and βPS Increases with the Age of the Disc

Discs belonging to two different stages of development (72 h AEL (Fig A.4), and 96 h AEL (Fig A.5) larval stages) were fixed, and an immunohistochemistry assay was carried out to label the expression of cytoskeletal regulators, including Actin, pMyoII and βPS. We next discretized the pouch AP axis into 90 cells as described in Appendix A subsection "Quantification of Morphological and Signaling-Related Features from the Wing Imaginal Discs". The averaged apical, basal, and lateral fluorescence intensity of Actin, pMyoII and βPS was calculated for the cells. To remove background noise in the imaging data, a rolling ball background subtraction [37] was performed using a 50-pixel ball radius in ImageJ [111].

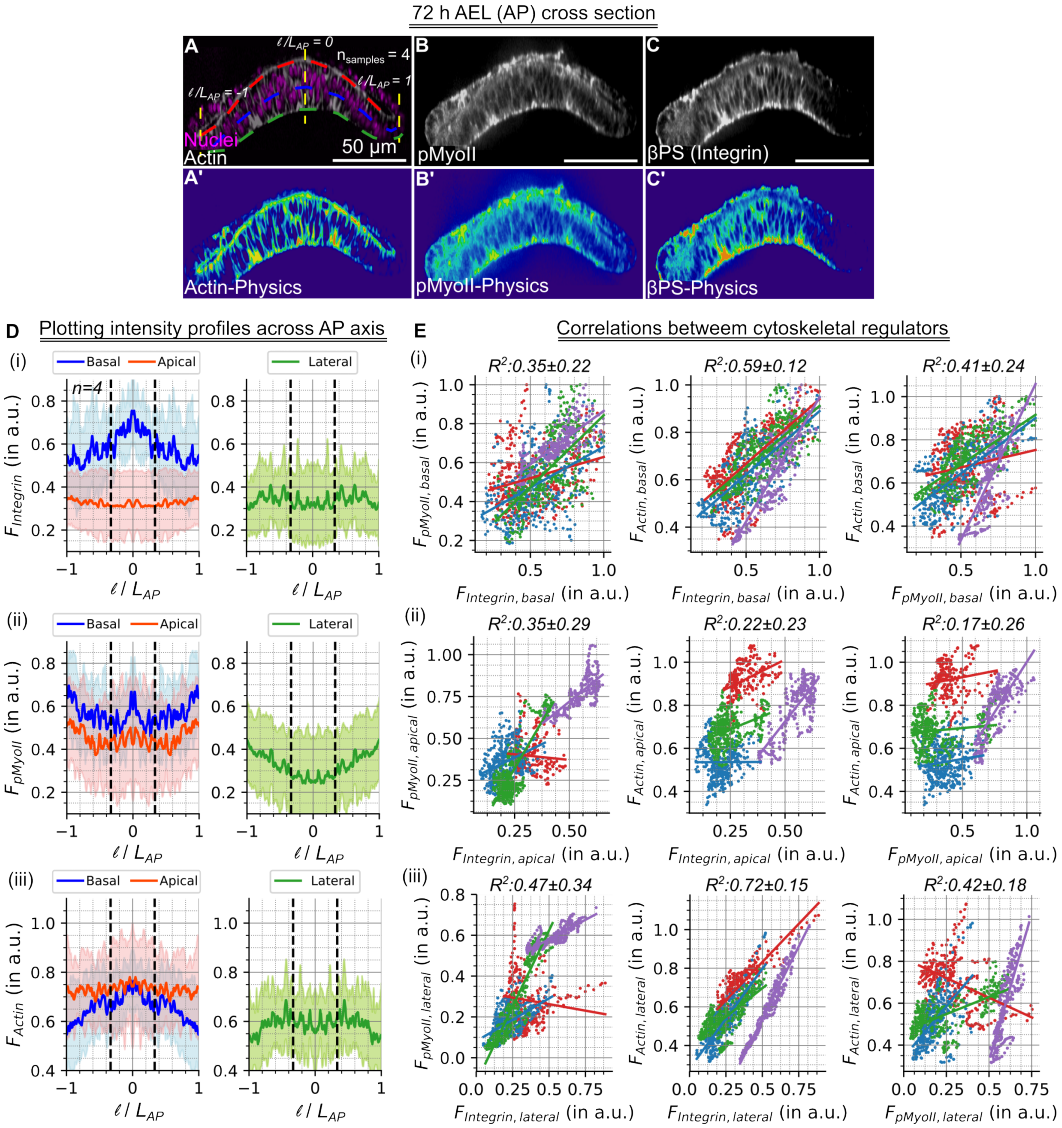

Figure A.4: **Actin, Myosin, and Integrin at earlier stages of development are expressed predominantly near the basal surface of pouch cells. Integrin correlates strongly with Actin.** (A-C) AP cross-section of wing imaginal discs staged to 72 h AEL. Fluorescent labels are indicated in the bottom left panel of each cross-section. Fluorescent intensity of Actin, Myosin, and Integrin were calculated over the apical, basal, and lateral sections of the disc proper (DP) cells for several samples (n = 5) (D) (i- iii) Variation of Integrin, Myosin and Actin localization across the pouch apical, basal and lateral surface. (E) Correlations between Actin, Myosin, and Integrin at the pouch cell's apical, basal, and lateral surfaces.

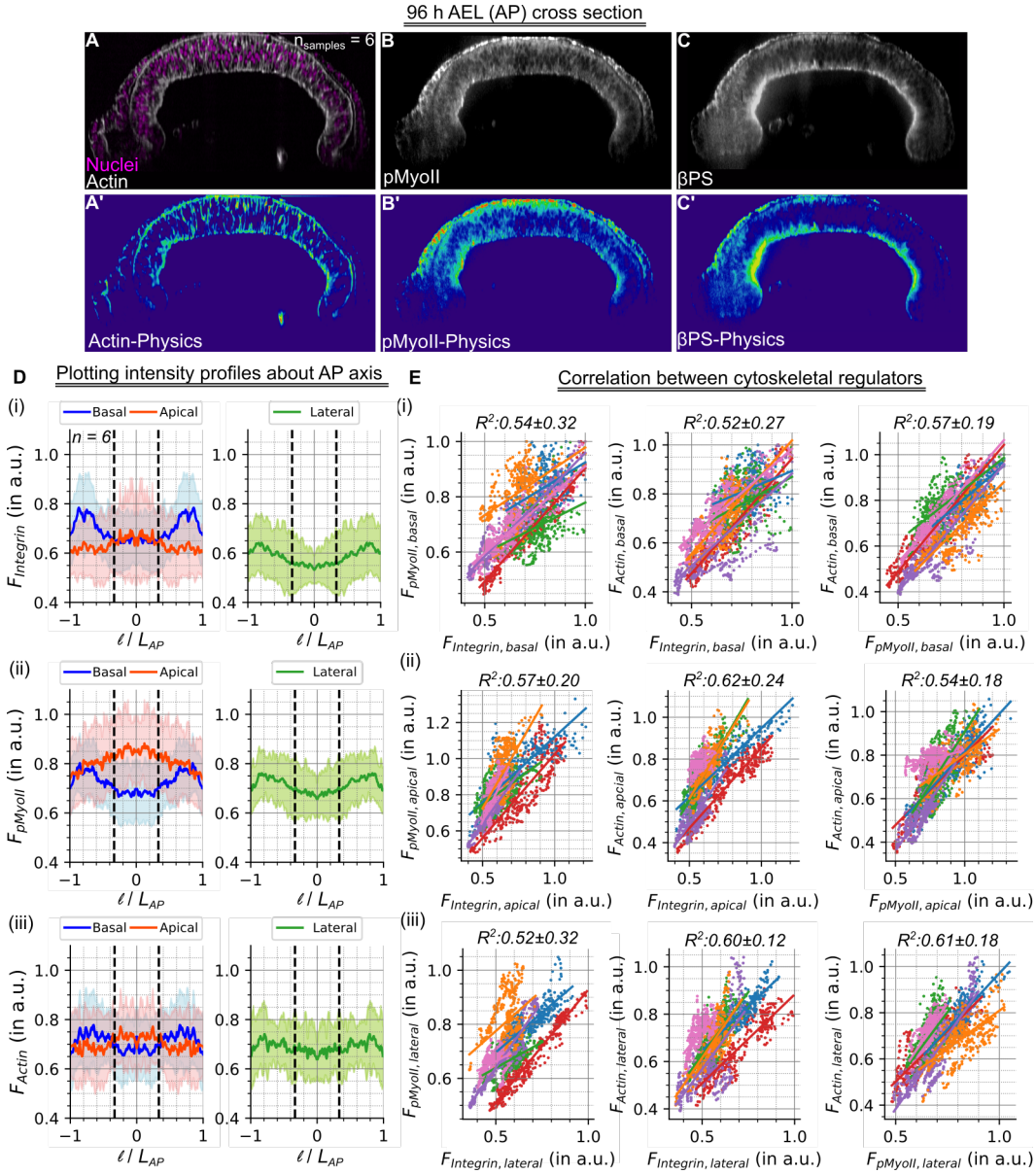

Figure A.5: **Actin, Myosin, and Integrin correlate strongly and are predominantly expressed in the basal-lateral region of the pouch.** (A-C) AP cross-section of a wing imaginal disc dissected from larvae staged to 96 h AEL. Fluorescent labels are indicated in the bottom left panel of each cross-section. Fluorescent intensity of Actin, Myosin and Integrin were calculated over the apical, basal, and lateral sections of the pouch for several samples (n = 7) (D) (i - iii) Variation of Integrin, Myosin and Actin localization across the apical, basal and lateral surface of columnar pouch cells. (E) Correlations between Actin, Myosin, and Integrin at the apical, basal and lateral surfaces of columnar pouch cells.

Further, the location of each discretized cell within the AP axis was defined as its normalized distance from the center of the AP axis. Normalization was carried out by dividing the distance of a particular discretized cell by half the curve length of the basal surface.

We first analyzed Actin, pMyoII and βPS expression profiles across the AP axis at the apical, basal, and lateral sides of cells (Fig A.4 D, Fig A.5 D). The x-axis of the plot is the normalized location along the basal surface. The solid line indicates the mean fluorescence of the measured cytoskeletal regulators ((i) βPS, (ii) pMyoII, (iii) Actin), while the shaded region indicates the standard deviation in fluorescence reported over multiple samples. At earlier stages of development, pMyoII and βPS are predominantly basal (Fig A.4 Di, ii). Moreover, integrin is localized primarily at the medial pouch region. In fact, it is like the expression at earlier developmental stages, as shown qualitatively in Fig A.2. However, at later stages of development, pMyoII in the medial pouch domain starts to become apical. In contrast, both pMyoII and βPS start to acquire more lateral expressions in the basal surface of the pouch (Fig A.5 Di, ii).

We next evaluated correlations between the extracted fluorescent intensity of Actin, pMyoII, and βPS in the apical, basal, and lateral surfaces of the pouch, respectively (Fig A.4 E, Fig A.5 E). Normalized fluorescence intensities of two components at a time ((βPS, pMyoII), (βPS, Actin), (pMyoII, Actin)) were plotted for multiple samples, and a straight line was fit using the LinearRegression library within scikit-learn [108]. R^2 values across multiple samples were averaged and reported on top of each plot and used as a metric to evaluate the strength in colocalization. Different colors within the plot represent data from different samples. We report an increased averaged R^2 values of the fit for all of the correlations along the basal surface as the disc ages (Fig A.4 E-i, Fig A.5 E-i).

A.3.5 Proliferation Decreases with an Increase in Pouch Size

In this section, we report a decrease in cell proliferation with an increase in the age of the disc. The obtained result agrees with previous literature studies [112]. Wing imaginal discs were dissected from larvae of different sizes belonging to different stages of development and

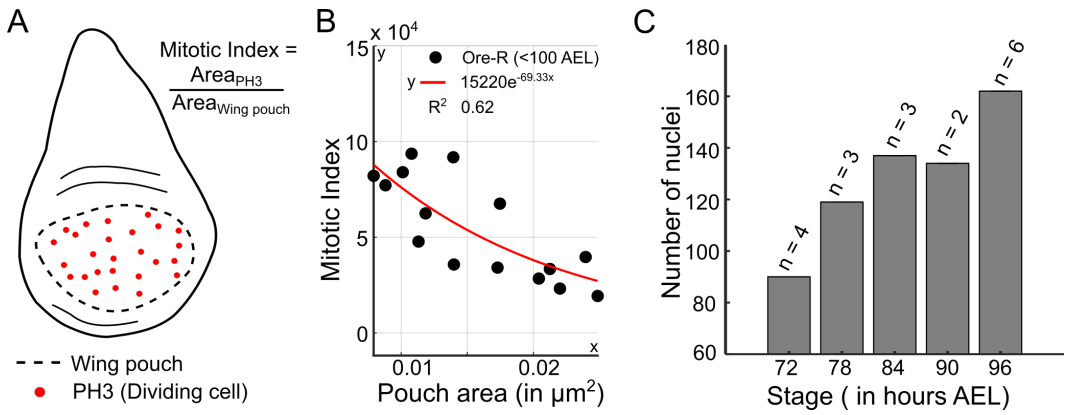

Figure A.6: **Cell proliferation decreases with the age of the pouch.** (A) Mitotic index is defined as the ratio of the area acquired by cells expressing Phospho Histone-H3 (PH3) over the area of the wing disc pouch. (B) Plot showing the variation of the mitotic index with respect to the pouch size. The red line indicates an exponential fit obtained through regression in MATLAB. (C) Plot showing the distribution of an average number of nuclei along the pouch AP axis with the age of the disc

proliferating cells were marked with anti-PH3. The mitotic index was next defined as the ratio of the area of cells that are marked by PH3 over the area of the pouch (Fig A.6 A). A 2D scatter plot was plotted with the X-axis representing the pouch area and the Y-axis the mitotic index (Fig A.6 B). An exponential decay model was next fit to the data using MATLAB's [107] fit function. The model details along with the goodness of fit indicated by an R^2 value have been included as a plot inset. The tendency of cells to divide decreases as the size of the pouch increases.

A.3.6 In Silico Model Scenarios of Patterned Cytoskeletal Regulation Across the AP Axis.

Multiple model parameters representing different functions of cytoskeletal regulation were patterned across the pouch's AP axis. Values of parameters were kept separate for the pouch medial and lateral domains and across the apical and basal surfaces depending upon the parameter varied. In total, we varied eight model parameters generating a total of 15 parameter profiles (Fig. A.7). For instance, in Case I, we varied the actomyosin contractility

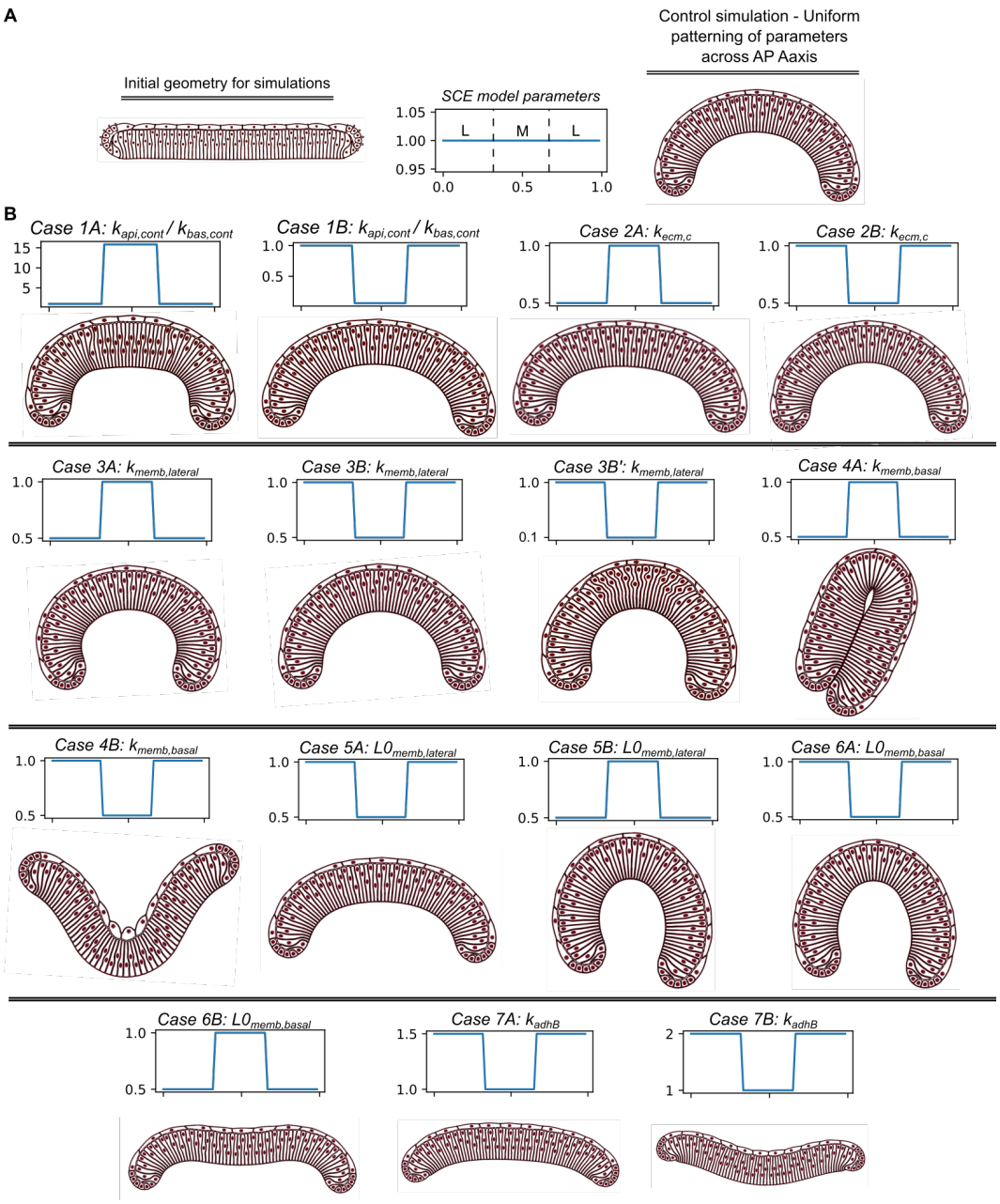

Figure A.7: **Key parameters that impact the basal curvature of the tissue.** (A-F) Through a series of cases, model parameters representing mechanical properties of cell cytoskeleton, actomyosin and adhesion were varied across the AP axis. The profiles of parameters are plotted above the final simulated shape.

in the model by increasing the apical ($k_{api,cont}$) and basal ($k_{bas,cont}$) contractility in the medial domain of the pouch and also increasing $k_{bas,cont}$ more than $k_{api,cont}$ in the lateral ends. The increase in the center was higher than that away from the center. This recapitulates the expression of pMyoII at 96 h AEL developmental stage, where we report higher apical contractility in the pouch medial region and a higher basal contractility in the lateral ends of the pouch (Fig 2.4 F). We also varied the parameters associated with the basal ECM stiffness ($k_{ecm,c}$), the membrane tension ($k_{memb,basal}$, $k_{memb,lateral}$, $L0_{memb,lateral}$, $L0_{memb,basal}$) and the Integrin-based adhesion between the basal region of columnar cells and the ECM (k_{adhB}) (Appendix Tables A.5, A.6). Cross sections of the simulation output have been shown along with the varying parameter profile across the AP axis on the top of each figure (Fig A.7).

A.3.7 Tissue Local Height is Regulated by the Difference in Apical-Basal Contractility

To test if cell height is driven by the apical-basal stiffness of cells, we ran simulations with a differential patterning of contractility parameters across the apical and basal surfaces. First, we divided the tissue into three domains (a medial domain and two lateral domains) and perturbed $k_{api,cont}$ and $k_{bas,cont}$ in each of these domains (Fig A.8 A). The contractility multipliers used in each of the cases are listed in the table in Fig A.8 B. Note that the apical and basal contractility multipliers get multiplied to $k_{api,cont}$ and $k_{bas,cont}$, respectively, to increase or decrease the strength of the actomyosin contractile springs. Cases 1A and 1B are reproduced from Fig A.7 A, where actomyosin contractility was increased and decreased, respectively, in the medial domain of the pouch. Using Case 1A as a comparison, we increased both $k_{api,cont}$ and $k_{bas,cont}$ in the medial domain while ensuring that the ratio of $k_{api,cont}/k_{bas,cont}$ remained constant (Case 1C) and also increased (Case 1D). Next, we used a multiple linear regression to further perturb $k_{api,cont}$ and $k_{bas,cont}$ (Cases 1E-1J) in the medial domain. Finally, in addition to varying the actomyosin contractility in the medial domain similar to Cases 1E-1J, we tested the effect of decreasing the basal contractility (by decreasing $k_{bas,cont}$) in the lateral domain of the pouch (Cases 1K-1V).

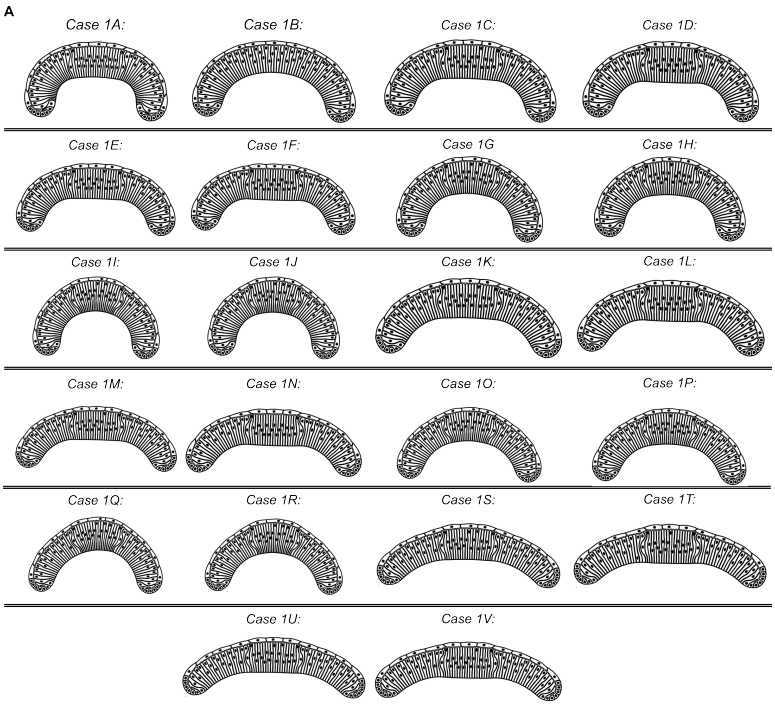

B

Contractility multiplier profile

		Lateral	Medial	Lateral
Case 1A	apical	0.0625	**1.333**	0.0625
	basal	1.5	**2.0**	1.5
Case 1B	apical	0.0625	**0.0029**	0.0625
	basal	1.5	**1.125**	1.5
Case 1C	apical	0.0625	**1.675**	0.0625
	basal	1.5	**2.5**	1.5
Case 1D	apical	0.0625	**2.61**	0.0625
	basal	1.5	**3.0**	1.5
Case 1E	apical	0.0625	**1.666**	0.0625
	basal	1.5	**2.219**	1.5
Case 1F	apical	0.0625	**2.0**	0.0625
	basal	1.5	**2.240**	1.5
Case 1G	apical	0.0625	**1.666**	0.0625
	basal	1.5	**3.856**	1.5
Case 1H	apical	0.0625	**2.0**	0.0625
	basal	1.5	**3.878**	1.5
Case 1I	apical	0.0625	**1.666**	0.0625
	basal	1.5	**4.948**	1.5
Case 1J	apical	0.0625	**2.0**	0.0625
	basal	1.5	**4.970**	1.5
Case 1K	apical	0.0625	**1.675**	0.0625
	basal	**1.0**	**2.5**	**1.0**

		Lateral	Medial	Lateral
Case 1L	apical	0.0625	**2.61**	0.0625
	basal	**1.0**	**3.0**	**1.0**
Case 1M	apical	0.0625	**1.666**	0.0625
	basal	**1.0**	**2.219**	**1.0**
Case 1N	apical	0.0625	**2.0**	0.0625
	basal	**1.0**	**2.240**	**1.0**
Case 1O	apical	0.0625	**1.666**	0.0625
	basal	**1.0**	**3.856**	**1.0**
Case 1P	apical	0.0625	**2.0**	0.0625
	basal	**1.0**	**3.878**	**1.0**
Case 1Q	apical	0.0625	**1.666**	0.0625
	basal	**1.0**	**4.948**	**1.0**
Case 1R	apical	0.0625	**2.0**	0.0625
	basal	**1.0**	**4.970**	**1.0**
Case 1S	apical	0.0625	**1.675**	0.0625
	basal	**0.5**	**2.5**	**0.5**
Case 1T	apical	0.0625	**2.61**	0.0625
	basal	**0.5**	**3.0**	**0.5**
Case 1U	apical	0.0625	**1.666**	0.0625
	basal	**0.5**	**2.219**	**0.5**
Case 1V	apical	0.0625	**2.0**	0.0625
	basal	**0.5**	**2.240**	**0.5**

Figure A.8: **Variation of apical to basal actomyosin contractility impacts cell height.** (A) Shapes obtained from varying actomyosin contractility in the pouch medial and lateral domains. Cases 1A and 1B are reproduced from Fig A.7. In cases 1C and 1D, both apical and basal actomyosin contractility was increased in the medial domain. Linear regression was used to vary actomyosin in the medial region in cases 1E-1J. Finally, in cases 1K-1V, in addition to varying contractility in the medial domain (similar to cases 1E-1J), the effect of decreasing the basal contractility in the lateral domain is tested. (B) A table of the apical and basal contractility multipliers for each simulation case. Note that the apical and basal contractility multipliers get multiplied to $k_{api,cont}$ and $k_{bas,cont}$, respectively. The role of these multipliers is to increase or decrease the strength of the actomyosin contractile springs.

Next, we carried out a quantitative comparison between phenotypic changes that occurred between the 72 and 96-hour discs and the simulation cases where actomyosin contractility was patterned across the AP axis, in contrast to the uniform patterned contractility in the control simulation (Fig A.9). We first visualized metrics, including the ratio of lateral to medial basal curvature (Fig A.9 A-i), medial tissue height (Fig A.9 Aii), and the ratio of nuclear positioning between the medial and lateral compartments (Fig A.9 A-iii). Compared to the control, all of the simulation cases led to an increase in tissue height and a basal shift of nuclei, consistent with our observations in the experimental data. However, only a few simulations resulted in the flattening of the midsection. We then visualized the differences in these phenotypic traits (Fig A.9 B). For experiments, the difference was calculated by subtracting these geometric features between the 96 and 72-hour discs. For the simulations, the morphological features of all cases were subtracted from the control case. Errors within individual metrics were normalized by dividing by the maximum reported error. Finally, we quantified the overall error by squaring and summing individual errors. Using this approach, we identified Case 1D as the case that matches all three metrics most accurately. Note that this case is presented as Case 1A' in Figures 2.4 - 2.6 of the main text.

To further explore the role of apical to basal contractility in cell height, we ran additional simulations. This time, the pouch was subdivided into five nested domains, namely: left (L), left medial (LM), medial (M), right medial (RM), and right (R). Perturbation of $k_{api,cont}$ and $k_{bas,cont}$ was done only in the medial domain of the pouch (Fig A.10 A-A"). The parameter values for the three different cases are listed in a table in Fig A.10 B. Initially, we assumed the contractility to be localized only on the basal surface. We first increased both $k_{api,cont}$ and $k_{bas,cont}$ without changing the ratio of $k_{api,cont}/k_{bas,cont}$. Analysis of the height profiles showed an increase in levels of contractilities in the apical and basal surface without changing the ratio of the two increased cell height (Fig A.10 A', C). Next, we increased both $k_{api,cont}$ and $k_{bas,cont}$ in such a way that the increment also increased the ratio between the two. A slight change in height was observed as compared to the previous case (Fig A.10 A", C).

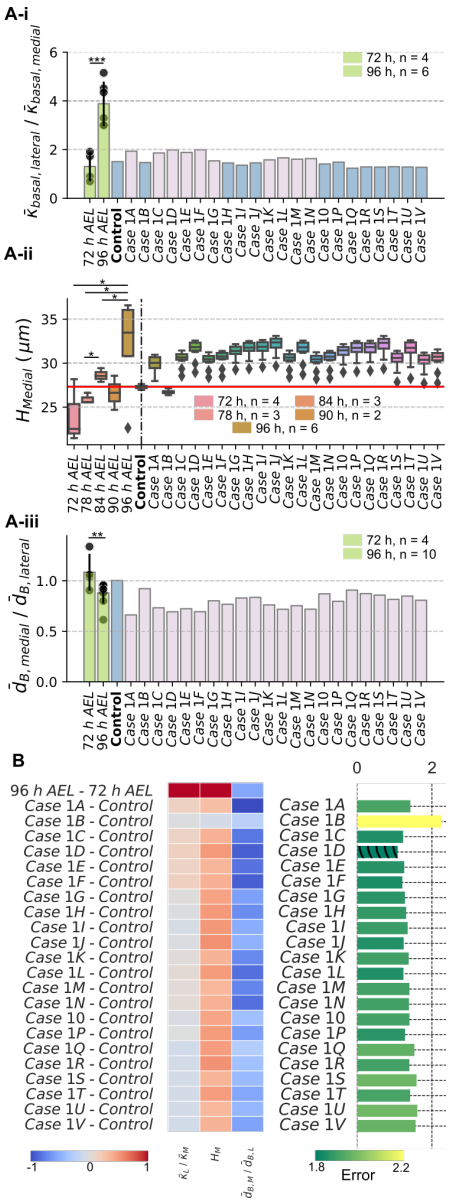

Figure A.9: **Effect of variation of apical-basal contractility on basal curvature, cell height and nuclear positioning.** (A) Bar graph visualizing comparison of (i) ratio of average lateral curvature to basal curvature (ii) medial tissue height (iii) ratio of $\bar{d_B}$ in medial to lateral compartment for wing discs belonging to 72 and 96 h AEL of development and the simulations presented in Fig A.8. (B) Differences between control and the perturbation simulations (y-axis) were normalized and compared with differences of measured properties (x- axis) between 72 h AEL and 96 h AEL (1st row). The combined errors from the three metrics were calculated through differences between the experimental and simulation data. The error bars are color-coded based on their values.

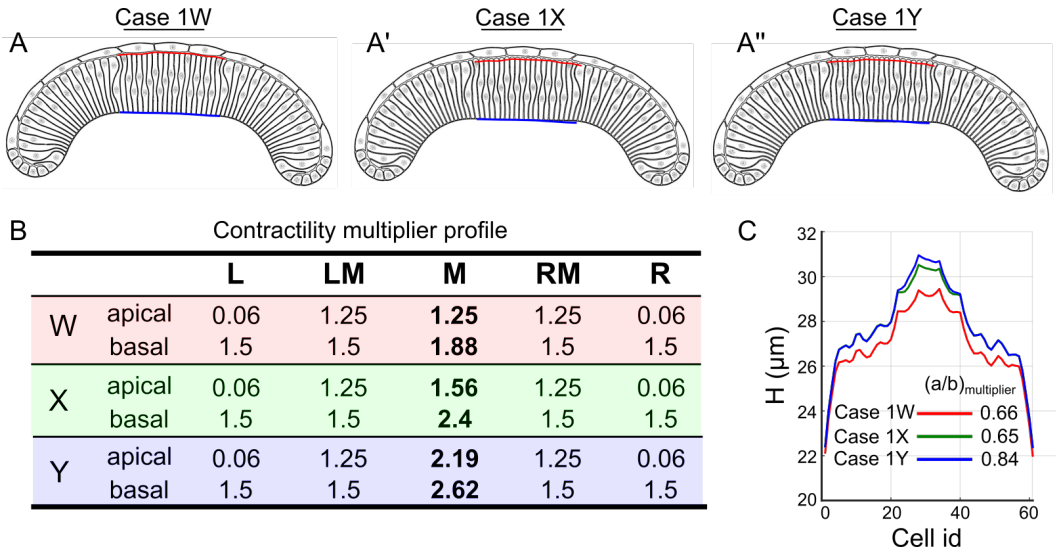

		L	LM	M	RM	R
W	apical	0.06	1.25	**1.25**	1.25	0.06
	basal	1.5	1.5	**1.88**	1.5	1.5
X	apical	0.06	1.25	**1.56**	1.25	0.06
	basal	1.5	1.5	**2.4**	1.5	1.5
Y	apical	0.06	1.25	**2.19**	1.25	0.06
	basal	1.5	1.5	**2.62**	1.5	1.5

Figure A.10: **Effect of apical-basal contractility profiles on cell height.** (A-A") Stable shapes obtained because of varying actomyosin contractility in the pouch medial domain. In cases W-Y the pouch was subdivided into five domains: left (L), left medial (LM), medial (M), right medial (RM), and right (R) where the apical-basal contractility ratio was only varied in the medial (M) domain. (B) A table of parameters for the simulations run in this case study was organized according to the five domains (L, LM, M, RM and R). For each case W-Y, the top row represents the apical contractility multiplier that gets multiplied to $k_{api,cont}$ while the bottom row represents the basal contractility multiplier for $k_{bas,cont}$. These multipliers are used to increase the strength of the actomyosin contractile springs. (C) Height profiles in the tissue are plotted against the cell id (from left to right of tissue) for the different cases run in this study. The ratio of the apical to basal contractility multiplier $(a/b)_{\text{multiplier}}$ for the medial domain associated with each case in (B) has been included as part of the figure legend. Note that a represents the contractility multiplier for $k_{api,cont}$ while b represents the contractility multiplier associated with $k_{bas,cont}$.

A.3.8 Knockdown of Integrin Increases Basal Curvature While Knockdown of Rho1 Reduces Basal Curvature

$MS1096 - Gal4$ driver was used to differentially express RNAi against mys and Rho1 (Fig A.11 A-C). The Gal4 driver allows more inhibition in the dorsal compartment while decreasing its effect as one moves towards the ventral compartment. We used multiple samples to quantify the basal curvature of the pouch across the DV axis (Fig A.11 A'-C'). Compared to the control, expression of mys^{RNAi} in the dorsal compartment led to a sharp increase in tissue folding near the lateral ends of the pouch. In contrast, the expression of $\text{Rho1}^{\text{RNAi}}$ led to a reduction in basal curvature reflected by flattening of the basal surface in the dorsal compartment (region of perturbation).

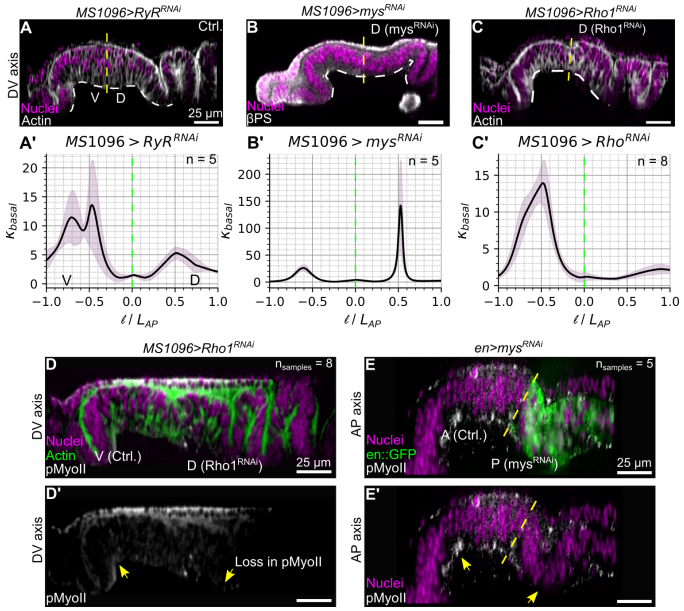

Figure A.11: **Loss of Integrin increases while loss of Rho1 reduces basal curvature.** MS1096-Gal4 driver was used to knock down mys and Rho1 in the dorsal compartment of the wing imaginal disc. Comparisons were done using the $MS1096 > RyR^{RNAi}$ control. (A-C) DV cross-sections of the pouch are shown. (A'-C') Quantification of basal curvature across the DV axis is shown. Solid line indicates the mean while the shaded region indicates the standard deviation of n predictions. Sample sizes have been indicated on the top-right inset of each plot. (D, D') DV cross sections for the $MS1096 > Rho1^{RNAi}$ genetic perturbations. (E, E') AP sections for $en > mys^{RNAi}$ genetic perturbations. Fluorescent labels have been indicated within the plot.

We also carried out immunostaining assays to see if the inhibition of mys and Rho in the wing disc effects pMyoII. Analysis of pMyoII fluorescence across the pouch DV axis for the $MS1096 > Rho1^{RNAi}$ genetic perturbations shows a decrease of pMyoII in the dorsal compartment of pouch where Rho1 activity was suppressed (Fig A.11 D, D'). Similarly, for $en > mys^{RNAi}$, we also report a reduction in pMyoII fluorescence in the posterior compartment where mys was inhibited (Fig A.11 E, E'). In summary, we qualitatively show that a loss in both Rho1 and mys can affect accumulation of pMyoII within the pouch.

A.3.9 A Cell-Specific Increase in Control Volumes (Ω_0) Causes an Increase in Cell Height (H) Without Changing its Gradient Along the DV Axis

In comparison to Case 8C, the simulation listed in Figure 2.5 E, G', we ran an additional simulation where we used a similar gradient to increase the cell volume of each cell by adjusting the maximum and minimum cell volumes such that the overall tissue volume was equal to the control simulation (Fig A.12 A, E). Compared to Case 8C, the height of cells in Case 8D was higher (Fig A.12 B). However, no qualitative difference in gradients of cell height across the AP axis is reported.

A.3.10 Loss of Rho1 Pushes the Nuclei Basally

MS1096-Gal4 driver was used to inhibit Rho1 in the dorsal compartment of the wing imaginal disc (Fig A.13 A). Note that the Gal4 driver also leads to inhibition of Rho1 in the ventral compartment, but the degree of perturbation decreases while moving away from the DV compartment boundary. To study how inhibition of Rho1 affects nuclear positioning, we segmented the nuclei in the DV section of the pouch. We next quantified the proximity of nuclei with the basal surface by estimating $\bar{d_B} = \frac{d_B}{d_A+d_B}$ (Appendix A subsection "Quantification of Nulcear Positioning", Appendix A Fig A.25). As shown in Fig A.13 C, the nuclei are located much closer to the basal surface than the nuclei within the dorsal compartment (internal control).

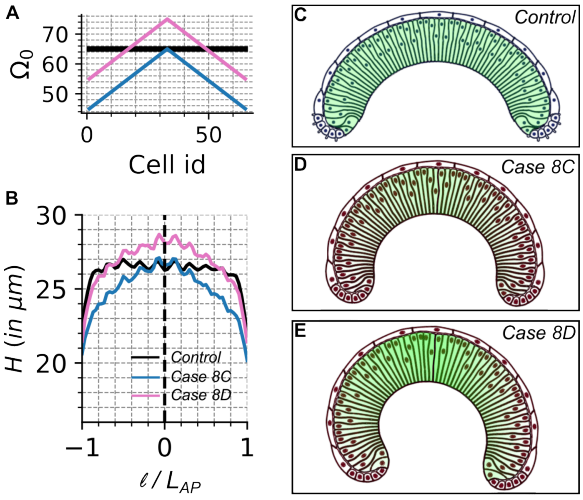

Figure A.12: **Increasing cell volumes globally causes a global increase in the cell height.** (A) Plot showing variation of Lagrange multiplier (Ω_0) along the pouch AP axis for different case studies. (B) Plot showing variation of lateral cell height (H) along the pouch AP axis for the simulated cases. (C-E) Model outputs for the simulated case studies. The green shading indicates a qualitative patterning of Ω_0 across the pouch AP axis.

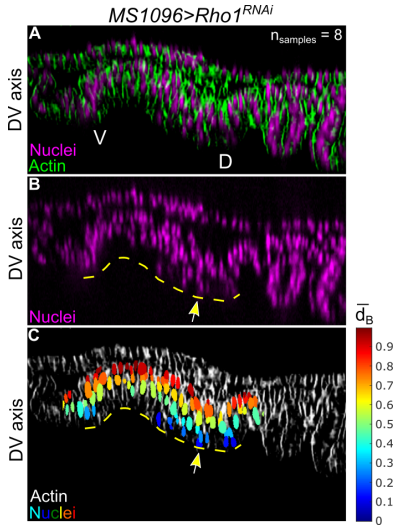

Figure A.13: **Loss of Rho1 pushes the nuclei basally.** (A, B) Inhibition of Rho1 in the dorsal compartment of the wing imaginal disc ($MS1096 > Rho1^{RNAi}$). Fluorescent labels have been indicated as labels in the left bottom corner. (C) Nuclei were segmented and their proximity to the basal surface of epithelia is shown.

A.3.11 Compartment-Specific Expression of InsR and Myc to Increase Proliferation Results in Two Distinct Phenotypes.

We used an engrailed-Gal4 driver to inhibit proliferation in the posterior compartment by expressing the dominant-negative (DN) form of the *Drosophila* insulin receptor (InsR^{DN}) in the posterior compartment (Fig A.14 A i-ii). We confirmed through a PH3 antibody staining that the downregulation of insulin signaling activity through the expression of InsR^{DN} reduced the number of mitotic cells [37] (Fig A.14 A i'-ii'). We also expressed the constitutively active form of insulin receptors (InsR^{CA}) in the posterior compartment of the wing imaginal disc (Fig A.14 A-iii). Expression of InsR^{CA} in the posterior compartment increased the number of mitotic cells in the pouch (Fig A.14 A-iii'). Wing imaginal discs were physiologically staged, and only 3$^{\text{rd}}$ instar wandering larvae were dissected. The *en-Gal4* driver has been used as a control for the comparison (Fig A.14 A-i, i'). We also examined cross-sections along the DV axis in the anterior (Fig A.14 C-i, ii) and posterior compartments (Fig A.14 C-i', ii'). Analysis of the cross-section reveals a similar observed increase in inwards bending upon expression of InsR^{CA} as observed in $Nubbin > InsR^{CA}$ (Fig 2.8 G', H-i). Qualitatively, cross-sections taken in the posterior compartment have an increased inward bending near the pouch lateral domains.

We next overexpressed Myc in the dorsal compartment of the wing imaginal disc (*apterous-Gal4* x UAS-Myc) (Fig A.14 D). Myc is a direct regulator of cell cycle and biogenesis [42], hence its overexpression increases in growth and cell proliferation. We next examined the cross-section along the DV axis, parallel to the AP boundary. Interestingly, very similar to $en > Myc$ (Fig 2.8 K, K'), we see a sharp increase in βPS fluorescence level in the dorsal compartment along with a loss in basal curvature (Fig A.14 E). In summary, the analysis of the biological replicates aligns with the data, and the results are included in the main manuscript in Figure 2.8.

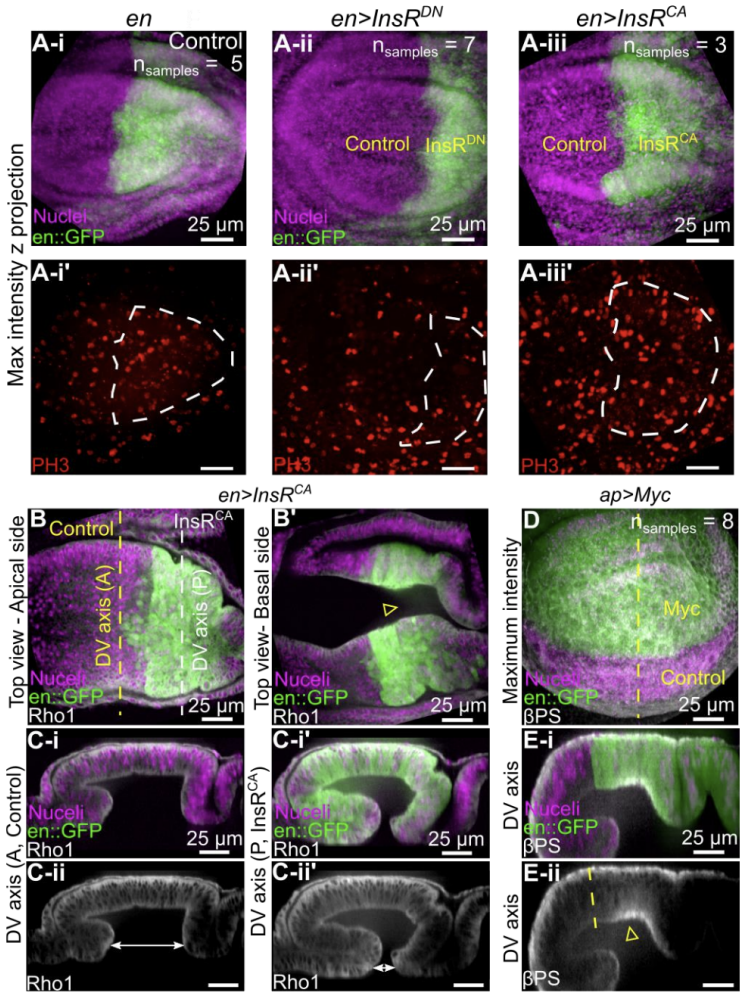

Figure A.14: **Two distinct phenotypes resulting from compartment-specific expression of InsR and Myc to increase proliferation.** (A) Maximum intensity projection of (i-i') control and (ii-ii') samples expressing dominant negative insulin receptor, InsR^{DN}, and (iii-iii') samples expressing constitutively active insulin receptor, $InsR^{CA}$ in the posterior compartment driven by en-Gal4. Proliferating cells are marked by PH3. (B, B') Samples expressing constitutively active insulin receptor $InsR^{CA}$ in the posterior compartment driven by *en-Gal4*. The Gal4 driver is tagged to a GFP to label the compartment boundaries. Additional fluorescent labels have been included within the figure. (C-i, ii, C-i', ii') Cross section taken parallel to the DV axis of the pouch in the anterior and posterior pouch compartments, respectively. (D) Samples expressing constitutively active Myc in the dorsal compartment driven by *ap-Gal4* tagged with GFP to label the compartment boundaries. Additional fluorescent labels have been included within the figure. (E-i, ii) Cross-section taken parallel to DV axis of the pouch with the same fluorescent labels as C. Yellow arrow indicating increase in βPS intensity.

A.3.12 Inhibition of *mTOR* Reduces Cell Proliferation and Inhibits Actomyosin Contractility Resulting in a Decrease in Cell Height and Basal Curvature

To test how proliferation impacts tissue geometry, we studied the effect of downregulating *mTOR*, a direct regulator of the cell cycle and cellular growth in the wing disc (Fig A.15). First, we expressed the dominant negative form of *mTOR* in the posterior compartment with engrailed-Gal4. However, the progeny was lethal. Hence, we expressed $mTOR^{DN}$ in the dorsal compartment of the wing disc with *ap-Gal4* (Fig A.15 A-ii). The expression of $mTOR^{DN}$ in the dorsal compartment resulted in a compartment-specific reduction in basal curvature compared to the control ((Fig A.15 B-i, ii, E-ii). We also report a decrease in cell height upon expression of $mTOR^{DN}$ (Fig A.15 E-i).

Lastly, to study how inhibition of *mTOR* affects cytoskeletal regulation, we carried out IHC assays to measure spatiotemporal changes in βPS, pMyoII and Rho GTPases. Quantification and comparison of fluorescence intensities across both internal and global control revealed that *mTOR* inhibition does not cause any changes in βPS (Fig A.15 D-i). However, we report a statistically significant decrease in both Rho1 and pMyoII at the pouch basal surface (Fig A.15 D-ii). Lastly, we also analyzed the AP cross sections within genetically perturbed $ap > mTOR^{DN}$ samples in the dorsal and ventral compartments of the wing imaginal disc (Fig A.15 Fi-iii). A loss of *mTOR* in the dorsal compartment led to qualitatively reduced basal curvature along the AP axis.

This study reveals that apart from a reduction in cell proliferation, *mTOR* inhibition also reduced both basal pMyoII and Rho1. It is noteworthy to mention that basal pMyoII is a key component of interkinetic nuclear migration (IKNM), a process that is required for cell proliferation within pseudostratified epithelia like wing discs. It is quite possible that a reduction in cell proliferation is a by-product of reduction in basal actomyosin contractility inhibiting IKNM.

To corroborate our experimental results, we used our computational model to run additional simulations where we decreased both cell proliferation and basal contractility in

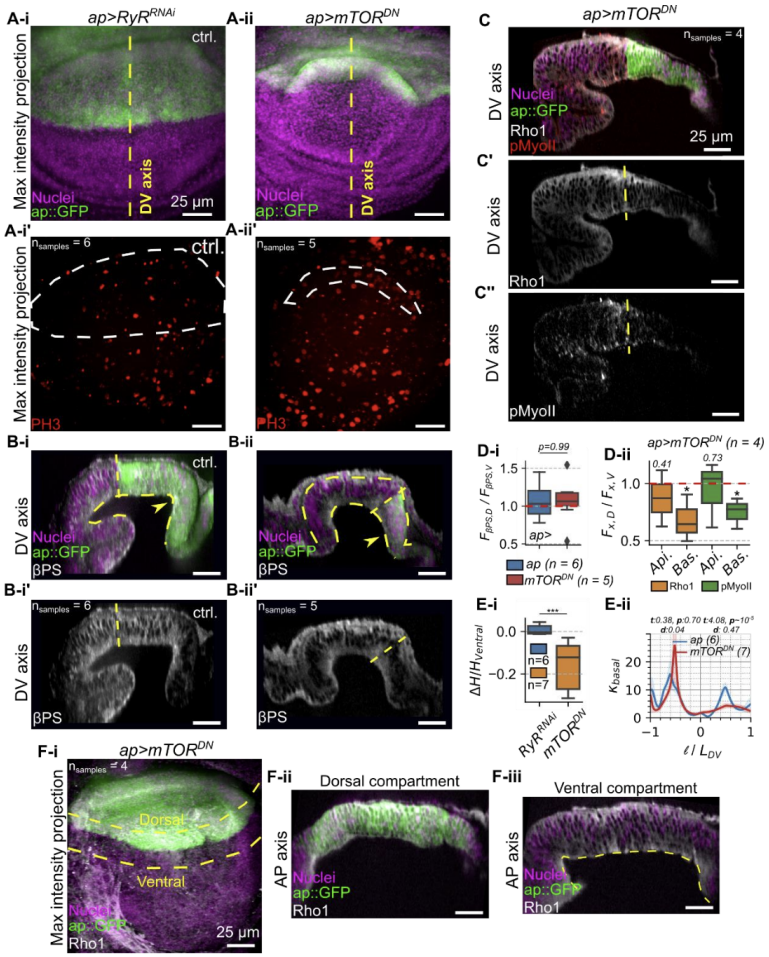

Figure A.15: (A) Maximum intensity projection of (i-i') control and (ii-ii') samples expressing dominant negative $mTOR$, $mTOR^{DN}$ in the dorsal compartment using ap::GFP. (B) Cross-section along DV-axis for (i) control and (ii)$mTOR^{DN}$. (C-C") Immuno staining of Rho1 and pMyoII for $ap > mTOR^{DN}$ genetic perturbations. (D) Quantification of ratio of βPS across the dorsal to ventral compartment for discs expressing $mTOR^{DN}$ ($ap > mTOR^{DN}$) in the wing disc dorsal compartment. Similar analysis for (ii) Rho1 and pMyoII across pouch apical and basal surface. (E-i) Box plot visualizing the differences in average cell heights between dorsal and ventral compartments of the wing disc for $ap > RyR^{RNAi}$ and $ap > mTOR^{DN}$ genetic perturbations (ΔH). ΔH was normalized by the average height of the tissue in ventral compartment (internal control). (E-ii) Plots quantifying the basal curvature profile for the DV pouch section of $ap > RyR^{RNAi}$ and $ap > mTOR^{DN}$. Solid color indicates the mean while the shaded region shows the standard error of mean. The t-statistic (t), p-value (p) and effect size (d) for comparison of mean curvature profiles of control and genetically perturbed samples in dorsal and ventral compartments have been indicated on the top of plot. (F) AP cross sections of (i) $ap > mTOR^{DN}$ mutant taken in the (ii) dorsal and (iii) ventral compartments of the wing imaginal disc.

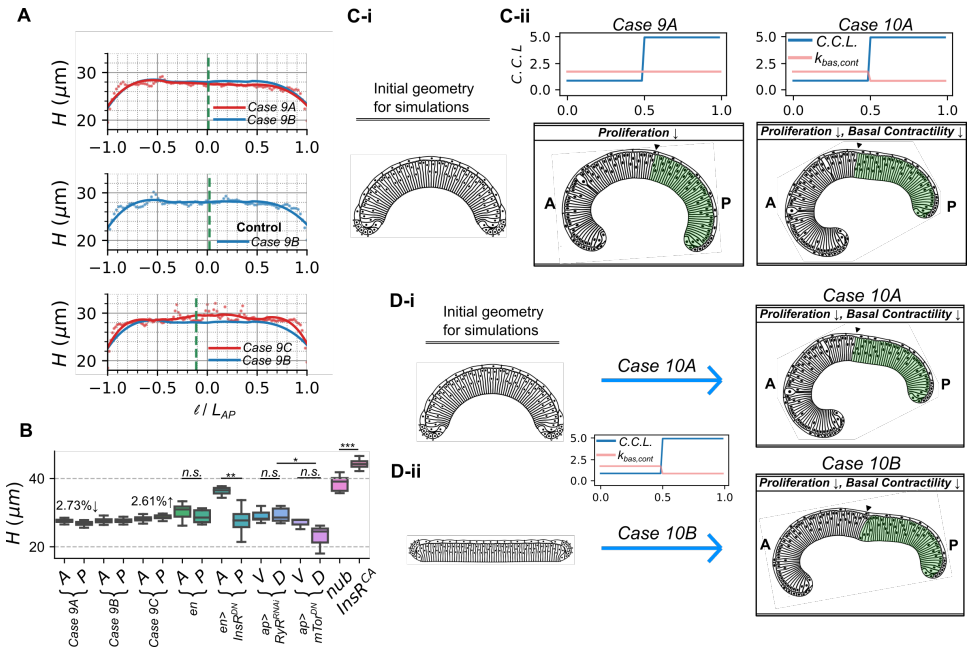

Figure A.16: (A) Quantification of cell heights for the Simulation Cases 9A-C presented within Fig 2.7 of the main manuscript. (B) Box plot visualizing the cell heights within the control (anterior ∼ en or ventral ∼ ap) and perturbation (posterior ∼ en or dorsal ∼ ap) compartments of simulations and experimental data presented within Fig 2.7 of the main manuscript. (C) (i) Initial geometry used for Cases 9A and 10A. (ii) Simulation cross-sections for cases where cell proliferation was decreased in the posterior compartment. In addition to decreased cell proliferation, basal contractility in the posterior side was also decreased for Case 10A. (D) Simulation cross sections in which both cell proliferation and basal contractility were decreased in the posterior compartment. The two cases (Case 10A and 10B) represent shapes arising from different initial geometries (curved or flat) used.

the posterior half of the in silico pouch (Fig A.16 C, D). These simulations qualitatively capture the loss in tissue folding (i.e. tissue flattening) observed within the $en > InsR^{DN}$ (Figure 2.8) and $ap > mTOR^{DN}$ samples.

A.3.13 Inhibition of *mTOR* Does Not Affect the Tissue Geometry During the Initial Stages of Development

To investigate morphological data at 72 h AEL for the perturbations reported in the later half of Chapter 2, we collected wing discs (n=12) from apterous>white as a control and apterous> $mTOR^{RNAi}$ perturbation at 84 ± 1.5 h AEL (Fig A.17 A-A') and stained the

discs against βPS (Integrin) and pMyoII antibody (Fig A.17 B-B', C-C'). Qualitatively, we find that the shape of the tissue remains consistent between the internal control (Fig A.17 A-A'), non-perturbed ventral compartment and the genetically perturbed dorsal compartment (Fig A.17 B-C'). We did not observe significant changes in cell height between the dorsal and ventral compartments, indicating an absence of significant early tissue morphological changes. Hence, we can conclude that our simplifying assumptions are appropriate in the current investigation.

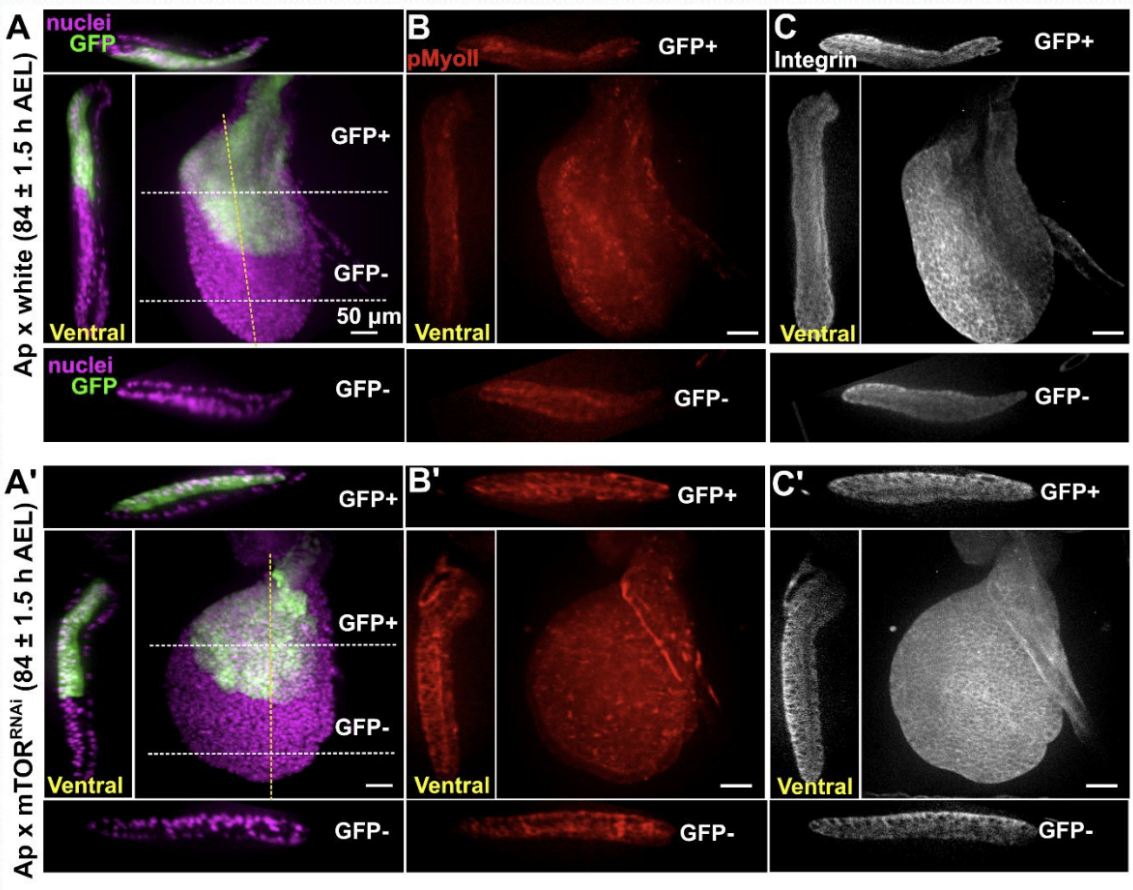

Figure A.17: The shape of the tissue remains consistent between the control, non-perturbed ventral compartment and the genetically perturbed dorsal compartment at very early stages of development. Wing discs (n=12) from (A, B, C) apterous>white (control), and (A', B', C') apterous> $mTOR^{RNAi}$ at 84 $\pm$ 1.5 hours AEL and stained the discs against (B, B') pMyoII and (C, C') βPS (Integrin) antibody to observe the changes in cell heights.

We also investigated wing discs at 72 h (figures not shown), but there is apterous expression on the ventral side at 72 h, which should be contained in the dorsal side. This signifies that the D-V boundary is not fully formed at this stage, and we are likely not yet perturbing the gene in the desired spatial pattern at such an early stage. Hence, we proceeded with our experimentation at 84 h AEL. Future analysis of all genetic perturbations accounting for the possibilities of developmental delays and maturation with early-stage wing discs may provide interesting insights but is beyond the scope of the present investigation.

A.3.14 Inhibiting Dpp Signaling Activity Decreases Rho1 Expression and Reduces Inwards Bending at the Pouch Lateral Domains

The GAL4/UAS [113] system was used to downregulate the activity of Dpp signaling in the posterior compartment of the wing disc with a cross between an engrailed-Gal4 driver and a commercially available $UAS - Tkv^{RNAi}$ line, and AP cross sections of the discs were analyzed (Fig A.18 B). An anti-PMAD antibody staining was carried out for validation. Expression of Tkv^{RNAi} leads to a reduction in fluorescence intensity of PMAD signals in the posterior half compared to the anterior half (Fig A.18 B'). Comparing this with the control, a wing imaginal disc for the parental engrailed-Gal4 driver, the fluorescence peaks in both the anterior and posterior half are roughly comparable (Fig A.18 A'). Next, an anti-Rho1 antibody staining was carried out to measure changes in cytoskeletal regulation (Fig A.18 B"). Rho1 expression is known to promote the phosphorylation of myosin and, hence, is a regulator of tissue contractility [114]. We report a decrease in the expression of Rho1 in the posterior Tkv^{RNAi} expressing compartment compared to its control anterior half (Fig A.18 B"). On the other hand, the expression of Rho1 for the control is symmetric for the anterior and posterior halves (Fig A.18 A"). Lastly, we also report a loss in inward bending at the lateral end of the epithelium in the posterior half, where the Tkv receptors were inhibited (Fig A.18 B).

To validate the Tkv^{CA} genetic perturbations (Fig 2.8), we first expressed Tkv^{CA} only in the posterior compartment of the wing imaginal disc using an *en-Gal4* driver (Fig A.18 C). A

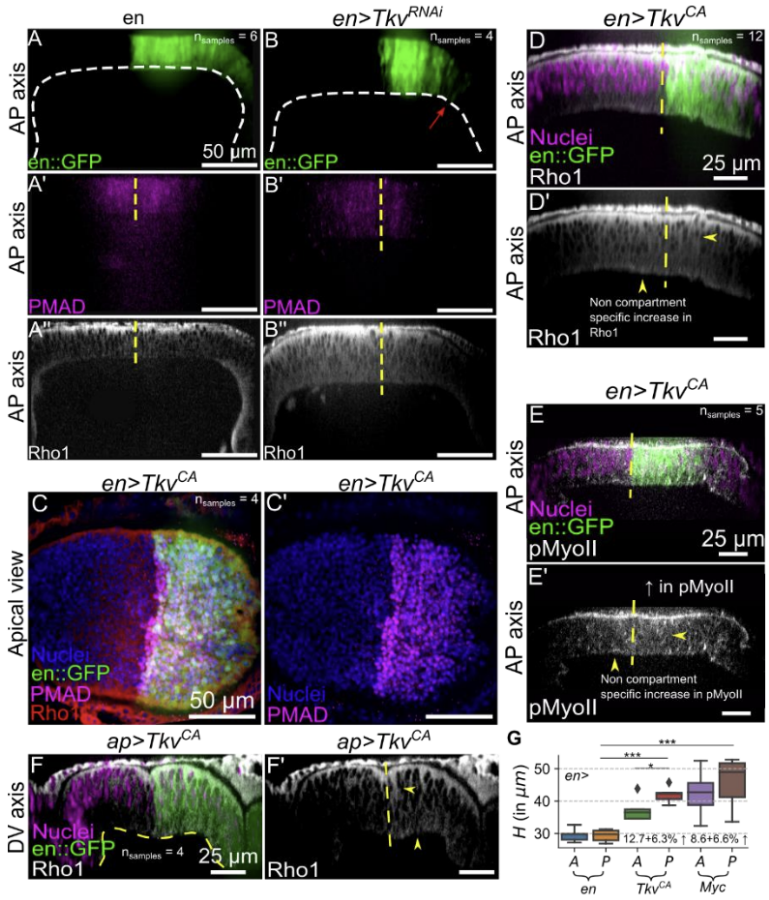

Figure A.18: **Inhibition of Tkv receptors results in a reduction of Rho1 followed by a loss in inwards bending of lateral pouch domains.** (A-A") Cross-section along the DV boundary of a control wing imaginal disc dissected from larvae of an *engrailed-Gal4* driver. Fluorescence labels have been indicated in the lower left panel of each figure. (B-B") Cross-section along the DV boundary of a wing imaginal disc expressing Tkv^{RNAi} in the posterior compartment. The posterior compartment also expresses GFP as indicated in A and B. (C-C") Apical view of discs expressing Tkv^{CA} in the posterior compartment of the wing disc. A PMAD antibody staining was carried out to validate the expression of Tkv^{CA}. (D-E) Cross-section along the DV boundary of a wing imaginal disc expressing Tkv^{CA} in the posterior compartment and stained against. (D-D') Rho1, (E-E') pMyoII. (F-F') Cross-section along the AP boundary of a wing imaginal disc expressing Tkv^{CA} in the posterior compartment and stained against Rho1. The posterior compartment also expresses GFP as indicated in A and B. (G) Box plot visualizing the cell heights within the control and perturbation compartments of experimental data.

PMAD antibody staining was carried out to validate the mutations. PMAD is downstream of Tkv and expression of constitutively active form of Tkv receptors should increase PMAD expression. As expected, we report an increase in PMAD fluorescence in the wing disc posterior compartment (Fig A.18 C') where Tkv^{CA} was expressed. In the Tkv^{CA} genetic perturbations, we also observed a non-compartment specific upregulation of Rho1 (Fig A.18 D-D', F-F') and pMyoII (Fig A.18 E-E'). We also report the distribution of average cell heights in the anterior and posterior compartments for $en > Tkv^{CA}$ and $en > Myc$ genetic perturbations. A student t-test was used to compare the statistical significance between population means ($***: p < 0.001$, $**: 0.001 < p \leq 0.01$, $*: 0.01 < p < 0.05$).

A.3.15 Overexpression of Myc Causes a Reduction in pMyoII and Rho1 Fluorescence Peaks Along the AP Axis

An *engrailed-Gal4* driver was used to overexpress Myc in the posterior compartment of the wing imaginal disc. An IHC assay was carried out to quantify the spatial expression of Rho1 (Fig A.19 A, A') and pMyoII (Fig A.19 A, A") along the pouch AP axis. Quantifications reveal that, unlike the anterior half, the posterior half of the wing imaginal disc does not have the peak in fluorescence near the folds, as shown in Fig A.19 B, B'.

A.3.16 Increasing Proliferation Beyond the Biological Limits Causes Severe Morphological Changes in the Shape of the Simulated Wing Imaginal Disc

To understand the role of patterned proliferation in regulating wing disc shape, we decreased the cell cycle length (C.C.L.) of the cell in the medial domain of the pouch to increase proliferation in the pouch central region compared to its lateral counterparts. We increased proliferation in the medial region by 1.4, 2, 10 and 20 times the control proliferation rates, whereas the proliferation rates for the lateral regions of the pouch were kept intact in each case (Fig A.20 A i-iv). It should be noted that cell proliferation rates are patterned across

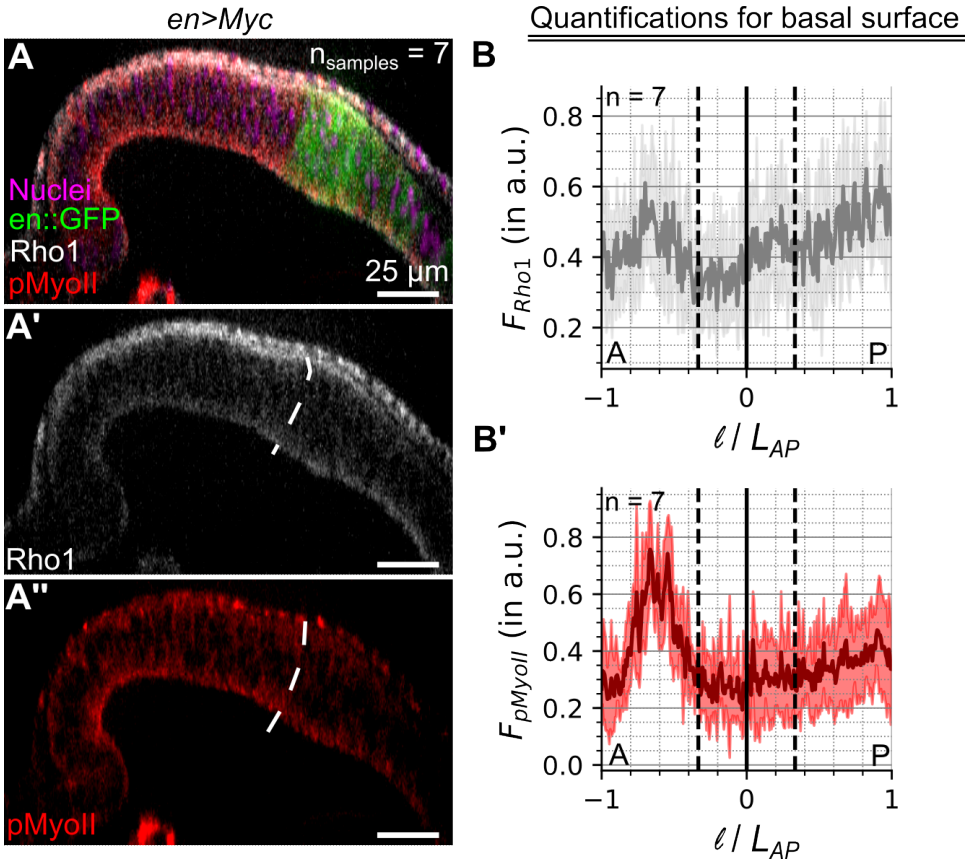

Figure A.19: **Overexpression of Myc reduced pMyoII in the lateral domain and reduced basal curvature.** An *engrailed-Gal4* driver was used to overexpress Myc in the posterior compartment of the wing imaginal disc. (A-A") AP cross-sections of the pouch were visualized. The fluorescent labels have been indicated as insets in the left bottom corners of each plot. A solid white line in A'-A" indicates the compartment boundary separating the anterior (left) and posterior (right) compartments. (B-B') Quantification of Rho and pMyoII across the pouch basal surface. Solid lines indicate the mean, while dashed lines indicate the standard deviation in prediction. Sample sizes have been indicated as the top-left inset of plots.

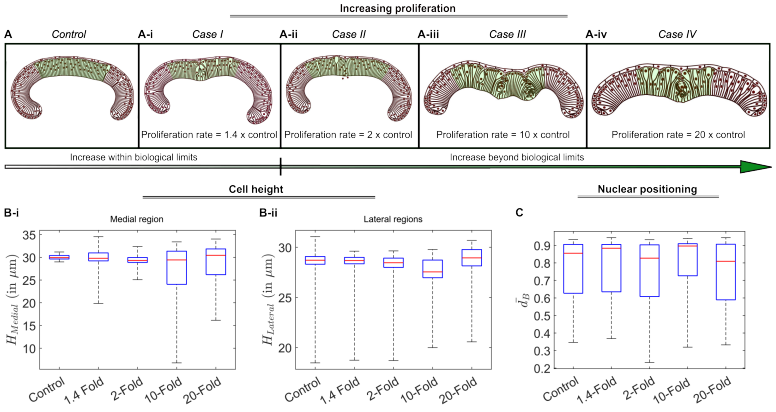

Figure A.20: **Increasing proliferation rate beyond biological limits in silico.** (A-A iv) Through a series of cases, model parameters were varied across the AP axis with proliferation being increased 1.4, 2, 10, and 20 times the control in the central region of the pouch (shown in green). Case II through Case IV correspond to increasing proliferation beyond biological limits. (Bi-Bii) Box plot representing cell heights at the (B) medial and (B') lateral regions corresponding to the cases in A-A iv. (C) Boxplot quantifying the nuclear position corresponding to cases in A-A iv.

the pouch AP axis at earlier developmental stages. The central region proliferates nearly 1.4 times more than the lateral region [112].

The proliferation rates decrease with the age of the pouch. Cases II, III and IV were run to test the effect of very high proliferation rates. With increased proliferation, the cells in the medial domain start to deform, with an increase in variability of cell height across both the medial and lateral pouch domains (Fig A.20 Bi, ii). Interestingly, some of the cells appear to be pushed by their neighbors toward the basal pouch surface (Fig A.20 Aiii, iv). We also see strong deformations on the pouch basal surface where the basal surface extrudes outward locally. This is a current limitation of our computational model, where we do not model cell death due to overcrowding. It has been shown across other model systems that additional pressure exerted by neighboring cells due to overcrowding can initiate cell death pathways [115–118], often as a result of mechanosensation [119], causing the cell to extrude out of the tissue. Very interestingly, due to instability arising because of this overcrowding, we see nuclei within the model simulations going out of the cell, suggesting that the forces within the tissue are no longer able to hold its position within the tissue. Our results here show

how a biologically accurate model, when pushed to its limitations, can result in additional novel biological insights, requiring future experimental validations.

A.3.17 Loss of Cell-ECM Adhesion Causes Apical Constriction Within the Tissue

Analysis of βPS genetic perturbations showed severe changes in basal curvature, cell height (Fig 2.5 B, C, D), and nuclear positioning (Fig 2.6 D, D') within the tissue. To better understand the shape changes occurring because of inhibiting βPS, we used our computational model to first decrease the cell-ECM adhesion by reducing the model parameter k_{adhB} in the pouch medial domain to mimic the knock down of βPS. We additionally allowed the tissue to grow starting with a flat disc of 86 cells with a constant C.C.L. across the AP axis. With a decrease in k_{adhB}, the tissue starts to form an apical constriction (Fig A.21 A-ii) similar to what we report in our experimental data (Fig A.21 B). It is known that cell-ECM adhesion is critical for maintaining the basal surface tension of the cell and that a dysregulation between apical, basal, and lateral tension within pseudostratified epithelium can generate folds. Through this case study, we show how our biophysical growth model can accurately model the experimentally observed tissue shape.

A.3.18 Expression Levels of Rho1 Quantified Using Rho1 Biosensor ANI.RBD-EGFP and Rho1 Antibody Correlate

We requested and received the ani:RBD [120] reporter fly line developed by Dr. Thomas Lecuit's lab from Dr. Lynn Cooley. We fixed the wing disc from this fly line at 6 days AEL and stained it against the Rho1 antibody used throughout the manuscript. The GFP expression of the Rho1 biosensor qualitatively appears to have positive colocalization with the antibody expression (Fig A.22). We also tested a commercially available fly line with Rho1/Rac GTPase activity biosensor (BDSC # 52298), and this also showed qualitatively the same expression as the Rho1 antibody accumulation (results not shown). Hence, we

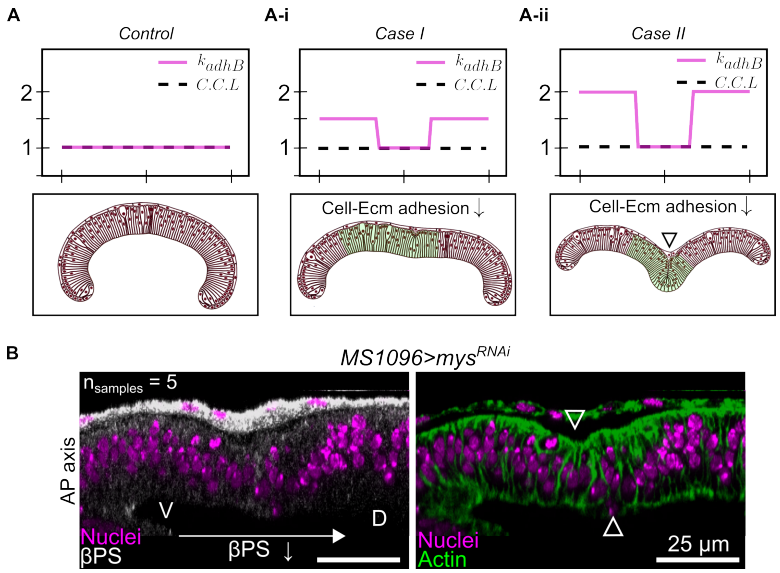

Figure A.21: **Decreasing cell-ECM adhesion with uniform proliferation induces an apical constriction in the medial region of the pouch.** (A-Aii) Model outputs for simulated cases where proliferation was uniform across the tissue (C.C.L.), but cell-ECM adhesion (k_{adhB}) was patterned. In particular, k_{adhB} was decreased in the medial region by 50% and 100% in Case I and Case II, respectively. (B) MS1096-Gal4 driver was used to express mys$^{\text{RNAi}}$ in the dorsal compartment of the wing imaginal disc. An optical section along the AP axis has been visualized. Fluorescent labels have been indicated as an inset within the plot. A decrease in βPS leads to basal nuclei migration (left panel) and an apical constriction formation near the central region (right panel).

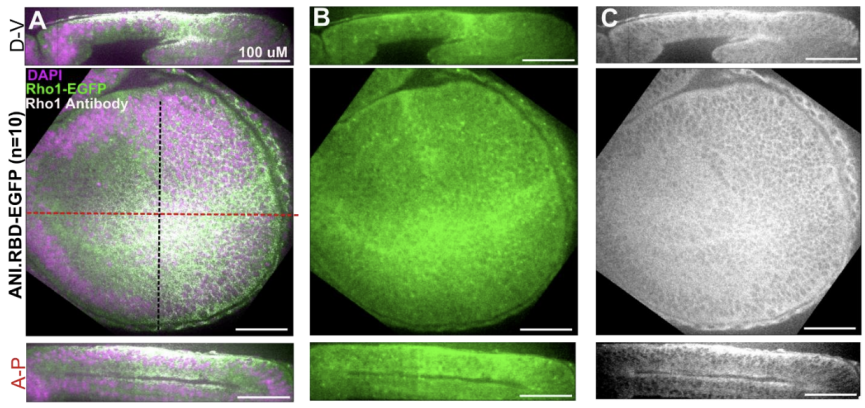

Figure A.22: **Comparison of Rho1 expressions as visualized using a biosensor and an antibody.** (A) Composite, (B) ANI.RBD-EGFP Rho1 Biosensor, and (C) anti-Rho1 antibody staining to observe the expression of Rho1 in the same wing disc. The GFP expression of the Rho1 biosensor (panel B) qualitatively appears to have positive colocalization with the antibody expression (panel C).

conclude that antibody staining of fixed images are roughly equivalent in terms of patterning for both the internal biosensor and antibody staining of fixed tissues.

A.4 Computational Modeling Methods

A.4.1 Initial Conditions for the Computational Model

Starting with the same initial tissue configuration, the quasi-steady states of perturbed model tissues are compared with the reference model tissue presented in the previous publication [24]. Comparisons were drawn at 50,000 AU (arbitrary unit) in simulation time, where each simulation time step size is 0.002 AU similar to the previous publication [24]. The midsection of the tissue can maintain its relative flatness via balancing the apical and basal contractility (Fig 2.4 E-i). Furthermore, the initial condition for simulations with cell proliferation is a curved shape representing the 72-hour AEL mark of the wing disc development (Fig 2.3 B-i). The default value for the spring coefficients of both apical and basal contractile springs is set as 9.0 $\mu N/\mu m$.

A.4.2 Model Calibration Pipeline

The computational model parameters have been calibrated using experimental data either from this study or from literature Appendix A Tables A.1 - A.6. Experimental data related to the *Drosophila* wing disc cross-sectional profile from our previous work (Nematbakhsh and Levis, et al. 2020 [24]) was used to calibrate the cell height, width and number of cells in the model. The model parameters associated with the ECM stiffness (E_{ecm}), volume conservation of the cytoplasm (E_{vol}) and columnar-squamous cell adhesion (E_{adhA}) were calibrated based on measurements found in literature [24]. The wild-type cell membrane stiffness k_{memb}, associated with the potential function E_{ecm}, was calibrated in our previous study (Nematbakhsh et al 2017 [32]) using the experimentally obtained modulus of elasticity of a single cell [95–97]. More specifically, a model simulation was conducted such that a single simulated cell was deformed by applying a linearly increasing force to the membrane nodes on either side of the cell. The deformation of the cell was calculated, and the cell elasticity was determined from the slope of the stress versus strain curve. The parameter k_{memb} was then chosen so that the modulus of elasticity remained within the experimentally measured range [96, 97].

A previous study on epithelial cells by Sim et al. showed that the cell-cell and cell-ECM adhesion levels were within the same range [98]. Hence, the wild-type parameters associated with the cell-cell (E_{adhL}) and cell-ECM (E_{adhB}) adhesions were calibrated using experimentally determined cell-cell adhesion forces for epithelial cells [32]. A computational simulation was run where two adhered cells were pulled until detachment by applying equal stretching forces to the membrane nodes on both sides of these attached cells. Next, the force required to detach these cells was calculated. The parameter k_{adhL} was calibrated so that the force needed to rupture the cell-cell adhesion was in accordance with published experimental data [98, 99]. k_{adhB} was then calibrated using data from literature [24, 32].

In our previous work [24], the Latin hypercube sampling method [100] was used to perform a sensitivity analysis and obtain the range of values for the average nuclei diameter, ECM tension (E_{ECMc}, E_{ECMs}) and actomyosin basal contractility parameters ($k_{bas,cont}$).

The derived parameter set was chosen such that it captured the experimentally measured global basal curvature, mean height and mean nuclei positioning the best. The apical and basal actomyosin contractility parameters ($k_{api,cont}$ and $k_{bas,cont}$) were calibrated using experimentally obtained data from this study. More specifically, $k_{api,cont}$ and $k_{bas,cont}$ were determined based on the local p-MyoII fluorescent intensity measured in experiments. The number of contractile springs in the model, which represented actin filaments inside individual cells, was calibrated using the experimentally observed actin intensity (see Methods section of Chapter 2). On the other hand, the membrane-membrane, membrane-nuclei and membrane-ECM volume exclusion (E_v) parameters were calibrated to ensure numerical stability.

The composite ECM spring constant (k_{ecm}) was calibrated based on the fact that the ECM is stiffer than pouch cells, as indicated in Keller et al. [85] and Harmansa et al. [25]. Specifically, k_{ecm} captures the experimentally observed local basal curvature, cell heights, and nuclear positions in Nematbakhsh and Levis et al. [24]. This study uses the same baseline parameter value. Because the ECM of the pouch cells is stiffer than the pouch cells, we chose a larger value for the ECM spring constant than that of the pouch cell's membrane spring constant.

In this study, we also tested different model scenarios by perturbing parameters in silico (Appendix A Fig A.7) and used experimental data to calibrate these parameters (Figure 2.4 - 2.6, Appendix A Tables A.5, A.6) based on three metrics of calibration: (1) local basal curvature, (2) tissue thickness and (3) nuclear positioning (Figure 2.2 B). Then, we determined the parameter values that generated results in agreement with the experimentally quantified metrics (1)-(3).

To capture cell growth and mitotic rounding, a dividing cell in the model undergoes time-dependent increments in cell volume and actomyosin contractile springs. Both of these increments were calibrated to ensure that cell growth and division completed in a timely manner consistent with experimental observation. Additionally, the maximum equilibrium cell volume (Ω_0) during cell growth was determined according to the expected

cell volume prior to cell division. During mitotic rounding, an increase in the actin and myosin concentrations was experimentally observed towards the basal region of cells and represented in the model by a gradual increase in the number of basal contractile springs. The parameter h representing this increment in actomyosin per simulation time step was calibrated using experimental data. In particular, the experimentally determined time duration for the mitotic rounding process and the portion of the mitotic cell with high actomyosin intensity were used to determine h.

Finally, our computational model accounts for in-plane and out-of-plane cell division because during cell division, the new daughter cell can lie within or outside of the wing disc cross-section that we focused on in this study. The probability that a new daughter cell lies in the same cross-section was experimentally determined by calculating the frequency of daughter cells that remain in the same wing disc cross-section as mother cells.

A.5 Image Analysis and Data Quantification Pipelines

A.5.1 Quantification of Local Basal Curvature

OpenCV [121] in Python was used to get points along the basal surface as a user input (Fig A.23 A). The *splrep* function within Scipy's [58] interpolation module was used to fit a B-spline [122] curve to the points (Fig A.23 B). Next, 90 equally distant points within the curve were sampled using the fit spline model. The sampled points were then scaled so that the total length of the curve was unity. Lastly, the curve was centered around zero (Fig A.23 C-i). Using points on the normalized curve, a spline with a smoothness factor of 0.1 was fit to smoothen the curve (Fig A.23 C-ii). The *splev* function within Scipy's interpolation module was used to compute the first and second derivatives using the xy coordinates of the sampled points in order to compute the numerical curvature (Fig A.23 D) defined by formula below:

$$\kappa = \frac{\frac{dx}{dt}\frac{d^2y}{dt^2} - \frac{dy}{dt}\frac{d^2x}{dt^2}}{\left[\frac{dx}{dt}\frac{dx}{dt} + \frac{dy}{dt}\frac{dy}{dt}\right]^{1.5}} \tag{A.1}$$

For each case, we assume that the middle 30 points constitute the pouch medial domain while the other 30 points on either end belong to the lateral domains. This is based on the assumption where we define that the medial domain acquires the central third of the tissue at each developmental stage. A similar analysis was also carried out to quantify basal curvature for the cross sections generated during simulations (Fig A.23 A'-D').

A.5.2 Quantification of Morphological and Signaling-Related Features from the Wing Imaginal Discs

Using Kappa [123], an ImageJ [111] plugin, user-defined points were used to fit splines along the apical and basal surfaces, respectively. The tool was also used to extract fluorescent intensity of cytoskeletal regulators such as pMyoII along the points on the apical and basal surfaces of the columnar cells (Fig A.24 A, B). Apical surface for the columnar epithelia is labeled carefully to avoid including points from the apical surface of the squamous cells.

In a custom MATLAB-based [107] tool, the number of discretization elements is first defined for analysis (N_{cells}). It is first used to split the basal curve into $N_{cells} + 1$ equidistant nodes. Using the discretized points in the basal surface, corresponding points on the apical surface area are then obtained in a way such that the distances between those points and the apical surface of the pouch are minimized. The methodology allows the discretization of pouches into N_{cells} computational elements each mimicking a pouch cell (Fig A.24 C). A frustum-like shape obtained by joining any two consecutive points on the basal surface and the corresponding distance minimizing apical points is considered as a computational cell for our analysis. For any computational cell, the median intensity of all the points lying between the corresponding nodes on the apical and basal surface is used to approximate local pMyoII intensities across the apical and basal surfaces. Local height is defined as the average distance between the nodes on the basal surface and their counterparts on the apical

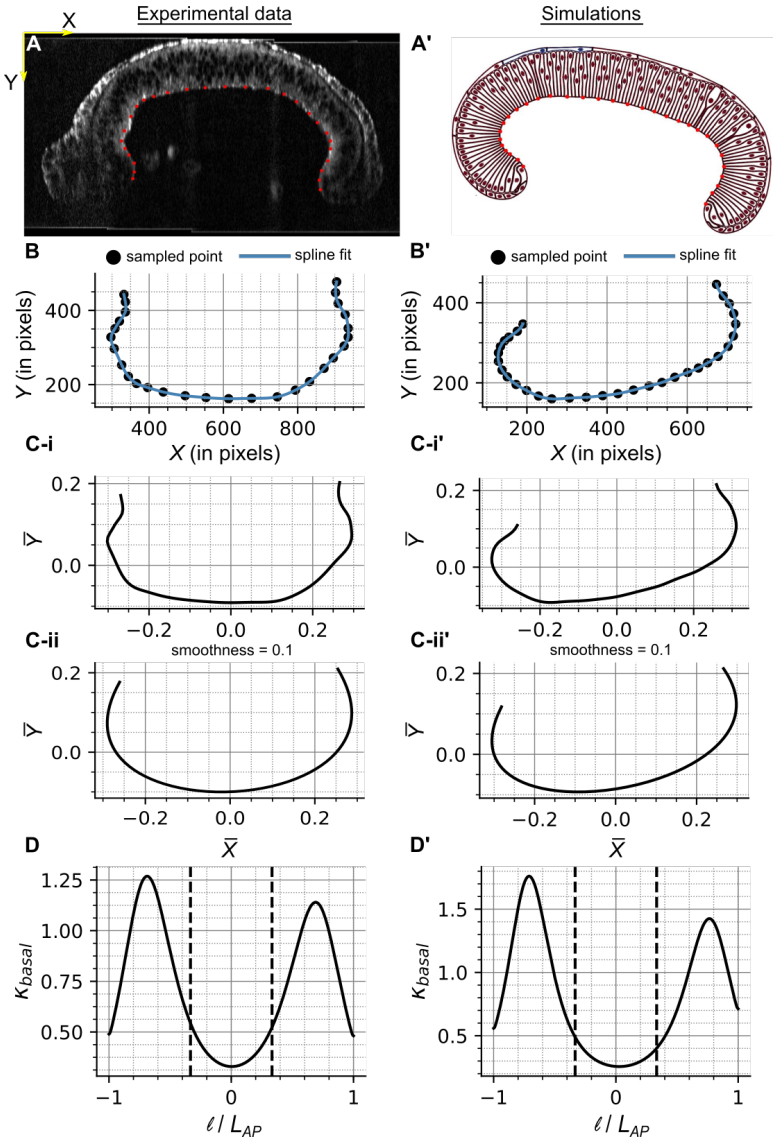

Figure A.23: **Pipeline for quantifying local basal curvature.** (A) User-defined points along the basal surface is indicated in red over the raw cross section data. (B) Plot showing user defined points along the basal surface overlaid with a curve generated by fitting a spline. (C) Plot showing the normalized curve representing the basal surface. (C-ii) A spline with a smoothness factor of 0.1 is fit to smoothen the normalized curve. (D) Plot showing the variation of local basal curvature along the pouch AP axis. The x-axis represents the normalized distance along the basal surface where curvature was calculated. The normalization was done by dividing the distance by half the length of the basal surface. (A'-D') A similar analysis of basal curvature for simulation generated cross sections.

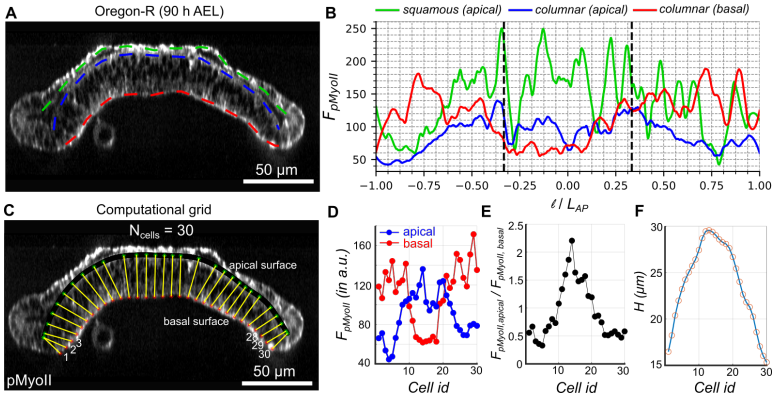

Figure A.24: **Pipeline for extracting local tissue height and the apical-basal ratio of pMyoII.** (A) Visualization of apical-basal surfaces for the columnar and apical surface for the squamous epithelia. (B) Plot showing fluorescence intensity of pMyoII at the pouch surfaces highlighted in A. (C) Visualization of 30 discretized computation cells mimicking columnar cells within the pouch. Cell ids have been indicated in the region below the basal surface of the pouch. (D) Plot showing fluorescence intensity of myosin at the apical and basal surfaces of the columnar cells within the pouch. (E) Plot showing ratio of apical to basal pMyoII for each computational cell within the pouch. (F) Plot showing the variation of local tissue height across the computational cells

surface. As an example, for a disc corresponding to 90 h AEL, the pipeline was used to quantify raw intensities of pMyoII in the apical and basal nodes (Fig A.24 D). The ratio of apical and basal pMyoII intensity across each computational cell (Fig A.24 E) along with the variation of local tissue thickness (Fig A.24 F) have also been plotted.

A.5.3 Quantification of Nuclear Positioning

StarDist [101], an open-source, deep learning-based ImageJ [111] plugin was used to segment nuclei from the background (Fig A.25 A, A'). The segmentation mask was imported to MATLAB [107] for further post-processing. MATLAB's image labeler was first used to generate a mask defining the pouch region to separate out the nuclei of squamous epithelia from the analysis (Fig A.25 B). Fluorescence visualizing the Actin cytoskeleton was used for this task. The same image was also used to get user input of points located on the apical and basal surface using MATLAB's *ginput()* function. Splines were next fit on the user-defined points to generate a smooth and continuous representation for the apical and

basal surfaces (Fig A.25 B'). The *Regionprops* command within MATLAB was then used to estimate the centroid of each nucleus. Minimum distances between the centroid of the nuclei and the apical-basal surfaces were calculated using the *distance2curve* MATLAB function (Fig A.25 C, C'). The proximity of a nucleus from the basal surface is defined as the ratio of its distance from the basal surface over the sum of the distances from both the apical and basal surfaces. This quantity was used to generate a heatmap where each nucleus is color-coded with its proximity to the basal surface (Fig A.25 D). It can be clearly seen that as one moves towards the apical surface, the color transitions indicate an increase in the quantity.

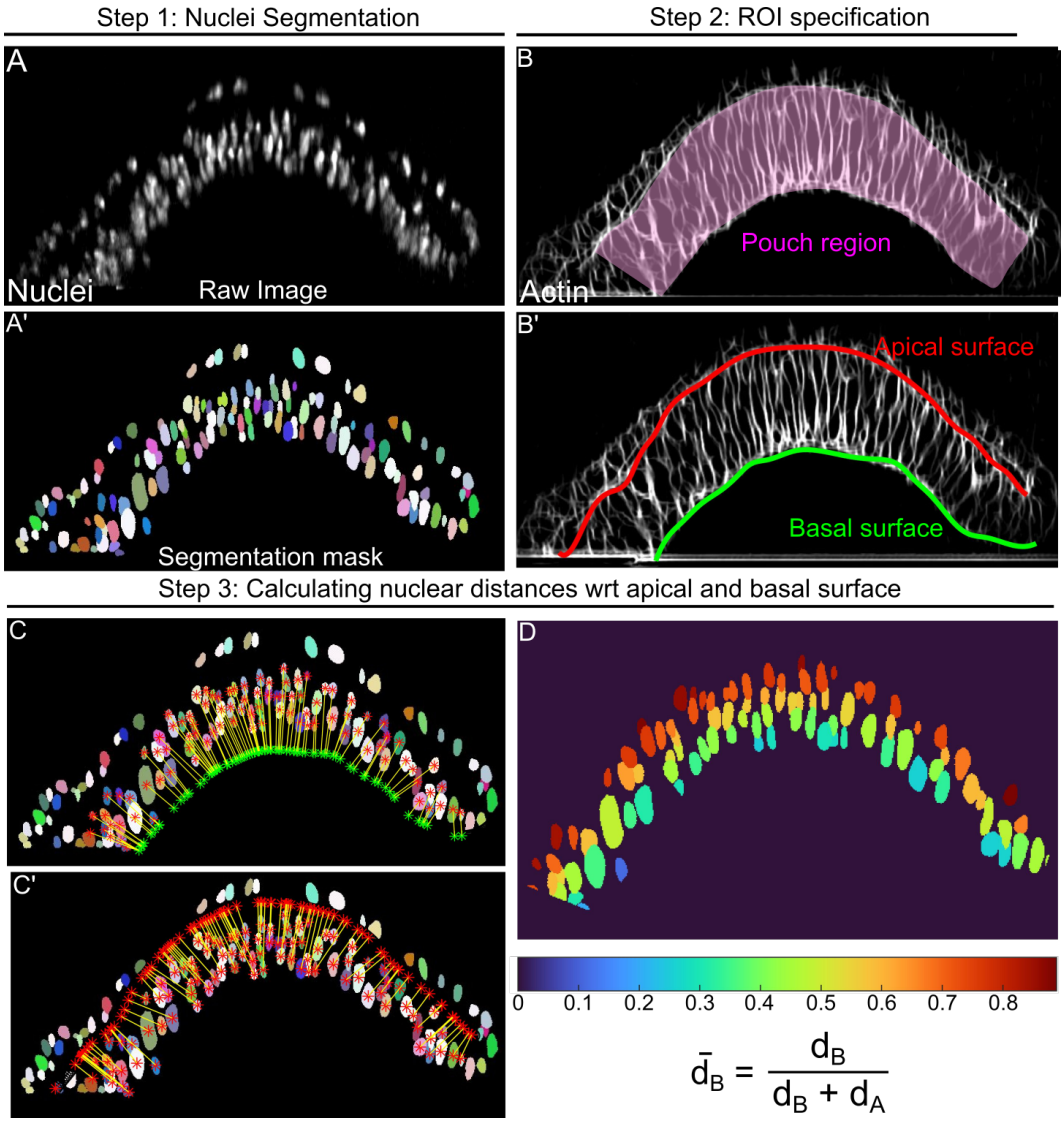

Figure A.25: **Quantification of nuclear positioning.** (A) DV cross-section of a 72 h AEL larval wing imaginal disc with fluorescence showing nuclei. (A') Segmentation mask generated using StarDist. Each color represents a different nucleus. (B) MATLAB's image labeler was used to define the pouch region using the fluorescence channel highlighting the actin cytoskeleton. (B') User-defined points on the apical and basal surfaces are used to generate splines. (C, C') Visualization of distances of the nuclear centroids from the apical and basal surfaces, respectively. (D) Heatmap visualizing relative positioning of nuclei with respect to the basal surface. It is defined as the distance of a nucleus from the basal surface (d_B) over the sum of distances of nuclei from the apical (d_A) and basal (d_B) surfaces.

A.6 Experimental Methods

A.6.1 Immunohistochemistry

Wing imaginal discs were dissected in phosphate-buffered saline (PBS) from 72 h, 84 h, 96 h, or 120 h AEL larvae in intervals of 20 min. Fixation was performed on dissected wing discs in ice-cold 4% paraformaldehyde solution (PFA) in PBS for 1 h in PCR tubes. Fresh PBT (PBS with 0.03% v/v Triton X-100) was used to rinse the wing discs three times immediately following fixation. PCR tubes containing wing discs in PBT were then placed on a nutator for 10 minutes at room temperature and then rinsed again with fresh PBT; this step was repeated for three nutation/rinsing intervals. PBT from after the third rinse was removed and 250 μ L of 5% normal goat serum (NGS) in PBS was added to the PCR tube. Tubes were then agitated on a nutator for 45 minutes at room temperature. NGS was replaced with 250 μ L of a primary antibody mixture prepared in a 5% NGS solution. Next, tubes were agitated on a nutator at 4 °C overnight. The following primary antibodies were used: Phospho-Smad1/5 (Ser463/465) (41D10) (1:300, Rabbit, Cell Signaling Technology #9516S), P-Histone H3 (1:500, Rabbit, Cell Signaling Technology #9701S), Phospho-Myosin Light Chain 2 (Ser19) (1:50, Rabbit, Cell Signaling Technology #3671S), α-Rho1 (1:10, Mouse, Developmental Studies Hybridoma Bank p1D9), Integrin betaPS (myospheroid) (1:5, Mouse, Developmental Studies Hybridoma Bank CF.6G11), α-Collagen IV antibody (1:5, Rabbit, Abcam ab6586). Three PBT rinses were performed the next day as was done after fixation. Tubes were then placed on a nutator for 20 minutes with fresh PBT and this was repeated for three nutation/rinsing intervals. After removing the PBT from the final rinse, 250 μL of a secondary antibody mixture corresponding to the primary antibodies along with DAPI, prepared in a 5% NGS solution, was added. Tubes were then agitated on a nutator for 2 hours at room temperature. The following dyes and secondary antibodies were α-Mouse Alexa Fluor^{TM} 568 (1:500, Goat, Thermo Fisher Scientific A-11031), α-Rabbit Alexa Fluor^{TM} 647(1:500, Goat, Thermo Fisher Scientific A32733), DAPI (1:500, Sigma Aldrich D9542), Fluorescein Phalloidin(1:500, Thermo Fisher Scientific F432). Three subsequent quick PBT

rinses followed by three 20 minutes of agitation on the nutator with fresh PBT at room temperature were performed. Wing discs in PBT were left in the tube at 4 °C for an overnight wash. Four sets of double-layered scotch tape strips were used as spacers to create a square well. The spacers were positioned on the surface of a glass slide which prevents the coverslip from pressing on the wing discs. The wing discs were mounted within the well using Vectashield mounting medium and a cover slip was placed atop, aligned with the spacers.

A.7 Tables

A.7.1 Updated Model Parameters Used in the Subcellular Element Model

The Supplementary Table 1 of [1] was split into Tables A.1 - A.4 to ensure the tables fit in a single page. Table A.1 has the parameter values used in the Morse potential energy functions while Table A.2 has the parameter values for the Linear and Bending Spring energy potentials and Lagrange Multiplier. The model parameters for the ECM can be found in Table A.3. Finally, the model parameters used during cell divison are in Table A.4.

Energy & model parameters	**Definition**	**Interaction Type**	**Values**	**Source**
E_v	Volume exclusion, membrane-membrane	Morse	$U_v = 14.08\ nN\mu m$	*
			$W_v = -14.08\ nN\mu m$	*
			$\xi_v = 0.375\mu m$	*
			$\gamma_v = 0.094\mu m$	*
E_v	Volume exclusion, membrane-nuclei	Morse	$U_v = 14.08\ nN\mu m$	*
			$W_v = -14.08\ nN\mu m$	*
			$\xi_v = 0.32\mu m$	*
			$\gamma_v = 0.039\mu m$	*
E_v	Volume exclusion, membrane-ECM	Morse	$U_v = 14.08\ nN\mu m$	*
			$W_v = -14.08\ nN\mu m$	*
			$\xi_v = 0.1375\mu m$	*
			$\gamma_v = 0.033\mu m$	*
E_{nuc}	Size of nucleus	Morse	$U_{nuc} = 35.5\ nN\mu m$	**
			$W_{nuc} = 35.5\ nN\mu m$	**
			$\xi_{nuc} = 0.392\mu m$	**
			$\gamma_{nuc} = 5.88\mu m$	**
	Interaction range	N/A	2.1 μm	**

Table A.1: Updated model parameters used in the Morse potential energy functions of the Subcellular Element model. Parameters with source marked as * have values calibrated for numerical stability while those marked with ** have been calibrated in this study.

Energy & model parameters	**Definition**	**Interaction Type**	**Values**	**Source**
E_{memb}	Cell membrane and actomyosin at the cortex of the cell	Spring	$k_{memb} = 1800\ nN/\mu m$	[24, 32]
			$L0_{memb} = 0.0625 \mu m$	[24]
$E_{memb,bend}$	Cell membrane and actomyosin at the cortex of the cell	Bending Spring	$k_{memb,bend} = 9\ nN\ \mu m$	[24, 32], ***
			$\theta_0 = \pi\ rad$	[24, 32], ***
$E_{api,cont}$	Apical actomyosin contractility	Spring	$k_{api,cont} = 9\ nN/\mu m$	**
			$L0_{api,cont} = 0.03125\ \mu m$	**
$E_{bas,cont}$	Basal actomyosin contractility	Spring	$k_{bas,cont} = 9\ nN/\mu m$	[24]
			$L0_{bas,cont} = 0.03125\ \mu m$	[24]
E_{vol}	Cytoplasm volume conservation	Lagrange Multiplier	$k_{vol} = 30\ nN/\mu m^2$	[24, 103]
			$\Omega_{0pouch} = 65\ \mu m^2$	[24]
			$\Omega_{0perip} = 65\ \mu m^2$	[24]
			$\Omega_{0BC} = 20\ \mu m^2$	[24]
E_{adhL}	E-cadherin mediated cell-cell adhesion	Spring	$k_{adhL} = 200\ nN/\mu m$	[32]
			$L0_{adhL} = 0.0625\ \mu m$	[24]
E_{adhB}	Integrin mediated cell-ECM adhesion	Spring	$k_{adhB} = 400\ nN/\mu m$	[32, 98]
			$L0_{adhB} = 0.0625\ \mu m$	[24]
E_{adhA}	Columnar-squamous cell adhesion	Spring	$k_{adhA} = 200\ nN/\mu m$	[24]
			$L0_{adhA} = 0.0625\ \mu m$	[24]

Table A.2: Updated model parameters used in the Linear and Bending Springs and Lagrange Multiplier of the Subcellular Element model. Parameters with source marked as ** have been calibrated in this study while those marked with *** have values calibrated in this work based on simulation output as compared to tissue morphology.

Energy & model parameters	**Definition**	**Interaction Type**	**Values**	**Source**
E_{ecm}	ECM stiffness	Spring	$k_{ECM} = 4500\ nN/\mu m$	[85]
			$L0_{ecm,c} = 0.06\mu m$	[24]
			$L0_{ecm,s} = 0.06\mu m$	[24]
			$L0_{ecm,bc} = 0.06\mu m$	[24]
$E_{ecm,bend}$	ECM bending stiffness	Bending Spring	$k_{ecm,bend} = 6\ nN\ \mu m$	[24,32], ***
			$\theta_0 = \pi\ rad$	[24,32], ***
	ECM_c pre-strain	N/A	$c_1 = 540\ nN$	***
	ECM_{bc} pre-strain	N/A	$c_2 = 540\ nN$	***

Table A.3: Updated model parameters used in the energy potential functions representing the extracellular matrix (ECM) in the Subcellular Element model. Parameters with source marked as *** have values calibrated in this work based on simulation output as compared to tissue morphology.

Energy & model parameters	**Definition**	**Interaction Type**	**Values**	**Source**
h	Increment of the height of the portion of a cell with high actomyosin presence during mitotic rounding	N/A	4.6703 x 10^{-5} μm per simulation time step A.U.	Calibrated in this study
Probability of in-plane cell division	The likelihood of a newly created daughter cell resides in the same cross plane of the model wing disc	N/A	0.25	From current experimental measurements
Mitotic event marker	Progression (%) of cell cycle needed to enter mitosis	N/A	95	[12]

Table A.4: Updated model parameters used in the Subcellular Element model during division.

A.7.2 Altered Model Parameters for the In-Silico Model Scenarios

The Supplementary Table 2 of [1] was split into Tables A.5 and A.6 to also ensure that the tables would fit in a single page. Table A.5 includes the parameter values for Cases 1A - 2B of the *in-silico* model scenarios while Table A.6 includes Cases 3A - 7B.

Case	**Energy**	**Definition**	**Parameter multiplier for lateral regions**	**Parameter multiplier for medial regions**	**Parameter Value**
Case 1A	$E_{api,cont}$	Apical actomyosin contractility	0.0625	1.333	$k_{api,cont} = 9\ nN/\mu m$
	$E_{bas,cont}$	Basal actomyosin contractility	1.5	2.0	$k_{bas,cont} = 9\ nN/\mu m$
Case 1B	$E_{api,cont}$	Apical actomyosin contractility	0.0625	0.0029	$k_{api,cont} = 9\ nN/\mu m$
	$E_{bas,cont}$	Basal actomyosin contractility	1.5	1.125	$k_{bas,cont} = 9\ nN/\mu m$
Case 2A	$E_{ecm,c}$	ECM stiffness	0.5	1.0	$k_{ecm,c} = 4500\,nN/\mu m$
Case 2B	$E_{ecm,c}$	ECM stiffness	1.0	0.5	$k_{ecm,c} = 4500\,nN/\mu m$

Table A.5: Altered model parameters for the *in-silico* model scenarios Case 1A - 2B.

Case	**Energy**	**Definition**	**Parameter multiplier for lateral regions**	**Parameter multiplier for medial regions**	**Parameter Value**
Case 3A	E_{memb}	Membrane stiffness	0.5	1.0	$k_{memb,lateral} = 1800\ nN/\mu m$
Case 3B	E_{memb}	Membrane stiffness	1.0	0.5	$k_{memb,lateral} = 1800\ nN/\mu m$
Case 3B'	E_{memb}	Membrane stiffness	1.0	0.1	$k_{memb,lateral} = 1800\ nN/\mu m$
Case 4A	E_{memb}	Membrane stiffness	0.5	1.0	$k_{memb,basal} = 1800\ nN/\mu m$
Case 4B	E_{memb}	Membrane stiffness	1.0	0.5	$k_{memb,basal} = 1800\ nN/\mu m$
Case 5A	E_{memb}	Membrane stiffness	1.0	0.5	$L0_{memb,lateral} = 0.0625\ \mu m$
Case 5B	E_{memb}	Membrane stiffness	0.5	1.0	$L0_{memb,lateral} = 0.0625\ \mu m$
Case 6A	E_{memb}	Membrane stiffness	1.0	0.5	$L0_{memb,basal} = 0.0625\ \mu m$
Case 6B	E_{memb}	Membrane stiffness	0.5	1.0	$L0_{memb,basal} = 0.0625\ \mu m$
Case 7A	E_{adhB}	Integrin-mediated cell-ECM adhesion	1.5	1.0	$k_{adhB} = 400\ nN/\mu m$
Case 7B	E_{adhB}	Integrin-mediated cell-ECM adhesion	2.0	1.0	$k_{adhB} = 400\ nN/\mu m$

Table A.6: Altered model parameters for the *in-silico* model scenarios Case 3A - 7B.

A.8 Statistical Tests

A.8.1 Statistical Tests Employed in Chapter 2

For all the experiments except for the staged Oregon-R discs, a total number of samples greater than 5 was used, except if indicated. Immunohistochemistry and dissection of discs from younger larvae is challenging and we have indicated the sample sizes as insets. A student t-test [109,110] with unequal variances was used to measure the statistical significance between data from any two experimental groups ($^{*}p \in [0.05, 0.01)$, $^{**}p \in [0.01, 0.001)$, $^{***}p \leq 0.001$). Statistics was carried out using the stats module of Scipy [58]. All the data visualization was carried out using either matplotlib and seaborn [124] libraries of Python or MATLAB [107]. Detailed statistics tables corresponding to specific figures within this manuscript can be found in Supplementary Information section S8 Statistical tests of [1].

A.8.2 Statistical test for Appendix Figure A.20

An F-test was calculated using the vartest2 function in MATLAB [107] to evaluate the statistical significance of increasing proliferation. The h and p-values have been listed below. When using this function, if $h = 1$ it means that the null hypothesis has been rejected at the 5% significance level and otherwise when $h = 0$. Details can be found in Table A.7.

Region	Groups Compared	h-value	p-value
Medial Region	control vs. case 1 (1.4 x control)	$h = 1$	$p = 2.9728e^{-22}$
	control vs. case 2 (2 x control)	$h = 1$	$p = 1.0107e^{-07}$
	control vs. case 3 (10 x control)	$h = 1$	$p = 1.1543e^{-36}$
	control vs. case 4 (20 x control)	$h = 1$	$p = 1.3591e^{-29}$
Lateral Regions	control vs. case 1 (1.4 x control)	$h = 0$	$p = 0.5555$
	control vs. case 2 (2 x control)	$h = 0$	$p = 0.9767$
	control vs. case 3 (10 x control)	$h = 0$	$p = 0.9205$
	control vs. case 4 (20 x control)	$h = 0$	$p = 0.4146$

Table A.7: F-test for Appendix Figure A.20

B

Appendix - Chapter 3

B.1 Table of Parameter Values for Model of Actomyosin Network Dynamics

To achieve the simulation results presented in section 3.4 "Preliminary Simulation Results" of Chapter 3, the following parameters were used. Note that these parameter values have not been calibrated but were selected based on the parameter values from [165]. Once the actomyosin network model has been incorporated into the multi-scale SCE model of the wing disc, that's presented in Chapter 2, the actomyosin network will be calibrated using experimental data. For now, the following parameters were used to run preliminary simulations for verification of the computational model.

Parameter	Definition	Value	Source
$k_{actin,spr}$	Actin spring coefficient	150 $pN/\mu m$	[165]
$L0_{actin}$	Actin spring resting length	0.2 μm	[165]
$k_{actin,bend}$	Actin bending spring constant	0.207 $pN\mu m^2$	5 times the value in [165]
θ_0	Actin equilibrium bending angle	π rad	[165]
C_a	Actin drag coefficient	0.216 $pNs/\mu m$	[165]
$k_{actomyo}$	Actomyosin connection spring constant	2 $pN/\mu m$	[165]
$L0_{actomyo}$	Actomyosin connection spring resting length	0 μm	[165]
C_m	pMyoII drag coefficient	400 $pNs/\mu m$	[165]
$k_{myo,spr}$	pMyoII mini-filament spring coefficient	600 $pN/\mu m$	4 times the value of $k_{actin,spr}$ in [165]
$L0_{myo}$	pMyoII mini-filament spring resting length	0.15 μm	[165]
$F_0^{myo-pull}$	Constant pMyoII pulling force	4 pN	[165]
r_{conn}	Actomyosin connection radius	0.15 μm	[165]
dt	Time step	0.0005 s	[165]
k_B	Boltzmann constant	$1.38064852e^{-5}$ $\frac{\mu m\ pN}{K}$	[165]
T	Temperature	300 K	[165]

Table B.1: Parameter values for preliminary simulations in Chapter 3.